To the Standard Model and beyond

A theoretical and experimental study of Leptoquark phenomenology and its traces in LFV $B \to \tau\mu$ decays in theory and with LHCb

Master Thesis

Olaf Massen
October 2022

Supervisors

Prof. Dr. R.J.M. Snellings
GRASP institute
University Utrecht

Dr. A. Grelli
GRASP institute
University Utrecht

Daily Supervisors

Dr. J. de Vries
Nikhef, Theory departement
University of Amsterdam

Dr. M. Lucio Martinez
Nikhef, LHCb Collaboration
Maastricht University

In memory of Sjoerd
Without you I would not have been the person I am today

Abstract

In recent years a number of experimental measurements in the field of flavour physics have showed hints towards a source of physics beyond the Standard Model. Theoretical studies have been performed to understand how new physics could account for these measured deviations from the SM. One of the proposed solutions is the existence of leptoquarks, particles coupling quarks and leptons directly. These leptoquarks will inevitably lead to new phenomenology such as lepton flavour violating decays. In this thesis leptoquarks are studied from a theoretical and experimental point of view. In the theoretical studies a high energy theory producing vector leptoquarks at low energy, the 4321-model, is studied in detail and its contributions to the lepton flavour violating $B_{(s)} \to \tau\mu$ decay are considered. This is followed by the study of a minimal BSM explanation of the flavour anomalies. A χ^2-fit of the parameters of this minimal explanation to the flavour anomalies is performed and it is shown that this minimal model describes the experimental data better than the Standard Model, with a $\Delta\chi^2 = 68.88$ with respect to the Standard Model. Experimentally, the lepton flavour violating decay of $B_{(s)} \to (\tau \to \pi\pi\pi\nu_\tau)\mu$ is studied with the LHCb experiment. First an HLT2 trigger line for this decay is written, to be used in the next data taking run of LHCb. Next a start was made with the search for the $B_{(s)} \to \tau\mu$ decay in Run 2 data. Potential Λ_b-baryon backgrounds were studied with RapidSim, an analytic reconstruction of the missing neutrino momentum was performed and a fit was performed on the invariant mass distribution of the $B^0 \to D^-(\to K^+\pi^-\pi^-)\pi^+$ normalisation channel. This work shows how in theory leptoquark models can account for the flavour anomalies and give contributions to lepton flavour violating B-meson decays. Experimentally this work forms a basis for both the search for $B_{(s)} \to (\tau \to \pi\pi\pi\nu_\tau)\mu$ in Run 2 data as well as for the search in future data runs like Run 3 of the LHCb experiment.

Contents

Introduction

The Standard Model of Particle Physics (SM) is one of the most successful models in the history of physics. It describes the fundamental building blocks of nature and their interactions.[1] The SM has been developed mainly in the second half of the twentieth century and it is still being studied extensively today. Using the SM physicists have been able to describe and calculate many processes within the field of elementary particle physics with great precision and these predictions have been confirmed by numerous experiments. With the discovery of the Higgs Boson[1, 2], a particle predicted to exist in the early sixties by Peter Higgs, Francois Englert and Robert Brout[3, 4], all fundamental particles in the SM had been observed experimentally.

However, despite the great successes of the SM, there are some fundamental questions that cannot be answered using merely the SM. To give a few examples, within the SM there are three generations of quarks and leptons but it is not clear why there are exactly three generations and why they differ in mass. Another unsolved problem within the SM is the mass of the neutrinos. Within the SM all three generations of neutrinos are massless, but neutrinos have been observed to oscillate from one flavour into another[5]. This is only possible if there is a mass difference between the different generations. These are indications that the SM is not a complete theory of elementary particle physics.

In addition to these fundamental problems there have been several experimental measurements throughout the last few years that show a discrepancy with the expected theoretical SM values. Among the most notable examples are the anomalous magnetic moment of the muon, $(g-2)_\mu$[6, 7], and the ratio of the decay of B-mesons to a Kaon and either muons or electrons, R_K and R_{K^*}[8, 9]. They show a deviation from the SM of 4.2, 3.1 and 2.5 standard deviations respectively. While there is quite some discussion on parts of the theoretical calculation of $(g-2)_\mu$, $R_{K^{(*)}}$ is theoretically a very clean observable. In addition to these three measurements there are more observables in the field of flavour physics showing discrepancies with the SM: $R_{D^{(*)}}$[10], the Angular distribution of $B_d \to K^{*0}\mu\mu$[11] and even observables in hadronic B-decays[12]. The collection of these discrepancies are often called the *flavour anomalies*. Even though no signal measurement exceeds the magical 5σ-limit, the set of all anomalies have intensified studies to further extend the SM.

These extensions of the Standard Model are called Beyond the Standard Model theories (BSM) and they come in many different kinds of shapes and sizes. Some BSM models include

---

[1]Excluding gravity, which is the odd one in the bunch of fundamental interactions. It will not be considered throughout this thesis.

new Higgs-like particles[13] while others introduce new force carriers. One of these new type of force carriers can couple quarks directly to leptons and is called a Leptoquark (LQ)[14]. Many of these theories are able to account for the flavour anomalies, but in addition they also contribute to processes shown to be in accordance with the SM. LQs have been studied extensively and they will play a major part in this thesis. Since LQs couple quarks and leptons directly one can imagine that they lead to a range of processes that are not allowed in the SM. The main topic of this thesis is the lepton flavour violating (LFV) decay $B_{(s)} \rightarrow \tau\mu$, a decay to which LQs can give a large contribution.

The goal of this thesis is twofold. On the one hand, a theoretical study of different BSM theories containing leptoquarks will be conducted. First a general overview of the standard model and BSM theories will be given, followed by a more detailed study of the so-called 4321-model[15]. Next we will move on to a minimal BSM explanation for the flavour anomalies[16], where the parameter space of the coupling constants in that theory will be studied by performing a χ^2-fit for the coupling constants of the theory to a selection of experimental observables. Then the preferred parameter space of the coupling constants will be studied using a Markov-Chain Monte Carlo simulation[17].

In the second half of this work the LFV $B_{(s)} \rightarrow \tau\mu$ decay will be studied experimentally with the LHCb experiment, one of the four major experiments at the Large Hadron Collider (LHC) [18]. This decay is highly suppressed in the SM, with a branching fraction as low as $\mathcal{B} < 10^{-54}$[19]. However some BSM particles, such as LQs, can lead to an increase of the branching fraction up to the order of $\mathcal{B} < 10^{-10} - 10^{-4}$, depending on the details of the theory[20, 21]. This could place its branching fraction in the vicinity of the limit of what can be measured, since the current limit set by a previous analysis by LHCb is of the order $\mathcal{B} < 10^{-5}$[22]. A signal of this decay would be a clear signal of new physics (NP) and this makes it an interesting decay to search for. The LHCb experiment is designed to study the decays of b- and c-hadrons, making it the perfect candidate to study this specific process. First preparations are made to study this decay in the future by writing a trigger line for this specific process to be used in the next data-taking run of LHCb, starting somewhere in 2023. Then some of the building blocks of the analysis, searching for the $B_{(s)} \rightarrow \tau\mu$ decay using Run 2 data of the LHCb experiment, will be created.

Part I

Theoretical studies of BSM solutions to the flavour anomalies

Chapter 1

Standard Model of Particle Physics

The Standard Model of particle physics describes the fundamental building blocks of nature and the three forces governing their interactions: the electromagnetic (EM), weak and strong force. In this chapter an introduction to the mathematical structure of the SM will be given. Then an introduction into effective field theories will be given, since these will be used at different points within this thesis. Successful as the SM is in making precise predictions, it is starting to show some cracks. In the final section an overview will be made of some of the major experimental results that differ from the SM predictions. For a more basic introduction into the SM one can consult [23].

1.1 The Standard model as a quantum field theory

The SM of particle physics is a non-Abelian gauge theory under the $SU(3)_c \times SU(2)_L \times U(1)_Y$ group. The constituents of the SM can be divided into two categories: fermions and bosons. The fermionic sector of the SM, containing the matter particles, consists again of two types of particles, quarks and leptons. The representations of the leptons and quarks under the SM gauge groups are given by:

$$\ell_L^i = \begin{pmatrix} \nu_L^i \\ e_L^i \end{pmatrix} \in (1, 2, -\frac{1}{2}), \tag{1.1}$$

$$e_R^i \in (1, 1, -1), \tag{1.2}$$

and

$$q_L^i = \begin{pmatrix} u_L^i \\ d_L^i \end{pmatrix} \in (3, 2, \frac{1}{6}), \tag{1.3}$$

$$u_R^i \in (3, 1, \frac{2}{3}), \tag{1.4}$$

$$d_R^i \in (3, 1, -\frac{1}{3}). \tag{1.5}$$

Both the leptons and quarks come in three generations only differing in mass, indicated by the index i. In the lepton sector the three generations are the electron (e) and electron

Standard Model of Elementary Particles
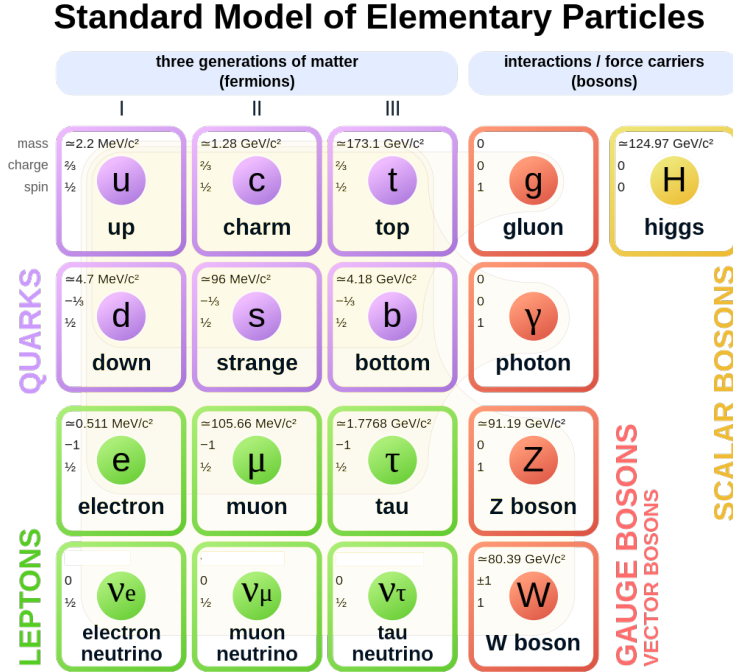
Figure 1.1: Fundamental building blocks of nature in the Standard Model of particle physics. Figure adapted from [24].

neutrino (ν_e), the muon (μ) and muon neutrino (ν_μ) and the tau lepton (τ) and tau neutrino (ν_τ). In the quark sector the three generation of up-type (U) quarks are up (u), charm (c) and top (t). The three down-type (D) quarks are down (d), strange (s) and beauty (b).

The bosons in the SM are the force carriers, responsible for the interactions between fermions. Each gauge group has corresponding gauge bosons mediating that force. A distinction must be made in the situation before or after electroweak symmetry breaking (EWSB). Before EWSB the gauge groups and corresponding gauge bosons are $SU(3) : G_\mu^a \in (8, 1, 0)$, $SU(2) : W_\mu^i \in (1, 3, 0)$ and $U(1) : B_\mu \in (1, 1, 0)$. In EWSB the gauge groups $SU(2)_L \times U(1)_Y$ are spontaneously broken to $U(1)_{EM}$ via the Higgs mechanism. After EWSB there are the three massive gauge bosons mediating the weak force, $W^\pm$ and Z, the massless photon (γ) mediating the electromagnetic force and the Higgs boson (H), the only scalar particle in the SM. The strong force is mediated by the massless gluons corresponding to the unbroken $SU(3)$ gauge group. In Figure 1.1 all fundamental particles within the SM are shown, including their masses. The quantum field theory describing the electromagnetic interaction is called quantum electrodynamics (QED) and the quantum field theory describing the strong force is called quantum chromodynamics (QCD). A working knowledge of both QED and QCD will be assumed throughout this thesis. For more information on these topics consult the excellent textbook of [25]. Since the weak interaction plays a major part throughout this thesis some aspects of it will be covered next.

1.1.1 Weak interaction and flavour physics

Since this thesis is mainly about the field of flavour physics and the flavour anomalies a bit of time will be spent introducing the weak interaction, which plays a major role in flavour physics. One of the main characteristics of the weak interaction is the possibility to change the flavour of the quarks participating in the interaction via the W^+ and W^- bosons. As can be seen from the quantum numbers of the fermionic fields, the weak interaction works on all left-handed fermions. There are two bases in which the quark fields can be considered: the interaction or flavour basis and the mass basis. In the interaction basis the quark flavours do not mix in the interaction Lagrangian, while in the mass basis the quark flavours do not mix in the Yukawa Lagrangian. To see how writing both the interaction and Yukawa Lagrangian in the same basis leads to flavour changing interactions, one can first consider the interaction between the W-bosons and the quarks in the interaction basis:

$$\mathcal{L}_{\text{Flavour changing}} = -\frac{g}{\sqrt{2}} \bar{u}_L^{i,I} \gamma_\mu W^{\mu+} d_L^{i,I} - \frac{g}{\sqrt{2}} \bar{d}_L^{i,I} \gamma_\mu W^{\mu-} u_L^{i,I}. \tag{1.6}$$

The quark fields gain mass via the interaction with the Higgs boson. After EWSB the mass terms of the quark fields are given by the so called Yukawa-terms:

$$\mathcal{L}_{\text{Yukawa}} = -\frac{v}{\sqrt{2}} Y_{ij}^d \bar{d}_L^{i,I} d_R^{j,I} - \frac{v}{\sqrt{2}} Y_{ij}^u \bar{u}_L^{i,I} u_R^{j,I} + \text{h.c.}, \tag{1.7}$$

where v is the Higgs vacuum expectation value and Y are the Yukawa couplings, which are not diagonal in this basis. To associate a mass with each quark the Yukawa couplings must be diagonalised. This can be done by writing the Yukawa couplings, using matrix notation, as:

$$\frac{v}{\sqrt{2}} Y^d = U_d M_d K_d^\dagger, \tag{1.8}$$

$$\frac{v}{\sqrt{2}} Y^u = U_u M_u K_u^\dagger, \tag{1.9}$$

where $M_{u,d}$ are the diagonal mass matrices and the matrices U_d, U_d, K_d and K_u are unitary matrices. Besides this, one is also allowed to perform a change of basis on the left- and right-handed quark fields. The quark fields will be transformed as $u_L^I \to U_u u_L^I$, $d_L^I \to U_d d_L$, $u_R^I \to K_u u_R$ and $d_R^I \to K_d d_R$. This is the change of basis to go from the interaction basis to the mass basis. Applying these transformations to the Yukawa Lagrangian will yield diagonal terms:

$$\mathcal{L}_{\text{Yukawa}} = -M_d^i \bar{d}_L^i d_R^i - M_u^i \bar{u}_L^i u_R^i + \text{h.c.}. \tag{1.10}$$

This change of basis can be applied to the interaction Lagrangian to find its form in the mass basis. Plugging the transformations into the equation yields:

$$\mathcal{L}_{\text{Flavour changing}} = -\frac{g}{\sqrt{2}} \bar{u}_L^i \left(U_u^{i\dagger} U_d^j \right) \gamma_\mu W^{\mu+} d_L^i - \frac{g}{\sqrt{2}} \bar{d}_L^i \left(U_d^{i\dagger} U_u^j \right) \gamma_\mu W^{\mu-} u_L^i. \tag{1.11}$$

One can now define the matrix $V^{\text{CKM}} = U_u^\dagger U_d$, which is the CKM-matrix. By convention the choice is made to have the up-type quarks be equal in both the interaction and mass basis. The CKM-matrix gives the transformation for the down-type quarks:

$$\begin{pmatrix} d^I \\ s^I \\ b^I \end{pmatrix} = \begin{pmatrix} V_{ud} & V_{us} & V_{ub} \\ V_{cd} & V_{cs} & V_{cb} \\ V_{td} & V_{ts} & V_{tb} \end{pmatrix} \begin{pmatrix} d \\ s \\ b \end{pmatrix}. \tag{1.12}$$

By construction the CKM matrix is unitary. There are four degrees of freedom in the CKM matrix: three real parameters and one complex phase. This complex phase in the CKM matrix is the source of CP-violation, the asymmetry between matter and anti-matter, in the weak-interaction. In fact, it is the only source of CP-violation in the SM.[1]

1.2 Effective field theories

Effective field theories (EFT) have been used in particle physics for a very long time. Every student in the field of particle physics has encountered effective field theories, although they may not have realised it. An effective field theory is way to perform calculations without an exact understanding of the deeper underlying theory. This is exactly what the Fermi theory, used to describe beta decays, is. It is an effective description of the weak interaction at an energy scale significantly lower than the mass of the W-boson. This concept can be extended to other theories and it is a useful tool in studying theories beyond the Standard Model. A low-energy approximation of some (unknown) theory at higher energies can be constructed to make predictions at this lower energy.

Effective field theories are constructed up to a certain power of a small parameter α, which is the ratio of two energy scales far apart from one another. This parameter α is called the power counting parameter. The EFT can be expanded to an arbitrary order in α, reducing the theoretical error in calculations to the desired degree. In general an EFT Lagrangian can be written as the sum over EFT operators with their coefficients. So an EFT Lagrangian to the first order in α is:

$$\mathcal{L}_{\text{EFT}} = \alpha \sum_i C_i O_i, \tag{1.13}$$

where O_i are the operators and C_i are the corresponding coefficients, called Wilson coefficients. By extracting the order of α from the Wilson coefficients the Wilson coefficients are kept dimensionless.

There are two distinct ways in which EFTs are used: top-down and bottom-up. In the top-down approach a simpler low-energy effective theory is constructed from a known high-energy theory. Based on the symmetry of the full theory all possible operators are determined. The coefficients of the operators are determined by matching the full theory to the EFT. Simple observables are calculated using the full theory and unwanted degrees of freedom are removed. The coefficients of the EFT are chosen in such a way that a calculation

---

[1]There is a CP-violating term in the QCD-Lagrangian but measurements have shown that this term has a zero phase. It is unclear why this is the case and this problem is called the strong CP-problem.
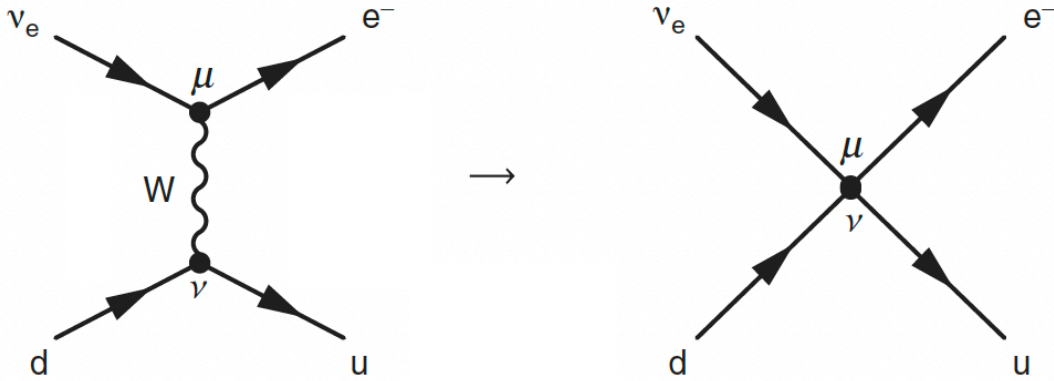
Figure 1.2: The elementary process for beta decay in the weak interaction on the left and in the Fermi theory on the right, where the energy of the process $q^2 << m_W^2$. Figure taken from [26].

using the EFT yields the same result as the calculation in the full theory. This matching can be done to the desired order of α. Once the matching has been completed one can use the EFT to perform calculations. To give a concrete example of this procedure let us again consider the Fermi theory. The full theory of the Fermi theory is the weak interaction. By calculating the Feynman diagram using the Feynman rules of the weak interaction and making the approximation that the mass of the W-boson is much larger than the energy of the process the value of the coefficient, G_F in this case, can be found in terms of the W-boson mass. The process of removing heavy particles from the full theory to create an effective theory is often called *integrating out* the heavy particles. In Fig 1.2 the Feynman diagrams for beta-decays are shown in both the full theory and the Fermi theory EFT. Another example of a top-down EFT is heavy quark effective field theory (HQEFT). HQEFT is used to describe mesons containing a b or a c quark by integrating out the b- and c-quarks.

In the bottom-up approach the framework of EFTs is applied, however the full theory is unknown. The Wilson coefficients cannot be computed since the high-energy theory is not known. The Wilson coefficients have to be fitted to experimental measurements. It is important that the number of predictions one can make with this EFT is larger than the number of fit parameters. This bottom-up approach is often used when looking for physics beyond the Standard Model. All operators in the SM have mass-dimension 4. However, one can construct higher dimensional operators using the SM-constituents. This is done in the Standard Model Effective Field Theory (SMEFT). New physics can be described in terms of the SMEFT Wilson coefficients. The $d = 5$ operators violate lepton number and give rise to neutrino masses[27]. Most analyses consider lepton number conserving $d = 6$ operators. If all possible Hermitian, baryon number and lepton number conserving $d = 6$ SMEFT operators are considered one would need to sum over 2499 operators[28]. The EFT Lagrangian would have the form:

$$\mathcal{L} = \mathcal{L}_{\text{SM}} + \frac{1}{\Lambda^2} \sum_{i=1}^{2499} C_i^{d=6} O_i^{d=6}, \tag{1.14}$$

where Λ is the scale of new physics. In a bottom-up approach a fit is then performed to experimental measurements to determine the Wilson coefficients. Since performing a fit to 2499 coefficients is downright impossible often a subset of these operators is considered and fitted to a selection of relevant experimental results.

1.3 Theory versus Experiments: the flavour anomalies

As was mentioned at the beginning of this chapter the SM is starting to show some cracks. There have been several measurements in the last couple of years, many of them in the field of flavour physics, that show deviations from their SM predictions. While no single observation has passed the 5σ-benchmark, it is interesting nonetheless that multiple measurements within the same field show $1 - 3\sigma$ deviations. Our focus will be on the so called B-anomalies. These B-anomalies are measurements of (properties of) semi-leptonic B-meson decays disagreeing with their SM predictions. The two main categories are flavour changing neutral currents ($b \to sll$ transitions) and flavour changing charged currents ($b \to cl\nu_l$ transitions). In addition the muon magnetic dipole moment anomaly will be touched upon as well.

1.3.1 Flavour-changing neutral currents

As mentioned, a number of anomalies have been observed in $b \to sll$ transitions. In the SM these transitions are forbidden at tree level and can only happen via electroweak penguins and box diagrams. What makes these processes so interesting with potential new physics in mind is that new physics, in the form of new heavy particles, could enter in the loop and have a significant contribution to different observables. Interesting observables are the branching ratios and angular distributions of decays containing a flavour chaning neutral current (FCNC). Two of the flavour anomalies within the $b \to sll$ transitions will be highlighted: the angular distribution of $B_d \to K^{*0}\mu\mu$ decays and lepton flavour universality tests (LFU) with $R_{K^{(*)}}$.

The decay of $B_d \to K^{*0}\mu\mu$ is a FCNC that at first order happens via an electroweak penguin diagram. Next to measuring the branching fraction, the angular distribution of this decay has been measured by the LHCb collaboration [11]. From a BSM point of view these angular distributions are particularly interesting since they are, to a large extent, independent of hadronic uncertainties[29]. These hadronic uncertainties can play a large role in the computation of branching fractions or other observables. Deviations in these kind of 'clean' theoretical observables could be a unambiguous sign for BSM physics. The LHCb collaboration performed a measurement of this angular distribution and compared it to the theoretical SM predictions in [29]. In this comparison they found a 3.4σ deviation for one of the angular observables, P_5'. More details on this, quite complicated, analysis can be found in [11].
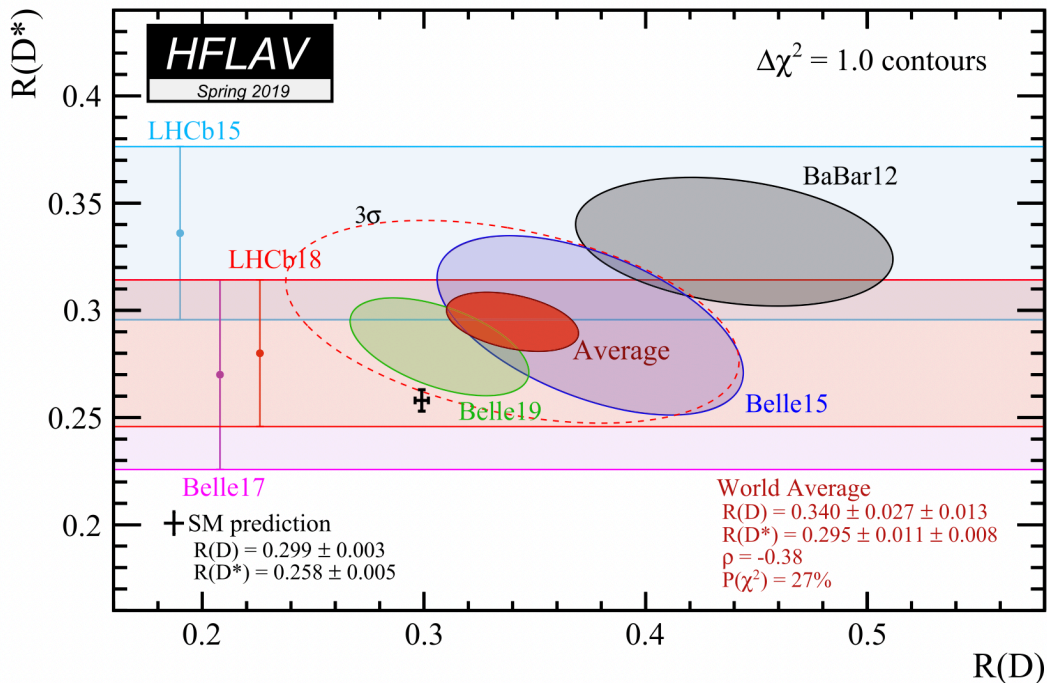
Figure 1.3: The world averages and SM values for $R(D)$ and $R(D^*)$. In addition the measurement by BABAR, Belle and LHCb have been included as well. Figure taken from [10].

Other theoretically clean observables in $b \to sll$ transitions are the LFU tests with the ratios R_{K^*} and R_K, defined as:

$$R_H = \frac{\int_{q_{min}}^{q_{max}} \frac{d\mathcal{B}(B \to H \mu^+ \mu^-)}{dq^2} dq^2}{\int_{q_{min}}^{q_{max}} \frac{d\mathcal{B}(B \to H e^+ e^-)}{dq^2} dq^2}. \tag{1.15}$$

Within the SM these ratios can be calculated with great precision and have a value of 1. This is due to the fact that the leading-order contribution is an electroweak penguin and within the SM the coupling of leptons to the Z-boson or photon are lepton flavour independent. Hadronic uncertainties in these calculations largely cancel since the ratio of the two decays is taken. These ratios have be measured for the specific decays $B^0 \to K^{*0}\ell^+\ell^-$ and $B^0 \to K^+\ell^+\ell^-$ giving the ratios R_{K^*} and R_K respectively. Both show a deviation from the SM, with a significance of 2.5[8] and 3.1[9] standard deviations. These deviations, if they would persist in future measurements, would be a clear signal of the violation of lepton flavour universality and a direct proof of physics beyond the SM.

1.3.2 Flavour changing charged currents

In addition to the anomalies in the FCNCs there are also some discrepancies in flavour changing charged currents (FCCC), or $b \to c\ell\nu_l$ transitions. In comparison to the FCNC these transitions are allowed at tree level in the SM and they test the universality of the
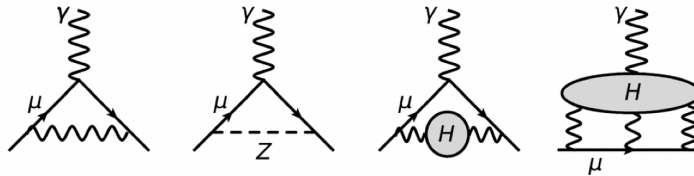
Figure 1.4: The Feynman diagrams for some of the SM corrections to the muon magnetic moment. From left to right these are the first order QED and weak correction, hadronic vacuum-polarisation correction and the light-by-light hadronic correction. Figure taken from [6].

couplings of leptons to the W-boson. Deviations with respect to the SM have been observed in the ratios R_D and R_{D^*}. These ratios are defined similarly to the ratios R_{K^*} and R_K:

$$R_{D^{(*)}} = \frac{\mathcal{B}\left(B \to D^{(*)}\tau\nu_\tau\right)}{\mathcal{B}\left(B \to D^{(*)}\ell\nu_\ell\right)}, \tag{1.16}$$

where $\ell = \mu$ or e. Just as before the hadronic uncertainties cancel to a large extent in the ratios. Both these ratios have been measured by BABAR[30] and Belle[31], while LHCb has only published a measurement of $R(D^*)$[32]. The averages of these measurements have been calculated by the Heavy Flavour Averaging Group (HFLAV) and have been compared to the most precise SM calculations. The different measurements, their average and the discrepancy with respect to the SM can be seen in Figure 1.3. The combination of $R(D)$ and $R(D^*)$ show a deviation from the SM predictions with a significance of 3.1σ.

1.3.3 Muon magnetic dipole moment

The final topic of this chapter will be $(g-2)_\mu$, the muon anomalous magnetic moment. Although this is not part of the flavour anomalies, there are no B-mesons to be found here, this anomaly is quite striking. In addition, muons are involved in all anomalies discussed above so if there would be some NP influencing the behaviour of muons there is a chance it can be seen in the $(g-2)_\mu$ measurement as well. The magnetic moment of a muon (or an electron) is given by:

$$\vec{\mu}_\mu = g_\mu \frac{q}{2m_\mu}\vec{s}_\mu, \tag{1.17}$$

where $g = 2(1 + a_\mu)$. $a_\mu = (g-2)_\mu$ is called the anomalous magnetic moment of the muon. Before the discovery of the muon the magnetic moment of the electron was already studied in great detail. The first prediction came from the Dirac equation, which predicted $g_e = 2$, and the first quantum correction was calculated by Schwinger: $a_e = 1 + \frac{\alpha}{2\pi}$. Nowadays the quantum corrections for both the electron and the muon have been measured to a great precision. The Feynman diagrams of some of the SM contributions have been drawn in Figure. 1.4 but there are more diagrams contributing, for example containing the Higgs boson. Recently a large international collaboration published the results for an updated, state of the art, calculation of a_μ in the SM to compare this result with future and previous

measurements [7].

There have been multiple measurements of the anomalous magnetic moment. In 2006 the final results of the E821 experiment at Brookhaven National Laboratory (BNL) were published [33]. This result, measuring a_μ at a precision of 0.54ppm, deviated $2.2 - 2.7\sigma$ from the SM prediction available at that time. The updated SM prediction has a deviation of 3.7σ from the BNL result. More recently a new experiment at Fermilab, E989, designed to confirm or disprove the results by BNL, published it first results of a_μ at a precision of 0.46ppm[6]. This result is in agreement with the results from BNL and shows a deviation from the SM prediction of 4.2σ. This in itself is a quite striking result and it is the only single measurement closing in on the 5σ benchmark. However it is important to note that there is quite some discussion in the community on the estimation of the errors in the SM prediction, especially in the uncertainties of the hadronic corrections. Parts of these calculations have to be performed using non-perturbative techniques, such as lattice QCD, and it can be difficult to assign precise errors when using these techniques. Nevertheless it is an interesting result and it will be considered later on when studying a minimal explanation to the flavour anomalies.

Chapter 2

Beyond the Standard Model solutions to the flavour anomalies

As covered in the previous chapter the Standard Model is starting to show some cracks. For a long time physicists have been studying extensions of the SM. Even during the development of the SM[1] it became clear that to solve some issues, the SM alone would not suffice. Famous examples are the three generations of leptons and quarks in the SM and the hierarchy problem: why is gravity, the only fundamental force not described in the SM, so much weaker than the other forces? However, some theories were simply developed as natural extensions of the SM to, for example, unify matter.[2] These extensions of the SM are called Beyond the Standard Model theories.

These BSM theories often lead to new particles and new types of interactions. Depending on the theory, these new particles can be very light or very heavy and have many different types of interactions with SM particles. These BSM theories can be tested in collider experiments such as at the LHC, since they can leave a trace in experimental observables like branching ratios or angular distributions of decay products. If the new heavy particles are not too heavy or their coupling to SM particles is not too small they even could be detected directly. Although we have an interesting set of measurements hinting towards new physics, the majority of current measurements agree with the SM predictions. Potential new physics models therefor are also heavily constrained. One BSM theory studied in detail is super-symmetry (SUSY)[34]. It was considered as one of the most promising (and elegant) extensions of the SM, however due to the lack of evidence found in LHC experiments it has become a much less popular theory to study. Luckily many other BSM theories exist.

In this chapter, the focus will be on one specific type of new particles that could account for the flavour anomalies covered in the previous chapter: Leptoquarks. At first an overview of a few different possible extensions of the SM will be given before diving more deeply into leptoquarks. At the end of the chapter a certain BSM model that produces, among others, leptoquarks will be worked out in detail: the 4321-model[15].

---

[1]The Standard Model was not designed as one model from scratch. It was a process taking decades where many theories were developed and later refuted by experiments, until a (largely) working theory of particle physics was found, which is now called the Standard Model of Particle Physics.

[2]In the SM there is no direct coupling between the two types of matter particles, quarks and leptons.

2.1 Possible extensions of the SM

In this section three different BSM particles or models will briefly be discussed that often are considered when searching for solutions to the observed anomalies. These BSM particles will be discussed one by one, however in many theories a combination of these is used. This will also be the case when considering the 4321-model later on in this chapter. A start will be made with extended Higgs models, followed by Z'-models and colorons. Leptoquarks will be covered in more detail in the next section. The extensions covered in this section are far from all possible extensions. To cover all of them would probably take a lifetime, if one would even be enough.

2.1.1 Extended Higgs models

The Higgs mechanism and the Higgs-boson are a key element to the SM, responsible for EWSB. The SM-Higgs is a single scalar doublet, which is the minimal scalar representation to be able to facilitate EWSB. It is possible to study more complicated Higgs representations. One of the most simple extensions of the Higgs-mechanism is to introduce multiple Higgs doublets, like the multiple generations in the fermionic sector. In addition one could introduce additional singlets or multiplets or even complex doublets[13, 35]. All these additions could introduce a wide variety of new phenomenology but are also constrained by the current measurements.

2.1.2 Z'-models

Another type of new particles are the neutral Z'-bosons. These Z'-bosons can be seen has the heavy cousins of the neutral Z-boson. However, in comparison with the Z-boson they can have a different coupling strength with respect to different generations of leptons or even couple to two different generations of leptons or quarks at one vertex in more general cases. Models with heavy Z'-bosons provide a relatively easy solution to the $R_{K^{(*)}}$ anomalies, but in some cases they can also give substantial contributions to $B_{(s)} \to \tau\mu$[36]. The Feynman diagram of such a contribution is drawn in Figure 2.1.

2.1.3 Colorons

Where the Z'-boson could be seen as the heavy cousin of the neutral Z-boson, colorons are the massive, flavour universal cousins of the gluons. These new massive gauge bosons originate from an extended strong gauge group that spontaneously breaks to QCD[37]. Although colorons do not give an explanation for the B-anomalies they are often present in BSM theories with extended high-energy gauge groups and for this reason they are briefly introduced here.

2.2 Leptoquarks

Leptoquarks (LQs) were postulated quite soon after the completion of the SM. They arise naturally from the unification of quarks and leptons as in the Pati-Salam theory[38]. Leptoquarks couple directly to a quark and a lepton, something that is not allowed in the SM.
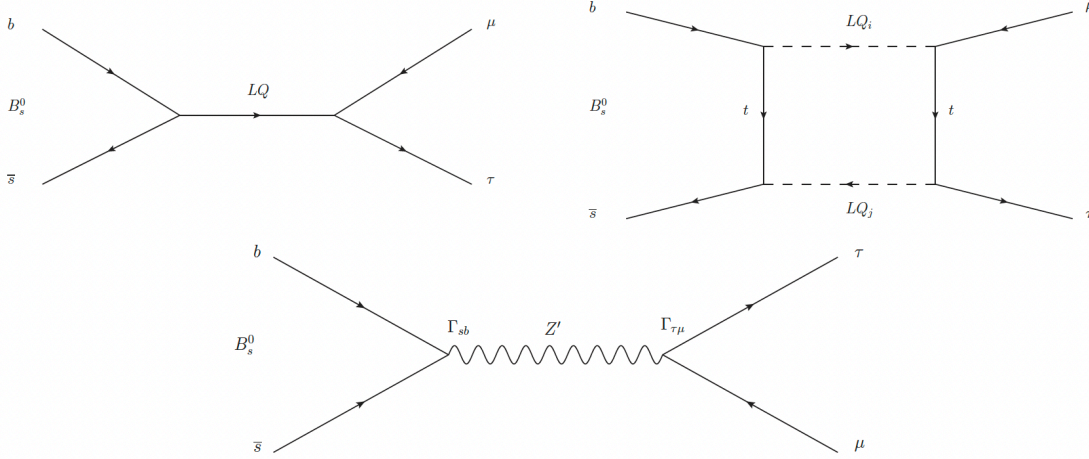
Figure 2.1: The Feynman diagrams for the contributions of a vector LQ (top left), scalar LQ (top right) and Z'-boson (bottom) to the decay of $B_{(s)} \to \tau\mu$.

Throughout the years many different types of leptoquarks, scalar (spin 0) or vector (spin 1), with different properties have been studied[14]. In this section more details will be given on LQs, since they are a prime candidate to account for the flavour anomalies and they are able to contribute significantly to the $B_{(s)} \to \tau\mu$ decay. The Feynman diagrams of the contribution to this decay of a scalar and a vector type LQ are drawn in Figure 2.1. Under the SM gauge group there are six types of scalar LQs and six types of vector LQs. The charges of the leptoquarks under the SM gauge group can be deduced from the charges of the quarks and leptons combined with the demand of gauge invariance of the Lagrangian. An overview of the possible LQ representations is given in [14]. These different LQs have different type of couplings to combinations of quarks and leptons and therefor lead to different phenomenology.

2.2.1   UV-completion: composite and gauge models

One can always postulate the existence of a certain type of leptoquark and study the effects its addition to the SM would have. However, it can be interesting to study theories at a very high energy that could produce these leptoquarks at low energy.[3] There are different types of UV-completions for leptoquarks that produce either a scalar or a vector LQ. Two types of UV-completions that are often considered and that will be considered here are composite models and gauge models.

In composite models leptoquarks are embedded as pseudo-Goldstone bosons in a composite Higgs model. One example of such a composite model producing scalar leptoquarks that could account for the B-anomalies can be found in [39]. In these composite models the LQs are produced as scalars.

In gauge models the leptoquarks are gauge bosons associated with some extended gauge group at higher energy. Then a spontaneous symmetry breaking (SSB) can be defined in

---

[3]The energies of SM processes are considered low energies at this scale.

such a way that, in one or more steps, the extended gauge groups are broken to the SM
gauge groups. These models produce the massive vector LQs in a similar way that EWSB
produces the massive W- and Z-bosons. In addition to vector leptoquarks other types of
BSM particles are postulated in these types of models, such as colorons and $Z^{'}$-bosons. The
model considered in the next section, the 4321-model, is an example of this second category.

2.3 A worked out example: 4321-model

In this section a specific NP model that could account for the current flavour anomalies will
be worked out and the implications of this model for the $B_{(s)} \to \tau\mu$ decay will be explored.
The model under consideration is a gauge leptoquark model, first introduced in [15] and
extended in [40]. In this section the results from these papers will be reproduced and the
calculations will be presented in more detail.
Starting from a higher gauge group a spontaneous symmetry breaking mechanism will be
defined, breaking the higher gauge group to the SM before EWSB, and the group-theoretical
aspects of this symmetry breaking will be covered. Then the gauge boson spectrum will be
studied, followed by construction of the interaction Lagrangian. At the end of the chapter
a brief insight into the flavour structure of the model will be given and the implications for
$B_{(s)} \to \tau\mu$ decay will be discussed. There was not enough time to work out these last two
topics in detail, so there the reasoning and information from [15, 40] will be presented.

2.3.1 Group theoretical aspects

The starting point will be the gauge group at UV energies: $G_{UV} \equiv SU(4) \times SU(3)^{'} \times SU(2)_L \times U(1)^{'}$. The respective real gauge fields and their corresponding gauge couplings
and generators are:

- H_μ^α, g_4 and T^α, with $\alpha = 1, ..., 15$

- $G_\mu^{'a}$, g_3 and T^a, with $a = 1, ..., 8$

- W_μ^i, g_2 and T^i, with $i = 1, 2, 3$

- $B_\mu^{'}$, g_1 and $Y^{'}$

Some symmetry breaking mechanism has to be defined to end up with the SM gauge group,
which is $G_{SM} = SU(3)_c \times SU(2)_L \times U(1)_Y$. Before the specific symmetry breaking will be
defined one can already gather information on the number of massive and massless gauge
bosons one expects to find based on the two gauge groups. If the gauge group is spon-
taneously broken from $G_1 \to G_2$ the number of massive gauge bosons in our theory is
$N_{dof}(G_1) - N_{dof}(G_2)$, while the number of massless gauge bosons is given by $N_{dof}(G_2)$[4]. In
our case $N_{dof}(G_{UV}) = 15 + 8 + 3 + 1$ and $N_{dof}(G_{SM}) = 8 + 3 + 1$. Therefore the expectation
is to find 15 degrees of freedom within the massive gauge bosons and 12 degrees of freedom
within the massless gauge bosons after the symmetry breaking to G_{SM}. In more technical

---

[4]The degrees of freedom of the $SU(N)$ and $U(N)$ gauge groups are given by $N^2 - 1$ and N respectively

terms: the Goldstone bosons of the symmetry breaking correspond to the coset space $\frac{G_{UV}}{G_{SM}}$. These Goldstone bosons get "eaten" by the massive gauge bosons.

Let us now define the specific structure of the symmetry breaking. The color charge, $SU(3)_c$, of the SM gauge group is embedded in the UV gauge group as $SU(3)_c = (SU(3)_4 \times SU(3)')_{\text{diag}}$ and the hypercharge, $U(1)_Y$, is embedded as $U(1)_Y = (U(1)_4 \times U(1)')_{\text{diag}}$. The groups $SU(3)_4$ and $U(1)_4$ are the $SU(3)$ and $U(1)$ subset of the $SU(4)$ gauge group at high energies. The SM hypercharge is defined as $Y = \sqrt{\frac{2}{3}}T^{15} + Y'$, where T^{15} is one of the $SU(4)$ generators.[5]

There are three scalar representations responsible for the symmetry breaking $G_{UV} \to G_{SM}$: $\Omega_1 = (\bar{4}, 1, 1, -1/2), \Omega_3 = (\bar{4}, 3, 1, 1/6)$ and $\Omega_{15} = (15, 1, 1, 0)$. Their decompositions under the SM gauge group are:

$$\Omega_1 = (\bar{3}, 1, -2/3) \oplus (1, 1, 0) \tag{2.1}$$
$$\Omega_3 = (8, 1, 0) \oplus (1, 1, 0) \oplus (3, 1, 2/3) \tag{2.2}$$
$$\Omega_{15} = (1, 1, 0) \oplus (3, 1, 2/3) \oplus (\bar{3}, 1, -2/3) \oplus (8, 1, 0). \tag{2.3}$$

It is possible to construct a scalar potential and study the scalar spectrum. This will not be done in this thesis, details can be found in the appendices of [40]. From constructing the scalar potential it is found that the scalars acquire non-zero vacuum expectation values (vevs):

$$\langle \Omega_1 \rangle = \frac{1}{\sqrt{2}} \begin{pmatrix} 0 \\ 0 \\ 0 \\ v_1 \end{pmatrix}, \tag{2.4}$$

$$\langle \Omega_3 \rangle = \frac{1}{\sqrt{2}} \begin{pmatrix} v_3 & 0 & 0 \\ 0 & v_3 & 0 \\ 0 & 0 & v_3 \\ 0 & 0 & 0 \end{pmatrix}, \tag{2.5}$$

$$\langle \Omega_{15} \rangle = v_{15} T^{15} = \frac{v_{15}}{2\sqrt{6}} \begin{pmatrix} 1 & 0 & 0 & 0 \\ 0 & 1 & 0 & 0 \\ 0 & 0 & 1 & 0 \\ 0 & 0 & 0 & -3 \end{pmatrix}, \tag{2.6}$$

$$\tag{2.7}$$

with T^{15} one of the $SU(4)$ generators. Similarly to the Higgs mechanism, once the scalars acquire their non-zero vev the the symmetry of the high-energy gauge theory is broken and reduced to a smaller gauge group. Even though the full symmetry of the high energy Lagrangian is broken when the scalars acquire their vev, two global $U(1)$-symmetries remain unbroken: $B = B' + \frac{1}{\sqrt{6}}T^{15}$ and $L = L' - \sqrt{\frac{2}{3}}T^{15}$. For the SM eigenstates these symmetries correspond to the baryon number and lepton number. Proton stability is protected and neutrinos remain massless due to these symmetries[40].

---

[5]The full list of $SU(4)$ generators can be found in appendix A

2.3.2 Gauge boson spectrum

To determine the gauge boson spectrum the covariant derivatives of the scalar representations must be constructed and the kinematic scalar terms have to be evaluated at the vacuum expectation value (vev). The covariant derivative of the scalar representations can be determined by considering its charges under the gauge group. It is important to note that Ω_1 and Ω_3 transform in the fundamental representation while Ω_{15} transforms in the adjoint representation. In general one can construct the covariant derivative in the fundamental representation as follows. Let the scalar representation Ω be charged under G_{UV} as $\Omega = (c_4, c_3, c_2, c_1)$. If one of the charges is zero (it does not transform under this gauge group) or one (it transforms trivially under this gauge group) no contribution to the covariant derivative will be present. However, if this is not the case the covariant derivative will be of the form:

$$D_\mu \Omega = (\partial_\mu - \frac{ig_4 c_4}{4} H_\mu^\alpha T^\alpha - \frac{ig_3 c_3}{3} G_\mu'^a T^a - \frac{ig_2 c_2}{2} W_\mu^i T^i - ig_1 c_1 B_\mu')\Omega. \tag{2.8}$$

The covariant derivative in the adjoint representation is defined differently. In this case the general covariant derivative is given by:

$$D_\mu \Omega = \partial_\mu \Omega - ig_4[T^\alpha, \Omega]H_\mu^\alpha - ig_3[T^a, \Omega]G_\mu'^a - ig_2[T^i, \Omega]W_\mu^i. \tag{2.9}$$

Applying this to our scalar representations one finds the following covariant derivatives:

$$D_\mu \Omega_1 = (\partial_\mu + ig_4 H_\mu^\alpha T^\alpha + \frac{1}{2}ig_1 B_\mu')\Omega_1, \tag{2.10}$$

$$D_\mu \Omega_3 = (\partial_\mu + ig_4 H_\mu^\alpha T^\alpha - ig_3 G_\mu'^a T^a - \frac{1}{6}ig_1 B_\mu')\Omega_3, \tag{2.11}$$

$$D_\mu \Omega_{15} = \partial_\mu \Omega_{15} - ig_4[T^\alpha, \Omega_{15}]H_\mu^\alpha. \tag{2.12}$$

Now the kinetic term at the vev of the respective scalar representations will be computed. They will be computed one by one, starting with $\langle \Omega_1 \rangle$.

Kinetic term of $\langle \Omega_1 \rangle$

$$(D_\mu \langle \Omega_1 \rangle)^\dagger (D^\mu \langle \Omega_1 \rangle) = (\partial_\mu \langle \Omega_1 \rangle + ig_4 H_\mu^\alpha T^\alpha \langle \Omega_1 \rangle + \frac{1}{2}ig_1 B_\mu' \langle \Omega_1 \rangle)^\dagger (\partial^\mu \langle \Omega_1 \rangle$$
$$+ ig_4 H^{\beta\mu} T^\beta \langle \Omega_1 \rangle + \frac{1}{2}ig_1 B'^\mu \langle \Omega_1 \rangle). \tag{2.13}$$

Making use of the fact that kinetic term of the scalar representation is evaluated in the vev one can make use of the fact that $\partial_\mu \langle \Omega_1 \rangle = 0$. This simplifies things a bit already. Besides this, one can simplify the expression some more. From eq. 2.4 one can see that the vevs are real: $\langle \Omega_1 \rangle^\dagger = \langle \Omega_1 \rangle^T$. In addition, since the gauge fields are real fields: $(H_\mu^\alpha)^\dagger = H_\mu^\alpha$[6] and the generators are Hermitian: i.e. $T^{\alpha\dagger} = T^\alpha$.

---

[6]The same holds for the gauge fields G and B'

$$
\begin{aligned}
(D_\mu \langle \Omega_1 \rangle)^\dagger (D^\mu \langle \Omega_1 \rangle) =& (ig_4 H_\mu^\alpha T^\alpha \langle \Omega_1 \rangle + \frac{1}{2} ig_1 B'_\mu \langle \Omega_1 \rangle)^\dagger (ig_4 H^{\beta\mu} T^\beta \langle \Omega_1 \rangle \\
& + \frac{1}{2} ig_1 B'^\mu \langle \Omega_1 \rangle) \\
=& (-ig_4 H_\mu^\alpha \langle \Omega_1 \rangle^T T^\alpha - \frac{1}{2} ig_1 \langle \Omega_1 \rangle^T B'_\mu)(ig_4 H^{\beta\mu} T^\beta \langle \Omega_1 \rangle \\
& + \frac{1}{2} ig_1 B'^\mu \langle \Omega_1 \rangle),
\end{aligned}
\tag{2.14}
$$

$$
\begin{aligned}
=& \overset{\text{\textcircled{1}}}{g_4^2 H_\mu^\alpha \langle \Omega_1 \rangle^T T^\alpha H^{\beta\mu} T^\beta \langle \Omega_1 \rangle} + \overset{\text{\textcircled{2}}}{\frac{1}{2} g_1 g_4 \langle \Omega_1 \rangle^T B'_\mu H^{\beta\mu} T^\beta \langle \Omega_1 \rangle} \\
& + \overset{\text{\textcircled{3}}}{\frac{1}{2} g_1 g_4 H_\mu^\alpha \langle \Omega_1 \rangle^T T^\alpha B'^\mu \langle \Omega_1 \rangle} + \overset{\text{\textcircled{4}}}{\frac{1}{4} g_1^2 \langle \Omega_1 \rangle^T B'_\mu B'^\mu \langle \Omega_1 \rangle}.
\end{aligned}
$$

A start can be made on simplifying the products between $\langle \Omega_1 \rangle$ and T^α. However first an additional index A is introduced to indicate a specific part of the $SU(4)$ generators, i.e. the index $A = 9, ..., 14$ spans over the $SU(4)/(SU(3)_4 \times U(1)_4)$ coset. If one considers the matrix representation of the generators T^α and $\langle \Omega_1 \rangle$ one can see that the only non-zero products are $\langle \Omega_1 \rangle T^A$, $T^A \langle \Omega_1 \rangle^T$, $\langle \Omega_1 \rangle T^{15}$ and $T^{15} \langle \Omega_1 \rangle^T$. Now these terms will be worked out one by one, starting with $\text{\textcircled{1}}$:

$$
\begin{aligned}
\text{\textcircled{1}} =& g_4^2 H_\mu^\alpha \langle \Omega_1 \rangle^T T^\alpha H^{\beta\mu} T^\beta \langle \Omega_1 \rangle, \\
=& g_4^2 \langle \Omega_1 \rangle^T (H_\mu^A T^A + H_\mu^{15} T^{15})(H^{B\mu} T^B + H^{15\mu} T^{15}) \langle \Omega_1 \rangle, \\
=& g_4^2 \langle \Omega_1 \rangle^T (H_\mu^A H^{B\mu} T^A T^B + H_\mu^A H^{15\mu} T^A T^{15} + H_\mu^{15} H^{B\mu} T^{15} T^B, \\
& + H_\mu^{15} H^{15\mu} T^{15} T^{15}) \langle \Omega_1 \rangle.
\end{aligned}
\tag{2.15}
$$

The different cases for the terms in $\text{\textcircled{1}}$ will be considered separately. The product $\langle \Omega_1 \rangle^T T^A T^B \langle \Omega_1 \rangle$ is non-zero for the case $A = B$. This will be shown explicitly for the case $A = B = 9$:

$$\langle\Omega_1\rangle^T T^9 T^9 \langle\Omega_1\rangle = \frac{1}{8}\begin{pmatrix}0\\0\\0\\v_1\end{pmatrix}^T\begin{pmatrix}0&0&0&1\\0&0&0&0\\0&0&0&0\\1&0&0&0\end{pmatrix}\begin{pmatrix}0&0&0&1\\0&0&0&0\\0&0&0&0\\1&0&0&0\end{pmatrix}\begin{pmatrix}0\\0\\0\\v_1\end{pmatrix},$$

$$= \frac{1}{8}\begin{pmatrix}0\\0\\0\\v_1\end{pmatrix}^T\begin{pmatrix}1&0&0&0\\0&0&0&0\\0&0&0&0\\0&0&0&1\end{pmatrix}\begin{pmatrix}0\\0\\0\\v_1\end{pmatrix},$$

$$= \frac{1}{8}\begin{pmatrix}0\\0\\0\\v_1\end{pmatrix}^T\begin{pmatrix}0\\0\\0\\v_1\end{pmatrix},$$

$$= \frac{v_1^2}{8}.$$

(2.16)

The case where $A \neq B$ is a bit more involved. The product $T^A T^B$ is only non-zero if $A = 9\,\&\,B = 10$, $A = 11\,\&\,B = 12$, $A = 13\,\&\,B = 14$ and vice versa. However the difference between the cases $A = 9, B = 10$ and $A = 10, B = 9$ amounts to precisely a minus sign. Since $H_\mu^9 H^{10\mu} = H^{10\mu} H_\mu^9$ [7] all terms combined for $A \neq B$ add up to zero. Next the terms $T^A T^{15}$ and $T^{15} T^B$ will be considered. Using a general form for the generators T^A, T^B one can show that these terms are zero as well for all A and B. For a general T^A:

$$\langle\Omega_1\rangle^T T^{15} T^A \langle\Omega_1\rangle = \frac{v_1^2}{4\sqrt{6}}\begin{pmatrix}0\\0\\0\\1\end{pmatrix}^T\begin{pmatrix}1&0&0&0\\0&1&0&0\\0&0&1&0\\0&0&0&-3\end{pmatrix}\begin{pmatrix}0&0&0&a\\0&0&0&b\\0&0&0&c\\\alpha&\beta&\gamma&0\end{pmatrix}\begin{pmatrix}0\\0\\0\\1\end{pmatrix},$$

$$= \frac{v_1^2}{4\sqrt{6}}\begin{pmatrix}0\\0\\0\\-3\end{pmatrix}^T\begin{pmatrix}a\\b\\c\\0\end{pmatrix} = 0.$$

(2.17)

Similarly for $T^{15} T^B$:

$$\langle\Omega_1\rangle^T T^{15} T^A \langle\Omega_1\rangle = \frac{v_1^2}{4\sqrt{6}}\begin{pmatrix}0\\0\\0\\1\end{pmatrix}^T\begin{pmatrix}0&0&0&a\\0&0&0&b\\0&0&0&c\\\alpha&\beta&\gamma&0\end{pmatrix}\begin{pmatrix}1&0&0&0\\0&1&0&0\\0&0&1&0\\0&0&0&-3\end{pmatrix}\begin{pmatrix}0\\0\\0\\1\end{pmatrix},$$

$$= \frac{v_1^2}{4\sqrt{6}}\begin{pmatrix}\alpha\\\beta\\\gamma\\0\end{pmatrix}^T\begin{pmatrix}0\\0\\0\\-3\end{pmatrix} = 0.$$

(2.18)

---

[7] They are components of the real gauge fields so they commute

Finally the $T^{15}T^{15}$-term will be considered:

$$
\begin{aligned}
\langle\Omega_1\rangle^T T^{15}T^{15}\langle\Omega_1\rangle =& \frac{v_1^2}{48}\begin{pmatrix}0\\0\\0\\1\end{pmatrix}^T \begin{pmatrix}1&0&0&0\\0&1&0&0\\0&0&1&0\\0&0&0&-3\end{pmatrix}\begin{pmatrix}1&0&0&0\\0&1&0&0\\0&0&1&0\\0&0&0&-3\end{pmatrix}\begin{pmatrix}0\\0\\0\\1\end{pmatrix}, \\
=& \frac{v_1^2}{48}\begin{pmatrix}0\\0\\0\\-3\end{pmatrix}^T \begin{pmatrix}0\\0\\0\\-3\end{pmatrix} = \frac{3v_1^2}{16}.
\end{aligned}
\tag{2.19}
$$

Combining all these results one finds for $\textcircled{1}$:

$$
\textcircled{1} = \frac{g_4^2 v_1^2}{8}H_\mu^A H^{A\mu} + \frac{3g_4^2 v_1^2}{16}H_\mu^{15}H^{15\mu}.
\tag{2.20}
$$

Continuing with the next terms from eq. 2.14, first $\textcircled{4}$ will be worked out, since it is a bit more straightforward.

$$
\begin{aligned}
\textcircled{4} =& + \frac{1}{4}g_1^2\langle\Omega_1\rangle^T B_\mu' B'^\mu\langle\Omega_1\rangle, \\
=& + \frac{g_1^2 v_1^2}{8}\begin{pmatrix}0\\0\\0\\1\end{pmatrix}^T\begin{pmatrix}0\\0\\0\\1\end{pmatrix} B_\mu' B'^\mu, \\
=& + \frac{g_1^2 v_1^2}{8}B_\mu' B'^\mu.
\end{aligned}
\tag{2.21}
$$

The terms $\textcircled{2}$ and $\textcircled{3}$ will be worked out together. Just as observed before the only indices of α, β one needs to consider are $\alpha = A$ or $\alpha = 15$ (similarly for β). The general structure of the $\langle\Omega_1\rangle$-generator products in $\textcircled{2}$ and $\textcircled{3}$ are of the form $\langle\Omega_1\rangle^T T^\alpha\langle\Omega_1\rangle$. One can immediately see that the only non-zero term will be for T^{15}. This simplifies the terms tremendously.

$$
\begin{aligned}
\textcircled{2}+\textcircled{3} =& \frac{1}{2}g_1 g_4\langle\Omega_1\rangle^T B_\mu' H^{\beta\mu}T^\beta\langle\Omega_1\rangle + \frac{1}{2}g_1 g_4 H_\mu^\alpha\langle\Omega_1\rangle^T T^\alpha B'^\mu\langle\Omega_1\rangle, \\
=& g_1 g_4 B_\mu' H^{15\mu}\langle\Omega_1\rangle^T T^{15}\langle\Omega_1\rangle, \\
=& \frac{-3g_1 g_4 v_1^2}{4\sqrt{6}}B_\mu' H^{15\mu}.
\end{aligned}
\tag{2.22}
$$

When all four terms are put together one finds that the kinetic term of Ω_1 evaluated in the vacuum expectation value is given by:

$$\boxed{(D_\mu \langle \Omega_1 \rangle)^\dagger (D^\mu \langle \Omega_1 \rangle) = \frac{g_4^2 v_1^2}{8} H_\mu^A H^{A\mu} + \frac{3 g_4^2 v_1^2}{16} H_\mu^{15} H^{15\mu} - \frac{3 g_1 g_4 v_1^2}{4\sqrt{6}} B_\mu' H^{15\mu} + \frac{g_1^2 v_1^2}{8} B_\mu' B'^\mu.}$$

$$(2.23)$$

The kinetic term of Ω_1 in the vev consists of 3 mass terms, the first, second and fourth terms, and one term mixing B_μ' and H_μ^{15}: the third term.

Kinetic term of $\langle \Omega_3 \rangle$

The next step is to study the kinetic term of $\langle \Omega_3 \rangle$, for which one needs to take the trace to ensure gauge invariance.

$$
\begin{aligned}
\text{Tr}[D_\mu \langle \Omega_3 \rangle)^\dagger (D^\mu \langle \Omega_3 \rangle)] =& \text{Tr}[((\partial_\mu + i g_4 H_\mu^\alpha T^\alpha - i g_3 G_\mu'^a T^a - \tfrac{1}{6} i g_1 B_\mu') \langle \Omega_3 \rangle)^\dagger \\
& \cdot ((\partial^\mu + i g_4 H^{\beta\mu} T^\beta - i g_3 G'^{b\mu} T^b - \tfrac{1}{6} i g_1 B'^\mu) \langle \Omega_3 \rangle)].
\end{aligned}
$$

$$(2.24)$$

As before one can omit the partial derivative terms, since $\partial_\mu \langle \Omega_3 \rangle = 0$. Besides this $\langle \Omega_3 \rangle^\dagger = \langle \Omega_3 \rangle^T$ and $T^\dagger = T$ and $H^\dagger = H$. Expanding the product within the trace will lead to nine terms, which will be considered one by one as before. These nine terms are:

$$
\begin{aligned}
\text{Tr}[D_\mu \langle \Omega_3 \rangle)^\dagger (D^\mu \langle \Omega_3 \rangle)] =& \text{Tr}[\; \overset{\text{①}}{g_4^2 H_\mu^\alpha H^{\beta\mu} \langle \Omega_3 \rangle^T T^\alpha T^\beta \langle \Omega_3 \rangle} - \overset{\text{②}}{g_4 g_3 H_\mu^\alpha G'^{b\mu} \langle \Omega_3 \rangle^T T^\alpha T^b \langle \Omega_3 \rangle} \\
& - \overset{\text{③}}{\frac{g_1 g_4}{6} H_\mu^\alpha B'^\mu \langle \Omega_3 \rangle^T T^\alpha \langle \Omega_3 \rangle} - \overset{\text{④}}{g_3 g_4 G_\mu'^a H^{\beta\mu} \langle \Omega_3 \rangle^T T^a T^\beta \langle \Omega_3 \rangle} \\
& + \overset{\text{⑤}}{g_3^2 G_\mu'^a G'^{b\mu} \langle \Omega_3 \rangle^T T^a T^b \langle \Omega_3 \rangle} + \overset{\text{⑥}}{\frac{g_1 g_3}{6} G_\mu'^a B'^\mu \langle \Omega_3 \rangle^T T^a \langle \Omega_3 \rangle} \\
& - \overset{\text{⑦}}{\frac{g_1 g_4}{6} B_\mu' H^{\beta\mu} \langle \Omega_3 \rangle^T T^\beta \langle \Omega_3 \rangle} + \overset{\text{⑧}}{\frac{g_1 g_3}{6} B_\mu' G'^{b\mu} \langle \Omega_3 \rangle^T T^b \langle \Omega_3 \rangle} \\
& + \overset{\text{⑨}}{\frac{g_1^2}{36} B_\mu' B'^\mu \langle \Omega_3 \rangle^T \langle \Omega_3 \rangle}].
\end{aligned}
$$

$$(2.25)$$

The cyclic and additive properties of the trace can be used to create a $\langle \Omega_3 \rangle \langle \Omega_3 \rangle^T$ product in each term.

$$\langle\Omega_3\rangle\langle\Omega_3\rangle^T = \frac{v_3}{\sqrt{2}} \begin{pmatrix} 1 & 0 & 0 \\ 0 & 1 & 0 \\ 0 & 0 & 1 \\ 0 & 0 & 0 \end{pmatrix} \frac{v_3}{\sqrt{2}} \begin{pmatrix} 1 & 0 & 0 & 0 \\ 0 & 1 & 0 & 0 \\ 0 & 0 & 1 & 0 \end{pmatrix},$$

$$= \frac{v_3^2}{2} \begin{pmatrix} 1 & 0 & 0 & 0 \\ 0 & 1 & 0 & 0 \\ 0 & 0 & 1 & 0 \\ 0 & 0 & 0 & 0 \end{pmatrix}.$$

(2.26)

In addition one can make use of some useful properties of the generators. The generators are traceless and normalised to $\text{Tr}[T^\alpha T^\beta] = \frac{1}{2}\delta^{\alpha\beta}$. At first the terms which are easiest to compute will be considered. Since the product $\langle\Omega_3\rangle^T\langle\Omega_3\rangle$ essentially is a three-by-three identity matrix, first the terms with the generators T^a will be worked out, as they only have entries in the same three-by-three space of the matrix, and the term without generators. These are the terms (5), (6), (8) and (9). The gauge fields and couplings are scalars and therefor they can be pulled out of the trace.

$$\begin{aligned}
\text{(5)} &= g_3^2 G_\mu'^a G'^{b\mu} \text{Tr}[\langle\Omega_3\rangle\langle\Omega_3\rangle^T T^a T^b], \\
&= \frac{g_3^2 v_3^2}{2} G_\mu'^a G'^{b\mu} \text{Tr}[T^a T^b], \\
&= \frac{g_3^2 v_3^2}{4} G_\mu'^a G'^{b\mu} \delta^{ab}, \\
&= \frac{g_3^2 v_3^2}{4} G_\mu'^a G'^{a\mu}.
\end{aligned}$$

(2.27)

$$\begin{aligned}
\text{(6)} &= \frac{g_1 g_3}{6} G_\mu'^a B'^\mu \text{Tr}[\langle\Omega_3\rangle\langle\Omega_3\rangle^T T^a], \\
&= \frac{g_1 g_3 v_3^2}{12} G_\mu'^a B'^\mu \text{Tr}[T^a] = 0.
\end{aligned}$$

(2.28)

$$\begin{aligned}
\text{(8)} &= \frac{g_1 g_3}{6} B_\mu' G'^{b\mu} \text{Tr}[\langle\Omega_3\rangle\langle\Omega_3\rangle^T T^b], \\
&= \frac{g_1 g_3 v_3^2}{12} B_\mu' G'^{b\mu} \text{Tr}[T^b] = 0.
\end{aligned}$$

(2.29)

$$\begin{aligned}
\text{(9)} &= \frac{g_1^2}{36} B_\mu' B'^\mu \text{Tr}[\langle\Omega_3\rangle^T\langle\Omega_3\rangle], \\
&= \frac{g_1^2 v_3^2}{24} B_\mu' B'^\mu.
\end{aligned}$$

(2.30)

Next the terms (3) and (7) will be covered together, as they have the same structure. The only generator with a non-zero contribution will be T^{15}. For $\alpha = 1, ..., 8$ the contribution is

zero as in the terms ⑥ and ⑧. For $\alpha = A$ the generator matrices have no entries on the diagonal so they will not contribute either. Since the $\langle\Omega_3\rangle^T \langle\Omega_3\rangle$ product produces an identity matrix in the $SU(3)_4$ subspace with a zero on the fourth diagonal element the product of $\langle\Omega_3\rangle^T \langle\Omega_3\rangle$ with T^{15} will not be traceless.

$$
\begin{aligned}
③ &= -\frac{g_1 g_4}{6} H_\mu^\alpha B'^\mu \operatorname{Tr}[\langle\Omega_3\rangle\langle\Omega_3\rangle^T T^\alpha], \\
&= -\frac{g_1 g_4 v_3^2}{12} H_\mu^{15} B'^\mu \operatorname{Tr}\left[\begin{pmatrix} 1 & 0 & 0 & 0 \\ 0 & 1 & 0 & 0 \\ 0 & 0 & 1 & 0 \\ 0 & 0 & 0 & 0 \end{pmatrix} T^{15}\right], \\
&= -\frac{g_1 g_4 v_3^2}{12} \frac{1}{2\sqrt{6}} H_\mu^{15} B'^\mu \operatorname{Tr}\left[\begin{pmatrix} 1 & 0 & 0 & 0 \\ 0 & 1 & 0 & 0 \\ 0 & 0 & 1 & 0 \\ 0 & 0 & 0 & 0 \end{pmatrix}\right], \\
&= -\frac{g_1 g_4 v_3^2}{8\sqrt{6}} H_\mu^{15} B'^\mu.
\end{aligned}
\tag{2.31}
$$

Identically one finds for ⑦:

$$
⑦ = -\frac{g_1 g_4 v_3^2}{8\sqrt{6}} B'_\mu H^{\mu 15}.
\tag{2.32}
$$

Next up are the terms ② and ④, which also have the same structure. For both terms two cases will be considered. At first the cases when $\alpha = a$ $(\beta = b)$ will be determined, followed by the case where $\alpha \neq a$ $(\beta \neq b)$. The first case:

$$
\begin{aligned}
②.1 &= -g_4 g_3 H_\mu^a G'^{b\mu} \operatorname{Tr}[\langle\Omega_3\rangle\langle\Omega_3\rangle^T T^a T^b], \\
&= -\frac{g_4 g_3 v_3^2}{2} H_\mu^a G'^{b\mu} \operatorname{Tr}[T^b \mathbb{1}_{3\times 3} T^a], \\
&= -\frac{g_4 g_3 v_3^2}{2} H_\mu^a G'^{b\mu} \operatorname{Tr}[T^b T^a], \\
&= -\frac{g_4 g_3 v_3^2}{4} H_\mu^a G'^{b\mu} \delta^{ab} = -\frac{g_4 g_3 v_3^2}{4} H_\mu^a G'^{a\mu}.
\end{aligned}
\tag{2.33}
$$

In the same manner one finds for ④.1 when $\beta = b$:

$$
④.1 = -\frac{g_4 g_3 v_3^2}{4} G'^a_\mu H^{a\mu}.
\tag{2.34}
$$

Now the second case will be considered, i.e. $\alpha \neq a$. As seen above one can incorporate the $SU(3)_4$ identity matrix into the T^a generator. By using the normalisation condition of the generators it can be seen that these contributions will vanish.

$$\begin{aligned}
\boxed{2.2} &= -g_4 g_3 H^\alpha_\mu G'^{b\mu} \operatorname{Tr}[\langle\Omega_3\rangle\langle\Omega_3\rangle^T T^\alpha T^b], \\
&= -\frac{g_4 g_3 v_3^2}{2} H^\alpha_\mu G'^{b\mu} \operatorname{Tr}[T^b \mathbb{1}_{3\times 3} T^\alpha], \\
&= -\frac{g_4 g_3 v_3^2}{2} H^\alpha_\mu G'^{b\mu} \operatorname{Tr}[T^b T^\alpha], \\
&= -\frac{g_4 g_3 v_3^2}{4} H^a_\mu G'^{b\mu} \delta^{a\alpha} = 0.
\end{aligned} \tag{2.35}$$

The exact same holds for $\beta \neq b$ in $\boxed{4.2}$. The final term to work out is $\boxed{1}$. For this term one needs to consider multiple cases for the different values α and β can take. Many of these cases lead to a zero contribution for reasons encountered previously. Those cases will not be worked out again. To prevent showing the same calculations again only the non-zero contributions and the zero-contributions with a novel origin will be considered. These cases are:

1. $\alpha = a$ & $\beta = b$

2. $\alpha = 15$ & $\beta = 15$

3. $\alpha = \beta = A$

4. $\alpha = A$ & $\beta = B$

Starting with $\boxed{1.1}$, a similar structure is found as encountered before in term $\boxed{5}$:

$$\begin{aligned}
\boxed{1.1} &= g_4^2 H^a_\mu H^{b\mu} \operatorname{Tr}[\langle\Omega_3\rangle\langle\Omega_3\rangle^T T^a T^b], \\
&= \frac{g_4^2 v_3^2}{2} H^a_\mu H^{b\mu} \operatorname{Tr}[T^a T^b] = \frac{g_4^2 v_3^2}{4} H^a_\mu H^{a\mu}.
\end{aligned} \tag{2.36}$$

For $\boxed{1.2}$ one need to take few additional steps:

$$\begin{aligned}
\boxed{1.2} &= g_4^2 H^{15}_\mu H^{15\mu} \operatorname{Tr}[\langle\Omega_3\rangle\langle\Omega_3\rangle^T T^{15} T^{15}], \\
&= \frac{g_4^2 v_3^2}{48} H^{15}_\mu H^{15\mu} \operatorname{Tr}\left[\begin{pmatrix} 1 & 0 & 0 & 0 \\ 0 & 1 & 0 & 0 \\ 0 & 0 & 1 & 0 \\ 0 & 0 & 0 & 0 \end{pmatrix}\begin{pmatrix} 1 & 0 & 0 & 0 \\ 0 & 1 & 0 & 0 \\ 0 & 0 & 1 & 0 \\ 0 & 0 & 0 & -3 \end{pmatrix}\begin{pmatrix} 1 & 0 & 0 & 0 \\ 0 & 1 & 0 & 0 \\ 0 & 0 & 1 & 0 \\ 0 & 0 & 0 & -3 \end{pmatrix}\right], \\
&= \frac{g_4^2 v_3^2}{48} H^{15}_\mu H^{15\mu} \operatorname{Tr}\left[\begin{pmatrix} 1 & 0 & 0 & 0 \\ 0 & 1 & 0 & 0 \\ 0 & 0 & 1 & 0 \\ 0 & 0 & 0 & 0 \end{pmatrix}\right] = \frac{g_4^2 v_3^2}{16} H^{15}_\mu H^{15\mu}.
\end{aligned} \tag{2.37}$$

Next up is the third case, where $\alpha = \beta = A$. Here one can make use of the fact that $\text{Tr}[\langle\Omega_3\rangle^T\langle\Omega_3\rangle T^A T^A] = \frac{v_3^2}{8}$. This can be checked for every A by computing the matrix products.[8] This then gives the following contribution:

$$
\begin{aligned}
\boxed{1.3} &= g_4^2 H_\mu^A H^{A\mu}\, \text{Tr}[\langle\Omega_3\rangle\langle\Omega_3\rangle^T T^A T^A], \\
&= \frac{g_4^2 v_3^2}{8} H_\mu^A H^{A\mu}.
\end{aligned}
\tag{2.38}
$$

Finally the fourth case will be considered, where $\alpha = A$ and $\beta = B \neq A$. This case will lead to a zero contribution to the overall kinetic term. It will be shown that this contribution vanishes for two combinations of A and B. The other combinations are completely analogous. At first one needs the sum of $A = 9\,\&\,B = 10$ and $A = 10\,\&\,B = 9$:

$$
\boxed{1.4.\text{a}} = g_4^2 H_\mu^9 H^{10\mu}\, \text{Tr}[\langle\Omega_3\rangle\langle\Omega_3\rangle^T (T^9 T^{10} + T^{10} T^9)].
\tag{2.39}
$$

Computing this sum, $T^9 T^{10} + T^{10} T^9$, gives:

$$
\begin{aligned}
T^9 T^{10} + T^{10} T^9 &= \begin{pmatrix} 0 & 0 & 0 & 1 \\ 0 & 0 & 0 & 0 \\ 0 & 0 & 0 & 0 \\ 1 & 0 & 0 & 0 \end{pmatrix} \begin{pmatrix} 0 & 0 & 0 & -i \\ 0 & 0 & 0 & 0 \\ 0 & 0 & 0 & 0 \\ i & 0 & 0 & 0 \end{pmatrix} + \begin{pmatrix} 0 & 0 & 0 & -i \\ 0 & 0 & 0 & 0 \\ 0 & 0 & 0 & 0 \\ i & 0 & 0 & 0 \end{pmatrix} \\
&\quad \cdot \begin{pmatrix} 0 & 0 & 0 & 1 \\ 0 & 0 & 0 & 0 \\ 0 & 0 & 0 & 0 \\ 1 & 0 & 0 & 0 \end{pmatrix}, \\
&= \begin{pmatrix} i & 0 & 0 & 0 \\ 0 & 0 & 0 & 0 \\ 0 & 0 & 0 & 0 \\ 0 & 0 & 0 & -i \end{pmatrix} + \begin{pmatrix} -i & 0 & 0 & 0 \\ 0 & 0 & 0 & 0 \\ 0 & 0 & 0 & 0 \\ 0 & 0 & 0 & i \end{pmatrix} = 0.
\end{aligned}
\tag{2.40}
$$

This term will not contribute to the kinetic term. As mentioned before the same holds for the sums of 11 & 12 and 13 & 14. Finally, if one would have the combination $A = 9$ and $B = 11$ and vice versa one would end up with the sum $T^9 T^{11} + T^{11} T^9$. If this sum is computed one finds:

---

[8]This is very straightforward to check and therefor it will not be worked out in detail here.

$$T^9 T^{10} + T^{10} T^9 = \begin{pmatrix} 0 & 0 & 0 & 1 \\ 0 & 0 & 0 & 0 \\ 0 & 0 & 0 & 0 \\ 1 & 0 & 0 & 0 \end{pmatrix} \begin{pmatrix} 0 & 0 & 0 & 0 \\ 0 & 0 & 0 & 1 \\ 0 & 0 & 0 & 0 \\ 0 & 1 & 0 & 0 \end{pmatrix} + \begin{pmatrix} 0 & 0 & 0 & 0 \\ 0 & 0 & 0 & 1 \\ 0 & 0 & 0 & 0 \\ 0 & 1 & 0 & 0 \end{pmatrix}$$

$$\cdot \begin{pmatrix} 0 & 0 & 0 & 1 \\ 0 & 0 & 0 & 0 \\ 0 & 0 & 0 & 0 \\ 1 & 0 & 0 & 0 \end{pmatrix},$$

$$= \begin{pmatrix} 0 & 1 & 0 & 0 \\ 0 & 0 & 0 & 0 \\ 0 & 0 & 0 & 0 \\ 0 & 0 & 0 & 0 \end{pmatrix} + \begin{pmatrix} 0 & 0 & 0 & 0 \\ 1 & 0 & 0 & 0 \\ 0 & 0 & 0 & 0 \\ 0 & 0 & 0 & 0 \end{pmatrix} = \begin{pmatrix} 0 & 1 & 0 & 0 \\ 1 & 0 & 0 & 0 \\ 0 & 0 & 0 & 0 \\ 0 & 0 & 0 & 0 \end{pmatrix}. \tag{2.41}$$

As there are no diagonal entries, the trace will be zero and therefor the entire contribution will vanish. The same holds for all other combinations. So in the end the total contribution from ① to the kinetic term is:

$$① = \frac{g_4^2 v_3^2}{4} H_\mu^a H^{a\mu} + \frac{g_4^2 v_3^2}{8} H_\mu^A H^{A\mu} + \frac{g_4^2 v_3^2}{16} H_\mu^{15} H^{15\mu}. \tag{2.42}$$

All separate terms of the kinetic term of $\langle \Omega_3 \rangle$ are evaluated. Putting all contributions together the following expression is found:

$$\boxed{\begin{aligned} \mathrm{Tr}[(D_\mu \langle \Omega_3 \rangle)^\dagger (D^\mu \langle \Omega_3 \rangle)] = & \frac{g_4^2 v_3^2}{4} H_\mu^a H^{a\mu} + \frac{g_4^2 v_3^2}{8} H_\mu^A H^{A\mu} + \frac{g_4^2 v_3^2}{16} H_\mu^{15} H^{15\mu} \\ & - \frac{g_4 g_3 v_3^2}{2} H_\mu^a G'^{a\mu} - \frac{g_1 g_4 v_3^2}{4\sqrt{6}} H_\mu^{15} B'^\mu \\ & + \frac{g_3^2 v_3^2}{4} G_\mu'^a G'^{a\mu} + \frac{g_1^2 v_3^2}{24} B_\mu' B'^\mu. \end{aligned}} \tag{2.43}$$

The kinetic term of Ω_3 in the vev consists of 5 mass and two mixing terms, mixing B_μ' with H_μ^{15} and H_μ^a with $G_\mu'^a$.

Kinetic term of $\langle \Omega_{15} \rangle$

The kinetic term of $\langle \Omega_{15} \rangle$ still needs to be calculated. Just as for $\langle \Omega_3 \rangle$ it is necessary to take the trace, but in addition an additional factor $\frac{1}{2}$ is needed since Ω_{15} transforms in the adjoint representation. The first step is to compute the commutator in the covariant derivative. Since $\langle \Omega_{15} \rangle$ is given by one of the $SU(4)$ commutators one can use the commutation relations between $SU(4)$ generators:

$$[T^\alpha, T^\beta] = i f^{\alpha \beta \gamma} T^\gamma, \tag{2.44}$$

where $f^{\alpha \beta \gamma}$ are the fully anti-symmetric structure constants of $SU(4)$. In [40] a list of the non-zero structure constants is given. The non-zero structure constants of interest in our case

are $f^{9\,10\,15}$, $f^{11\,12\,15}$ and $f^{13\,14\,15}$, all with a value of $\sqrt{\frac{2}{3}}$. Computing the commutator between T^{15} and T^{α} gives:

$$
\begin{aligned}
\left[T^{\alpha}, T^{15}\right] &= i f^{\alpha\,15\,\gamma} T^{\gamma} = i f^{A\,15\,\gamma} T^{\gamma} = -i f^{A\,\gamma\,15} T^{\gamma} \\
&= i\sqrt{\frac{2}{3}} \left(T^{9} - T^{10} + T^{11} - T^{12} + T^{13} - T^{14}\right).
\end{aligned}
\tag{2.45}
$$

All ingredients are now present to start the computation of the kinetic term of $\langle \Omega_{15} \rangle$. As with $\langle \Omega_1 \rangle$ and $\langle \Omega_3 \rangle$ the partial derivative is zero, so this term will not be considered. The following expression is found:

$$
\begin{aligned}
\frac{1}{2}\mathrm{Tr}[(D_{\mu}\langle \Omega_{15}\rangle)^{\dagger}(D^{\mu}\langle \Omega_{15}\rangle)] &= \frac{1}{2}\mathrm{Tr}\left[\left(ig_4 v_{15} H_{\mu}^{\alpha}\left[T^{15}, T^{\alpha}\right]\right)\left(-ig_4 v_{15} H^{\beta\mu}\left[T^{\beta}, T^{15}\right]\right)\right], \\
&= \frac{1}{2}g_4^2 v_{15}^2 \mathrm{Tr}\left[\left(-iH_{\mu}^{\alpha}\left[T^{\alpha}, T^{15},\right]\right)\left(-iH^{\beta\mu}\left[T^{\beta}, T^{15}\right]\right)\right], \\
&= -\frac{1}{2}g_4^2 v_{15}^2 \mathrm{Tr}\left[\left(H_{\mu}^{A}\left[T^{A}, T^{15},\right]\right)\left(H^{B\mu}\left[T^{B}, T^{15}\right]\right)\right].
\end{aligned}
\tag{2.46}
$$

Using the results for the commutator from above one finds:

$$
\begin{aligned}
&= -\frac{1}{2}g_4^2 v_{15}^2 H_{\mu}^{A} H^{B\mu}\mathrm{Tr}\left[i\sqrt{\frac{2}{3}}\left(T^{9} - T^{10} + T^{11} - T^{12} + T^{13} - T^{14}\right)\right. \\
&\qquad \left. i\sqrt{\frac{2}{3}}\left(T^{9} - T^{10} + T^{11} - T^{12} + T^{13} - T^{14}\right)\right], \\
&= \frac{1}{3}g_4^2 v_{15}^2 H_{\mu}^{A} H^{B\mu}\frac{1}{2}\delta^{AB},
\end{aligned}
\tag{2.47}
$$

where again the relation $\mathrm{Tr}[T^{\alpha}T\beta] = \frac{1}{2}\delta^{\alpha\beta}$ is used. In the end one finds for the kinetic term of $\langle \Omega_{15} \rangle$:

$$
\boxed{\frac{1}{2}\mathrm{Tr}[(D_{\mu}\langle \Omega_{15}\rangle)^{\dagger}(D^{\mu}\langle \Omega_{15}\rangle)] = \frac{g_4^2 v_{15}^2}{6}H_{\mu}^{A} H^{A\mu}.}
\tag{2.48}
$$

The kinetic term of Ω_{15} in the vev only consists of a mass term for H_{μ}^{A}.

Mass eigenstates of the gauge bosons

All ingredients are now ready to compute the full gauge boson spectrum and the mass eigenstates. At first all three kinetic terms, i.e. eq. 2.23, eq. 2.43 and eq. 2.48 are combined. One can already see that there are some fixed combinations of gauge fields in the kinetic terms. Rewriting the expression in a more convenient form yields:

$$
(D_\mu \langle \Omega_1 \rangle)^\dagger (D^\mu \langle \Omega_1 \rangle) + \mathrm{Tr}[(D_\mu \langle \Omega_3 \rangle)^\dagger (D^\mu \langle \Omega_3 \rangle)] + \frac{1}{2} \mathrm{Tr}[(D_\mu \langle \Omega_{15} \rangle)^\dagger (D^\mu \langle \Omega_{15} \rangle)]
$$

$$
= \frac{g_4^2}{8} \left(v_1^2 + v_3^2 + \frac{4v_{15}^2}{3} \right) H_\mu^A H^{A\mu} + \frac{v_3^2}{4} \left(g_4^2 H_\mu^a H^{a\mu} - 2g_4 g_3 H_\mu^a G'^{a\mu} + g_3^2 G_\mu'^a G'^{a\mu} \right) +
$$

$$
\frac{g_4^2}{16} \left(3v_1^2 + v_3^2 \right) H_\mu^{15} H^{15\mu} - \frac{g_1 g_4}{4\sqrt{6}} \left(3v_1^2 + v_3^2 \right) H_\mu^{15} B'^\mu + \frac{g_1^2}{24} \left(3v_1^2 + v_3^2 \right) B_\mu' B'^\mu,
\tag{2.49}
$$

$$
= \frac{g_4^2}{8} \left(v_1^2 + v_3^2 + \frac{4v_{15}^2}{3} \right) H_\mu^A H^{A\mu} + \frac{v_3^2}{4} \begin{pmatrix} H_\mu^a & G_\mu'^a \end{pmatrix} \begin{pmatrix} g_4^2 & -g_3 g_4 \\ -g_4 g_3 & g_3^2 \end{pmatrix} \begin{pmatrix} H^{a\mu} \\ G'^{a\mu} \end{pmatrix}
$$

$$
+ \frac{3v_1^2 + v_3^2}{8} \begin{pmatrix} H_\mu^{15} & B_\mu' \end{pmatrix} \begin{pmatrix} \frac{g_4^2}{2} & \frac{-g_1 g_4}{\sqrt{6}} \\ \frac{-g_1 g_4}{\sqrt{6}} & \frac{g_1^2}{3} \end{pmatrix} \begin{pmatrix} H^{15\mu} \\ B'^\mu \end{pmatrix}.
$$

To find the mass eigenstates of the gauge boson the matrices need to be diagonalised and the eigenvectors and eigenvalues have to be found. Luckily the matrices are only two by two matrices, making this procedure fairly straightforward. At first the $H_\mu^A H^{A\mu}$-term is considered, since no eigenvectors and values have to be computed. A complex gauge field $U_\mu^{1,2,3}$ is introduced:

$$
\boxed{U_\mu^{1,2,3} = \frac{1}{\sqrt{2}} \left(H_\mu^{9,11,13} - i\, H_\mu^{10,12,14} \right), \quad m_U^2 = \frac{g_4^2}{4} \left(v_1^2 + v_3^2 + \frac{4v_{15}^2}{3} \right).}
\tag{2.50}
$$

The corresponding mass term in the Lagrangian will have the form:

$$
\mathcal{L}_{m_U} = \frac{1}{2} m_U^2 U^{i\mu\dagger} U_\mu^i.
\tag{2.51}
$$

The mass eigenstates of the other gauge bosons will require some additional calculations. The matrices will be diagonalised and the eigenvector and eigenvalues will be used to find the diagonal decomposition. To be more precise, one can make use of the fact that $M = SDS^{-1}$, where $D = \mathrm{diag}[\lambda_1, \lambda_2]$ with λ_i being the eigenvalues and $S = (v_1, v_2)$ with v_i being the eigenvector corresponding to the ith eigenvalue. Using the matrices S and its inverse S^{-1} one can then find the mass eigenstates. For the $H_\mu^a, G'^{a\mu}$-term:

$$
M = \begin{pmatrix} g_4^2 & -g_3 g_4 \\ -g_4 g_3 & g_3^2 \end{pmatrix} = \frac{1}{g_3^2 + g_4^2} \begin{pmatrix} g_3 & g_4 \\ g_4 & -g_3 \end{pmatrix} \begin{pmatrix} 0 & 0 \\ 0 & g_3^2 + g_4^2 \end{pmatrix} \begin{pmatrix} g_3 & g_4 \\ g_4 & -g_3 \end{pmatrix}.
\tag{2.52}
$$

With this decomposition one finds the following mass eigenstates and corresponding masses:

$$
\boxed{\begin{aligned}
g_\mu^a &= \frac{g_3 H_\mu^a + g_4 G'^a{}_\mu}{\sqrt{g_3^2 + g_4^2}}, \quad m_g^2 = 0, \\
g_\mu'^a &= \frac{g_4 H_\mu^a - g_3 G'^a{}_\mu}{\sqrt{g_3^2 + g_4^2}}, \quad m_{g'}^2 = \frac{v_3^2}{2} \left(g_3^2 + g_4^2 \right).
\end{aligned}}
\tag{2.53}
$$

Similarly one finds for the H_μ^{15}, B'^μ-term:

$$M = \begin{pmatrix} \frac{g_4^2}{2} & \frac{-g_1 g_4}{\sqrt{6}} \\ \frac{-g_1 g_4}{\sqrt{6}} & \frac{g_1^2}{3} \end{pmatrix},$$

$$= \frac{\sqrt{\frac{2}{3}}}{g_4^2 + \frac{2}{3}g_1^2} \begin{pmatrix} \sqrt{\frac{2}{3}}g_1 & \sqrt{\frac{3}{2}}g_4 \\ g_4 & -g_1 \end{pmatrix} \begin{pmatrix} 0 & 0 \\ 0 & \frac{1}{3}\left(g_1^2 + \frac{3}{2}g_4^2\right) \end{pmatrix} \begin{pmatrix} g_1 & \sqrt{\frac{3}{2}}g_4 \\ g_4 & -\sqrt{\frac{2}{3}}g_1 \end{pmatrix}. \tag{2.54}$$

Leading to the following mass eigenstates:

$$\boxed{\begin{aligned} B_\mu &= \frac{\sqrt{\frac{2}{3}}g_1 H_\mu^{15} + g_4 B'_\mu}{\sqrt{g_4^2 + \frac{2}{3}g_1^2}}, \quad m_B^2 = 0, \\ Z'_\mu &= \frac{g_4 H_\mu^{15} - \sqrt{\frac{2}{3}}g_1 B'_\mu}{\sqrt{g_4^2 + \frac{2}{3}g_1^2}}, \quad m_{Z'}^2 = \frac{v_3^2}{2}\left(g_3^2 + g_4^2\right). \end{aligned}} \tag{2.55}$$

In the beginning of this chapter the claim was made that based on the specific structure of the symmetry breaking 15 massive and 12 massless degrees of freedom should be present within the gauge boson spectrum. This claim can now easily be checked. Three complex massive gauge fields were found, $U_\mu^{1,2,3}$, containing 6 massive degrees of freedom. In addition nine massive real gauge boson fields, Z'_μ and $g_\mu'^a$, were found giving us a total of 15 degrees of freedom within the massive gauge bosons as was expected. In addition nine new massless real gauge bosons were found, B_μ and g_μ^a, which together with the three massless, real $SU(2)$ gauge bosons contain a total of 12 massless degrees of freedom. The predictions based on the group structure of the symmetry breaking correspond to the outcome of the explicit calculation.

2.3.3 Fermion-boson interaction Lagrangian

The next step in our study of the 4321-model is the fermion-boson interaction Lagrangian. In particular the interactions between the fermions and the new massive gauge bosons are of interest. The interaction Lagrangian of our model can be derived by studying the Dirac equation for all fermions in our model. For a general fermion Ψ the Dirac equation is given by

$$\mathcal{L}_{dirac} = \bar{\Psi}(i\gamma^\mu D_\mu)\Psi. \tag{2.56}$$

First an overview of all fermions in our model will be created. All SM fermions are singlets under $SU(4)$, so to introduce the interaction between the SM fermions and the new leptoquark additional heavy vector-like fermions, $\Psi_L^i = (Q'_L, L'_L)^T, \Psi_R^i = (Q'_R, L'_R)^T$ are introduced. These heavy vector-like fermions mix with the SM-like fermions when $\Omega_{1,3}$ goes to its VEV. Under the SM gauge group the charges of $Q'_{L,R}$ and $L'_{L,R}$ are $(3, 2, 1/6)$ and $(1, 2, -1/2)$ respectively. In Table 2.1 an overview of all fermions in our theory with their charges under the gauge groups is given. Besides $\Psi_{L,R}^i$ the fermions are the SM fermions as

Table 2.1: All fermions in our theory with the charges under the gauge groups.

Fermion	$(SU(4), SU(3)', SU(2)_L, U(1)')$
$q_L^{'i}$	(1,3,2,1/6)
$u_R^{'i}$	(1,3,1,2/3)
$d_R^{'i}$	(1,3,1,-1/3)
$\ell_L^{'i}$	(1,1,2,-1/2)
$e_R^{'i}$	(1,1,1,-1)
Ψ_L^i	(4,1,2,0)
Ψ_R^i	(4,1,2,0)

defined in Section 1.1, with the addition of being a singlet of the $SU(4)$ gauge group. Just as q_L' and ℓ_L' both Q_L' and L_L' are doublets.

In addition it is instructive to write the interaction Lagrangian in terms of the mass eigenstates of the gauge bosons. For that reason $H_\mu^\alpha, G_\mu^{'\alpha}$ and B_μ' are written in terms of $U_\mu^i, g_\mu^a, g_\mu^{'a}, Z_\mu'$ and B_μ. This leads to the following expressions for the gauge bosons:

$$H_\mu^a = \frac{g_4}{\sqrt{g_3^2 + g_4^2}} g_\mu^{'a} + \frac{g_3}{\sqrt{g_3^2 + g_4^2}} g_\mu^a,$$

$$G_\mu^{'a} = \frac{g_4}{\sqrt{g_3^2 + g_4^2}} g_\mu^a - \frac{g_3}{\sqrt{g_3^2 + g_4^2}} g_\mu^{'a},$$

$$B_\mu' = \frac{g_4}{\sqrt{g_4^2 + \frac{2}{3}g_1^2}} B_\mu - \sqrt{\frac{2}{3}} \frac{g_1}{\sqrt{g_4^2 + \frac{2}{3}g_1^2}} Z_\mu',$$

$$H_\mu^{15} = \frac{g_4}{\sqrt{g_4^2 + \frac{2}{3}g_1^2}} Z_\mu' + \sqrt{\frac{2}{3}} \frac{g_1}{\sqrt{g_4^2 + \frac{2}{3}g_1^2}} B_\mu, \tag{2.57}$$

$$H_\mu^{9,11,13} = \frac{1}{\sqrt{2}} \left(U_\mu^{1,2,3} + U_\mu^{*1,2,3} \right),$$

$$H_\mu^{10,12,14} = \frac{i}{\sqrt{2}} \left(U_\mu^{1,2,3} - U_\mu^{*1,2,3} \right).$$

The covariant derivative for each fermion in our model can be constructed in the same way as done for the scalars in the previous section. Evaluating the Dirac Lagrangian for each fermion with the corresponding covariant derivative will yield the fermion-boson interaction Lagrangian. In addition, constructing the covariant derivative of a SM-like fermion that has a trivial transformation under $SU(4)$ allows one to match the couplings g_1, g_3 and g_4 to the SM couplings g_s and g_Y. Considering the covariant derivative of u_R':

$$D_\mu u_R^{'} = \partial_\mu u_R^{'} - ig_3 G_\mu^{'a} T^a u_R^{'} - i\frac{2}{3}g_1 B_\mu^{'} u_R^{'},$$

$$\subset \partial_\mu u_R^{'} - i\frac{g_3 g_4}{\sqrt{g_3^2 + g_4^2}} g_\mu^a T^a u_R^{'} - i\frac{2}{3}\frac{g_1 g_4}{\sqrt{g_4^2 + \frac{2}{3}g_1^2}} B_\mu u_R^{'}. \tag{2.58}$$

In the second line the subset of the $SU(3)_c \times U(1)_Y$ fields was considered. Matching the 4321-model couplings to the SM couplings yields:

$$g_s = \frac{g_4 g_3}{\sqrt{g_4^2 + g_3^2}}, \tag{2.59}$$

$$g_Y = \frac{g_4 g_1}{\sqrt{g_4^2 + \frac{2}{3}g_1^2}}. \tag{2.60}$$

The two equations above will be applied in the interaction Lagrangian. Therefore again the expressions of the gauge bosons will be given, as in eq. 2.3.3, but with the two equations above applied:

$$H_\mu^a = \frac{g_s}{g_3}g_\mu^{'a} + \frac{g_s}{g_4}g_\mu^a,$$

$$G_\mu^{'a} = \frac{g_s}{g_3}g_\mu^a - \frac{g_s}{g_4}g_\mu^{'a},$$

$$B_\mu^{'} = \frac{g_Y}{g_1}B_\mu - \sqrt{\frac{2}{3}}\frac{g_Y}{g_4}Z_\mu^{'},$$

$$H_\mu^{15} = \frac{g_Y}{g_1}Z_\mu^{'} + \sqrt{\frac{2}{3}}\frac{g_Y}{g_4}B_\mu, \tag{2.61}$$

$$H_\mu^{9,11,13} = \frac{1}{\sqrt{2}}\left(U_\mu^{1,2,3} + U_\mu^{*1,2,3}\right),$$

$$H_\mu^{10,12,14} = \frac{i}{\sqrt{2}}\left(U_\mu^{1,2,3} - U_\mu^{*1,2,3}\right).$$

The interaction Lagrangian will be constructed separately for left handed and right handed interactions. In addition our interest is solely in the interactions with the new heavy gauge bosons U_μ, $g_\mu^{'}$ and $Z_{mu}^{'}$. The interactions with all other gauge bosons will be omitted, since they are already present in the SM interaction Lagrangian. The kinetic terms of the fermions will not be considered either.

Left-handed interaction Lagrangian

To find the full left-handed interaction Lagrangian, $\mathcal{L}_{dirac}$ will be calculated for each left-handed fermion and all contributions will be added up. Starting with $\mathcal{L}_{dirac}$ of Ψ_L, which contains both quarks and leptons:

$$\mathcal{L}_{dirac} = \bar{\Psi}_L(i\gamma^\mu D_\mu)\Psi_L,$$

$$= \bar{\Psi}_L(i\gamma^\mu \cdot -ig_4 H_\mu^\alpha T_\mu^\alpha)\Psi_L. \tag{2.62}$$

As before the sum will be split over α in the indices $a = 1, ..., 8$ and $A = 9, ..., 15$. Starting with $T^\alpha H_\mu^\alpha$:

$$\mathcal{L}_{dirac} \subset \bar{\Psi}_L (i\gamma^\mu \cdot - ig_4 H_\mu^a T_\mu^a)\Psi_L,$$
$$= \frac{g_4 g_s}{g_3}\left(\bar{Q}'_L, \bar{L}'_L\right)\gamma^\mu T^a \begin{pmatrix} Q'_L \\ L'_L \end{pmatrix} g_\mu^{'a}, \tag{2.63}$$
$$= \frac{g_4 g_s}{g_3}\bar{Q}'_L \gamma^\mu T^a Q'_L g_\mu^{'a}.$$

Using the matrix form of the generators T^A and the gauge bosons H_μ^A in terms of U_μ^i and U_μ^{i*} one can work out the sum over the index A. As an example the calculation of $T^9 H_\mu^9 + T^{10} H_\mu^{10}$ will be done explicitly.

$$T^9 H_\mu^9 + T^{10} H_\mu^{10} = \frac{1}{2}\begin{pmatrix} 0 & 0 & 0 & 1 \\ 0 & 0 & 0 & 0 \\ 0 & 0 & 0 & 0 \\ 1 & 0 & 0 & 0 \end{pmatrix}\frac{1}{\sqrt{2}}\left(U_\mu^1 + U_\mu^{1*}\right) + \frac{1}{2}\begin{pmatrix} 0 & 0 & 0 & -i \\ 0 & 0 & 0 & 0 \\ 0 & 0 & 0 & 0 \\ i & 0 & 0 & 0 \end{pmatrix}\frac{i}{\sqrt{2}}\left(U_\mu^1 - U_\mu^{1*}\right),$$
$$= \frac{1}{2\sqrt{2}}\begin{pmatrix} 0 & 0 & 0 & U_\mu^1 + U_\mu^{1*} + U_\mu^1 - U_\mu^{1*} \\ 0 & 0 & 0 & 0 \\ 0 & 0 & 0 & 0 \\ U_\mu^1 + U_\mu^{1*} - U_\mu^1 + U_\mu^{1*} & 0 & 0 & 0 \end{pmatrix},$$
$$= \frac{1}{\sqrt{2}}\begin{pmatrix} 0 & 0 & 0 & U_\mu^1 \\ 0 & 0 & 0 & 0 \\ 0 & 0 & 0 & 0 \\ U_\mu^{1*} & 0 & 0 & 0 \end{pmatrix}. \tag{2.64}$$

Similarly one finds for $T^{11} H_\mu^{11} + T^{12} H_\mu^{12}$ and $T^{13} H_\mu^{13} + T^{14} H_\mu^{14}$:

$$T^{11} H_\mu^{11} + T^{12} H_\mu^{12} = \frac{1}{\sqrt{2}}\begin{pmatrix} 0 & 0 & 0 & 0 \\ 0 & 0 & 0 & U_\mu^2 \\ 0 & 0 & 0 & 0 \\ 0 & U_\mu^{2*} & 0 & 0 \end{pmatrix}, \tag{2.65}$$

$$T^{13} H_\mu^{13} + T^{14} H_\mu^{14} = \frac{1}{\sqrt{2}}\begin{pmatrix} 0 & 0 & 0 & 0 \\ 0 & 0 & 0 & 0 \\ 0 & 0 & 0 & U_\mu^3 \\ 0 & 0 & U_\mu^{3*} & 0 \end{pmatrix}. \tag{2.66}$$

Now the contribution of $T^{15} H^{15}$ has to be determined. Luckily this can be done in one line:

$$T^{15} H^{15} = \frac{1}{2\sqrt{6}}\frac{g_Y}{g_1}\begin{pmatrix} Z'_\mu & 0 & 0 & 0 \\ 0 & Z'_\mu & 0 & 0 \\ 0 & 0 & Z'_\mu & 0 \\ 0 & 0 & 0 & -3Z'_\mu \end{pmatrix}. \tag{2.67}$$

Thus one finds for the Dirac Lagrangian of Ψ_L:

$$
\begin{aligned}
\mathcal{L}_{dirac} =& \bar{\Psi}_L (i\gamma^\mu D_\mu) \Psi_L, \\
=& \frac{g_4}{\sqrt{2}} \left(\bar{Q}'_L, \bar{L}'_L \right) \begin{pmatrix} 0 & 0 & 0 & U^1_\mu \\ 0 & 0 & 0 & U^2_\mu \\ 0 & 0 & 0 & U^3_\mu \\ U^{1*}_\mu & U^{2*}_\mu & U^{3*}_\mu & 0 \end{pmatrix} \gamma^\mu \begin{pmatrix} Q'_L \\ L'_L \end{pmatrix} \\
& + \frac{g_4 g_Y}{g_1} \frac{1}{2\sqrt{6}} \left(\bar{Q}'_L, \bar{L}'_L \right) \begin{pmatrix} Z'_\mu & 0 & 0 & 0 \\ 0 & Z'_\mu & 0 & 0 \\ 0 & 0 & Z'_\mu & 0 \\ 0 & 0 & 0 & -3Z'_\mu \end{pmatrix} \gamma^\mu \begin{pmatrix} Q'_L \\ L'_L \end{pmatrix} \\
& + \frac{g_4 g_s}{g_3} \bar{Q}'_L \gamma^\mu T^a Q'_L g'^a_\mu, \\
=& \frac{g_4}{\sqrt{2}} \left(\bar{Q}'_L, \bar{L}'_L \right) \begin{pmatrix} 0 & U_\mu \\ U^\dagger_\mu & 0 \end{pmatrix} \gamma^\mu \begin{pmatrix} Q'_L \\ L'_L \end{pmatrix} + \frac{g_4 g_Y}{g_1} \frac{1}{2\sqrt{6}} \bar{Q}'_L \gamma^\mu Q'_L Z'_\mu - \frac{g_4 g_Y}{g_1} \frac{3}{2\sqrt{6}} \bar{L}'_L \gamma^\mu L'_L Z'_\mu \\
& + \frac{g_4 g_s}{g_3} \bar{Q}'_L \gamma^\mu T^a Q'_L g'^a_\mu, \\
=& \frac{g_4}{\sqrt{2}} \bar{Q}'_L \gamma^\mu L'_L U_\mu + \text{h.c.} + \frac{g_4 g_Y}{g_1} \frac{1}{2\sqrt{6}} \bar{Q}'_L \gamma^\mu Q'_L Z'_\mu - \frac{g_4 g_Y}{g_1} \frac{3}{2\sqrt{6}} \bar{L}'_L \gamma^\mu L'_L Z'_\mu \\
& + \frac{g_4 g_s}{g_3} \bar{Q}'_L \gamma^\mu T^a Q'_L g'^a_\mu.
\end{aligned}
\tag{2.68}
$$

The next left-handed fermion of which the Dirac Lagrangian will be evaluated is q'_L. Since q'_L transforms trivially under $SU(4)$ this calculation will be significantly shorter. Using the quantum number from Table 2.1 one finds for the covariant derivative, omitting all non-relevant parts:

$$
\begin{aligned}
\mathcal{L}_{dirac} &\subset i\bar{q}'_L \gamma^\mu \left(-ig_3 T^a G'^a_\mu - \frac{ig_1}{6} B'_\mu \right) q'_L, \\
&\subset -\frac{g_3 g_s}{g_4} \bar{q}'_L \gamma^\mu T^a q'_L g'^a_\mu + \sqrt{\frac{2}{3}} \frac{1}{6} \frac{g_1 g_Y}{g_4} \bar{q}'_L \gamma^\mu q'_L Z'_\mu.
\end{aligned}
\tag{2.69}
$$

The only left-handed fermion left is ℓ'_L:

$$
\begin{aligned}
\mathcal{L}_{dirac} &\subset i\bar{\ell}'_L \gamma^\mu \left(\frac{ig_1}{2} B'_\mu \right) \ell'_L, \\
&= +\sqrt{\frac{2}{3}} \frac{1}{2} \frac{g_1 g_Y}{g_4} \bar{\ell}'_L \gamma^\mu \ell'_L Z'_\mu.
\end{aligned}
\tag{2.70}
$$

Putting all parts together gives us the full left-handed interaction Lagrangian:

$$\begin{aligned}
\mathcal{L}_L \subset &\frac{g_4}{\sqrt{2}}\bar{Q}'_L\gamma^\mu L'_L U_\mu + \text{h.c.} \\
&+ g_s\left(\frac{g_4}{g_3}\bar{Q}'_L\gamma^\mu T^a Q'_L - \frac{g_3}{g_4}\bar{q}'_L\gamma^\mu T^a q'_L\right)g'^a_\mu \\
&+ g_Y\left(\frac{g_4}{g_1}\frac{1}{2\sqrt{6}}\bar{Q}'_L\gamma^\mu Q'_L + \sqrt{\frac{2}{3}}\frac{1}{6}\frac{g_1}{g_4}\bar{q}'_L\gamma^\mu q'_L\right)Z'_\mu \\
&- g_Y\left(\frac{g_4}{g_1}\frac{3}{2\sqrt{6}}\bar{L}'_L\gamma^\mu L'_L - \sqrt{\frac{1}{6}}\frac{g_1}{g_4}\bar{\ell}'_L\gamma^\mu \ell'_L\right)Z'_\mu.
\end{aligned}$$

(2.71)

Right-handed interaction Lagrangian

The procedure to find the right-handed interaction Lagrangian is completely analogous as for the left-handed interaction Lagrangian. Since the Ψ_L and Ψ_R have the same charges under the gauge groups they also have an identical contribution to the Lagrangian. Therefore one can immediately write down their contribution:

$$\begin{aligned}
\mathcal{L}_{dirac} \subset &\frac{g_4}{\sqrt{2}}\bar{Q}'_R\gamma^\mu L'_R U_\mu + \text{h.c.} + \frac{g_4 g_Y}{g_1}\frac{1}{2\sqrt{6}}\bar{Q}'_R\gamma^\mu Q'_R Z'_\mu - \frac{g_4 g_Y}{g_1}\frac{3}{2\sqrt{6}}\bar{L}'_R\gamma^\mu L'_R Z'_\mu \\
&+ \frac{g_4 g_s}{g_3}\bar{Q}'_R\gamma^\mu T^a Q'_R g'^a_\mu.
\end{aligned}$$

(2.72)

Similarly the contribution of e'_R is the same as the contribution of ℓ'_L up to a factor 2:

$$\mathcal{L}_{dirac} \subset + \sqrt{\frac{2}{3}}\frac{g_1 g_Y}{g_4}\bar{e}'_R\gamma^\mu e'_R Z'_\mu.$$

(2.73)

All that is left is to determine the contribution from u'_R and d'_R. If one takes a look at their charges in Table 2.1 one can see that their charge under $SU(3)'$ is the same as for q'_L and their charge under $U(1)'$ differs only a factor 4 and -2 for u'_R and d'_R respectively. Taking this into account their contributions can be written down using the results from the left-handed interaction Lagrangian:

$$\begin{aligned}
\mathcal{L}_{dirac} \subset &\, i\bar{u}'_R\gamma^\mu\left(-ig_3 T^a G'^a_\mu - \frac{i4g_1}{6}B'_\mu\right)u'_R + i\bar{d}'_R\gamma^\mu\left(-ig_3 T^a G'^a_\mu + \frac{i2g_1}{6}B'_\mu\right)d'_R, \\
\subset &-\frac{g_3 g_s}{g_4}\bar{u}'_R\gamma^\mu T^a u'_R g'^a_\mu + \sqrt{\frac{2}{3}}\frac{2}{3}\frac{g_1 g_Y}{g_4}\bar{u}'_R\gamma^\mu u'_R Z'_\mu \\
&-\frac{g_3 g_s}{g_4}\bar{d}'_R\gamma^\mu T^a d'_R g'^a_\mu - \sqrt{\frac{2}{3}}\frac{1}{3}\frac{g_1 g_Y}{g_4}\bar{d}'_R\gamma^\mu d'_R Z'_\mu.
\end{aligned}$$

(2.74)

Adding all separate contribution one finds for the right-handed interaction Lagrangian:

$$\begin{aligned}
\mathcal{L}_R \subset\ & \frac{g_4}{\sqrt{2}} \bar{Q}'_R \gamma^\mu L'_R U_\mu + \text{h.c.} \\
& + g_s \left(\frac{g_4}{g_3} \bar{Q}'_R \gamma^\mu T^a Q'_R - \frac{g_3}{g_4} \bar{u}'_R \gamma^\mu T^a u'_R - \frac{g_3}{g_4} \bar{d}'_R \gamma^\mu T^a d'_R \right) g'^a_\mu \\
& + g_Y \left(\frac{g_4}{g_1} \frac{1}{2\sqrt{6}} \bar{Q}'_R \gamma^\mu Q'_R + \sqrt{\frac{2}{3}} \frac{2}{3} \frac{g_1}{g_4} \bar{u}'_R \gamma^\mu u'_R - \sqrt{\frac{2}{3}} \frac{1}{3} \frac{g_1}{g_4} \bar{d}'_R \gamma^\mu d'_R \right) Z'_\mu \\
& - g_Y \left(\frac{g_4}{g_1} \frac{3}{2\sqrt{6}} \bar{L}'_R \gamma^\mu L'_R - \sqrt{\frac{2}{3}} \frac{g_1}{g_4} \bar{e}'_R \gamma^\mu e'_R \right) Z'_\mu.
\end{aligned} \tag{2.75}$$

With these two interaction Lagrangians a start can be made with studying the expected phenomenology of our model. All new types of interaction between the SM matter particles and the new massive gauge bosons are encompassed in these two Lagrangians. However, before the phenomenology can be considered and the implications of these new interaction on the $B_{(s)} \to \tau\mu$ decay can be understood, the flavour structure of this model must be introduced.

As mentioned at the beginning of this section there was not enough time to work this out in the same level as detail as what has been shown up to here. Therefor the work from previous publications [15, 40] will be followed and presented.

2.3.4 Yukawa Lagrangian and flavour structure

Just as in the SM, where a change of basis in the Yukawa Lagrangian introduces the mixing between quarks in the interaction with W-bosons, mixing between the vector-like and SM-like fermions can be introduced via the Yukawa Lagrangian. The Yukawa Lagrangian for the SM-like fermions and for the mixed terms is given by:

$$\mathcal{L}_{\text{SM-like}} = -\bar{q}'_L Y_d H d'_R - \bar{q}'_L Y_u \tilde{H} u'_R - \bar{\ell}'_L Y_e H e'_R + \text{h.c.}, \tag{2.76}$$

$$\mathcal{L}_{\text{mix}} = -\bar{q}'_L \lambda_q \Omega_3^T \Psi_R - \bar{\ell}'_L \lambda_\ell \Omega_1^T \Psi_R - \bar{\Psi}_L \left(M + \lambda_{15} \Omega_{15} \right) \Psi_R + \text{h.c.}. \tag{2.77}$$

Using the symmetry of the kinetic term of the fermionic fields one has the freedom to choose another basis:

$$\mathcal{L}_{\text{SM-like}} = -\bar{q}'_L \hat{Y}_d d'_R H - \bar{q}'_L V^\dagger \hat{Y}_u u'_R \tilde{H} - \bar{\ell}'_L \hat{Y}_e e'_R H + \text{h.c.}, \tag{2.78}$$

$$\mathcal{L}_{\text{mix}} = -\bar{q}'_L \lambda_q \Psi_R \Omega_3 - \bar{\ell}'_L \lambda_\ell \Psi_R \Omega_1 - \bar{\Psi}_L \left(\hat{M} + \lambda_{15} \Omega_{15} \right) \Psi_R + \text{h.c.}. \tag{2.79}$$

where λ_q, λ_ℓ and λ_{15} are flavour matrices. If these flavour matrices would be kept general this would allow for very large flavour violating effects for both quarks and gluons. However, if the correct assumptions are made on the flavour structure this model could account for the flavour anomalies without violating constraints from other measurements. The flavour structure that will be used in our model is:

$$\lambda_q = \hat{\lambda}_q \equiv \mathrm{diag}(\lambda_{12}^q, \lambda_{12}^q \lambda_3^q), \tag{2.80}$$

$$\lambda_\ell = \hat{\lambda}_\ell W^\dagger \equiv \mathrm{diag}(\lambda_1^\ell, \lambda_2^\ell \lambda_3^\ell) \begin{pmatrix} 1 & 0 & 0 \\ 0 & \cos\theta_{LQ} & -\sin\theta_{LQ} \\ 0 & \sin\theta_{LQ} & \cos\theta_{LQ} \end{pmatrix}, \tag{2.81}$$

$$\lambda_{15} \propto \hat{M} \propto \mathbb{1}. \tag{2.82}$$

This specific flavour structure allows for a mixing between the second and third generation of quarks and leptons while preventing flavour violating processes in the first generation. If this flavour structure is applied to the interaction Lagrangian of our model the interaction structure of the leptoquark with the quarks and leptons can be found. For the left-handed interactions, Eq. 2.71, the interaction is:

$$\mathcal{L}_{\text{LQ-interaction}} = \frac{g_4}{\sqrt{2}} \bar{Q}_L \gamma^\mu L_L \begin{pmatrix} 1 & 0 & 0 \\ 0 & \cos\theta_{LQ} & -\sin\theta_{LQ} \\ 0 & \sin\theta_{LQ} & \cos\theta_{LQ} \end{pmatrix} U_\mu + \text{h.c.}, \tag{2.83}$$

where the basis $\Psi_L = (Q_L', L_L')^T = (Q_L, WL_L)^T$ is chosen. The SSB structure rotates parts of the SM fermion doublets into Ψ_L. Therefor a projection of Q_L and L_L on the SM-fermion mass eigenstates has to be made. Once these last steps in the calculation are performed the structure of the interaction of U_μ with the SM fermions is given by:

$$\mathcal{L}_{\text{LQ-interaction}} = \frac{g_4}{\sqrt{2}} U_\mu \left[\beta_{ij} \bar{q}_L^i \gamma^\mu \ell_L^j + \text{h.c.} \right], \tag{2.84}$$

where β_{ij} is the 3×3 matrix containing the information of the flavour structure. The final flavour structure is:

$$\beta = \begin{pmatrix} 0 & 0 & 0 \\ 0 & \cos\theta_{LQ} s_{q_{12}} s_{\ell_2} & -\sin\theta_{LQ} s_{q_{12}} s_{\ell_3} \\ 0 & \sin\theta_{LQ} s_{q_3} s_{\ell_2} & \cos\theta_{LQ} s_{q_3} s_{\ell_3} \end{pmatrix}. \tag{2.85}$$

The SM fermion mixing angles can all be expressed in terms of fundamental parameters of the Yukawa Lagrangian. These definitions, together with more details on this calculation, can be found in the appendices of [40]. Now all ingredients are in place to take a look at the low energy phenomenology of this gauge leptoquark.

2.3.5   LQ contributions to the flavour anomalies and $B_{(s)} \to \tau\mu$

Due to the specific flavour structure assumed this model allows for a flavour violating leptoquark interaction in semi-leptonic decays with the second and third generation fermions. This is a necessity to be able to explain the flavour anomalies. In this model U_μ contributes at tree level to $R_{D^{(*)}}$, $R_{K^{(*)}}$ and to $B_{(s)} \to \tau\mu$. Defining the deviation from the SM for $R_{D^{(*)}}$ and $R_{K^{(*)}}$ as:

$$\Delta R_X = \frac{R_X}{R_{X,SM}} - 1, \tag{2.86}$$

one can find $R_{D^{(*)}}$ and $R_{K^{(*)}}$ as well as $\mathcal{B}(B_s \to \tau\mu)$ in terms of the model parameters. Since all three observables have similar transitions one can even write $\mathcal{B}(B_s \to \tau\mu)$ in terms of $\Delta R_{D^{(*)}}$ and $\Delta R_{K^{(*)}}$. Performing this calculation gives an estimate of $\mathcal{B}(B_s \to \tau\mu)$:

$$\mathcal{B}\left(B_{(s)} \to \tau\mu\right) \approx 2.0 \times 10^{-6} \left(\frac{\Delta R_{K^{(*)}}}{0.3}\right)\left(\frac{\Delta R_{D^{(*)}}}{0.2}\right). \tag{2.87}$$

This allows us to make a (very rough) prediction of the branching fraction using the current flavour anomalies. Using the current experimental data available for $R_{D^{(*)}}$[10] and $R_{K^{(*)}}$[9] one finds $\Delta R_{D^{(*)}} = 0.217 \pm 0.053$ and $\Delta R_{K^{(*)}} = 0.154 \pm 0.05$. Therefore, within this model, a prediction for the branching fraction is found of $\mathcal{B} \approx (1.1 \pm 0.09) \times 10^{-6}$.

2.4 Discussion

In this chapter we have seen, after an introduction into some NP particles, how a model can be constructed in such a way that a gauge leptoquark solution is found for the flavour anomalies. Based on this model a prediction was made on the branching fraction of the $B_{(s)} \to \tau\mu$ decay. It is important to keep in mind that one can construct many more solutions to the flavour anomalies that sometimes do and sometimes do not give a sizeable contribution to the $B_{(s)} \to \tau\mu$ decay. In addition, to arrive at the model at hand with the required flavour structure a great number of assumptions had to be made. Nevertheless it is instructive to see how such a model is built and how predictions can be made based on it.
If at some point the $B_{(s)} \to \tau\mu$ decay is found in experiment and a branching fraction can be determined this will not be direct evidence for one model or another, since multiple models can give similar predictions. However, some models can be ruled out since their predicted branching fraction is higher or lower than the measured branching fraction or higher than the limit set on the branching fraction. Therefore experimental searches for these decays are interesting from a theoretical point of view even if only the upper limit can be tightened.

Chapter 3

Studying a minimal explanation

As was discussed in the previous chapter there are many possible extensions to the SM and some of these extensions could account for the flavour anomalies. In this chapter a certain extension of the SM will be studied. The model that will be studied is a minimal explanation for the flavour anomalies, i.e. it is the most basic addition to the SM that can account for the anomalies while also being consistent with other measurements that are in agreement with the SM. This minimal new physics model consists of two scalar particles: a scalar leptoquark and a charged singlet. This chapter aims to recreate the work done in [16]. Unlike the previous chapter no high-energy theory is presented that produces these particles and their specific interactions at low energies. Only the phenomenology of the model is studied.

The goal is to study the parameter space of the coupling constants of these new scalar particles to the SM-particles. It is a priori unknown what the value of these couplings is, they have to be deduced from experimental measurements. At first the methods used to determine the coupling constants will be discussed, followed by a detailed description of the model under consideration. Finally the results of the study will be presented.

3.1 Methods of studying the parameter space

Two types of numerical analyses will be performed to study the parameter space. At first a global likelihood fit, using a χ^2-function, will be performed to find the values of the coupling constants that best account for the anomalies and the SM constraints. Then a numerical scan of the parameter space will be performed using a Markov-Chain Monte Carlo to find the allowed confidence level (CL) regions. However, first the framework has to be constructed before the global likelihood fit and the numerical scan can be performed. This will be covered first.

3.1.1 Building the framework

Building the framework in which the analyses will be performed is conceptually relatively straightforward, but quite challenging if much has to be done from scratch. At first a list of observables must be made, containing both the anomalies and non-anomalous observables to which the model could contribute. Once the list of observables is complete, theoretical

expressions for all the observables have to be found in terms of the parameters of the model. In order to find these expressions a wide range of QFT and EFT calculations have to be performed, which can be quite challenging. Depending on the model these calculations could have been performed already. Next to these theoretical calculations the experimental values and corresponding uncertainties to all the observables have to be found. Once this is all in place a decision must be made on which parameters of the model one wants to study and which ones will be fixed to a certain assumed value, which can be (loosely) based on experimental results or SM predictions.

These analyses cannot be done using merely a pencil and a sheet of paper. For this reason all calculations will be performed using Mathematica[41].

3.1.2 χ^2-fit

Now that the framework has been created the search of the optimal values of the parameters in our model can begin. These values will be found by constructing and minimising a global likelihood function, the χ^2-function:

$$-2\log\mathcal{L} \equiv \chi^2(\lambda_\alpha) = \sum_i \frac{(\mathcal{O}_i(\lambda_\alpha) - \mu_i)^2}{\sigma_i^2}, \tag{3.1}$$

with $\mathcal{O}_i(\lambda_\alpha)$ the expression for the observable in terms of the model parameters λ_α, μ_i the experimentally observed value of the observable and σ_i the uncertainty in the experimental observation.[42]. Theoretical uncertainties are not taken into account explicitly. They can in general be reduced by considering higher order contributions to the observables. Correlations between observables can (and must) be taken into account as well. For two correlated observables their contribution to the χ^2 function is given by:

$$\chi^2(\lambda_\alpha) = \chi_1^2(\lambda_\alpha) + \chi_2^2(\lambda_\alpha) - \frac{2\rho_{12} \cdot (\chi_1^2(\lambda_\alpha))^{\frac{1}{2}}(\chi_2^2(\lambda_\alpha))^{\frac{1}{2}}}{1 - \rho_{12}^2}, \tag{3.2}$$

where ρ_{12} is the Pearson correlation coefficient between the two observables. These correlations are determined in the experimental analyses.

By minimising the χ^2-function for the model parameters the most likely configuration can be found. This minimisation procedure is performed in Mathematica. This best fit χ^2 value can then also be compared to the χ^2 value assuming only SM particles, to see if the model describes the experimental data better than the SM.

3.1.3 Numerical parameter space scan

Besides finding the most likely configuration it is also instructive to consider which values the parameters can take while keeping a certain fit quality. This can be done by considering the confidence level (CL) regions. Specifically the 68% and 95% CL regions will be studied. These CL regions can be coupled to a certain value of $\Delta\chi^2 = \chi^2 - \chi_{min}^2$, where χ_{min}^2 is the best fit value of the χ^2-function. The 68% and 95% CL regions correspond to a $\Delta\chi^2 < 0.98$

and $\Delta\chi^2 < 3.84$ respectively. A numerical scan of parameter space will be performed to see which values of the set of coupling constants fall within these CL regions. For all regions one wants to study a separate scan has to be performed. For models with a large number of parameters these scans can require a lot of computing power. To perform these scans efficiently a Markov-Chain Monte Carlo simulation called the Metropolis-Hastings algorithm is used.

Metropolis-Hastings algorithm

Suppose the model under consideration has 6 parameters and the goal is to scan the parameter space of the model to find our CL regions. If one would consider 12 values for each parameter, $6^{12} \approx 2.2 \cdot 10^9$ points would need to be considered. Besides this the $\Delta\chi^2$ would need to be calculated in each configuration. This is highly inefficient since many configurations would not be inside the desired confidence level regions and it would take a huge amount of time to perform the analysis in this manner. The Metropolis-Hastings algorithm is an algorithm that can generates points in phase space according to the probability distribution governing the system[17]. In this case that would be the $\Delta\chi^2$ function. In this way one can probe the most likely points in phase space.

First a starting configuration in phase space is chosen. From this configuration a random new configuration is chosen by varying all parameters slightly. For this new configuration the $\Delta\chi^2$ is determined. If the $\Delta\chi^2$ corresponds to the desired CL region the new configuration is accepted and it is used as starting position for the next step.[1] If the new configuration is rejected one stays in the previous configuration and uses this as starting point for the next step. Again a new random shift in parameter space is applied and the new value for $\Delta\chi^2$ is checked. This is then repeated for a number of times until the desired statistics has been reached. In this way one scans mainly the allowed regions of parameter space, which is the region of interest, and this makes it highly efficient.

3.2 The model

The model that will be considered is the SM with the addition of a scalar leptoquark S_1 and a charged scalar ϕ^+. Their charges under the SM gauge group[2] are $(\bar{\mathbf{3}}, \mathbf{1}, \frac{1}{3})$ and $(\mathbf{1}, \mathbf{1}, 1)$ for S_1 and ϕ^+ respectively. From their charges under the SM gauge group the interaction Lagrangian can be built. This interaction Lagrangian of S_1 and ϕ^+ with the SM particles is given by

$$\mathcal{L}_{S1+\phi} = \frac{1}{2}\lambda_{\alpha\beta}\bar{\ell}^c_\alpha \epsilon \ell_\beta \phi^+ + \lambda^{1L}_{i\alpha}\bar{q}^c_i \epsilon \ell_\alpha S_1 + \lambda^{1R}_{i\alpha}\bar{u}^c_i e_\alpha S_1 + \text{ h.c. },\tag{3.3}$$

with $\epsilon = i\sigma_2$. As can be seen from the Lagrangian there are two types of LQ couplings. One of them is a coupling between the LQ, up-type quarks and electrons, muons or taus. The

---

[1] The probability distribution governing the system is a χ^2-distribution with one degree of freedom. However, since we are only interested in the boundaries of our CL regions and not in the probability distribution within our CL regions, the configuration is always accepted provided it is within the set boundaries. This is a simplification made to speed up the numerical analysis.

[2] Remember that the charges under the SM gauge group are given by $(SU(3)_c, SU(2)_L, U(1)_Y)$.

other one is a coupling between the LQ, down-type quarks and neutrinos. The charged scalar couples to a lepton and a neutrino from a different flavour.

The model under consideration will be a minimal explanation. All couplings not necessary to account for the anomalies will be set to zero. This and other assumptions will be discussed below. Afterwards a list of all observables used in this study will be given, including the precise theoretical expressions.

3.2.1 Assumptions

As a minimal solution is studied all couplings not necessary to account for the set of anomalies will be set to zero. These couplings are $\lambda_{s\mu}^{1L}$ and $\lambda_{t\tau}^{1R}$, as well as all leptoquark couplings to the first generation quarks. The ϕ^+ coupling $\lambda_{e\tau}$ is set to zero as well because of the tight constraints on the LFV $\mu \to e\gamma$ decay[43].

In order to simplify the model the masses of S_1 and ϕ^+, M_1 and M_ϕ, are both set to 5.5 TeV. A mass of 5.5 TeV is above the detection limit for direct LQ searches at the LHC. In addition, the assumption is made that all the new physics couplings are real.

3.2.2 List of observables

In this study a combination of anomalous observables, such as R_D and $(g-2)_\mu$, and strong phenomenological constraints, such as $\mathcal{B}(\tau \to \mu\gamma)$, is used. In Table 3.1 the full list of observables with their experimental values is given. A description of each observable and the corresponding theoretical expression, in terms of the model parameters, can be found in this subsection as well. The left-handed couplings of S_1 will use down-type quarks to denote the quark generation while right-handed couplings will us up-type quarks, e.g. $\lambda_{b\tau}^{1L}$ and $\lambda_{c\tau}^{1R}$. Besides the masses M_1 and M_ϕ let us define $m_1 = M_1/\text{TeV}$ and $m_\phi = M_\phi/\text{TeV}$.

CKM matrix

In numerous expressions elements of the CKM matrix are needed. Therefore the CKM matrix in the Wolfenstein parametrisation up to $\mathcal{O}(\lambda^6)$ is presented first[50]:

$$V_{CKM} = \begin{pmatrix} V_{ud} & V_{us} & V_{ub} \\ V_{cd} & V_{cs} & V_{cb} \\ V_{td} & V_{ts} & V_{tb} \end{pmatrix}, \tag{3.4}$$

$$= \begin{pmatrix} -\frac{\lambda^4}{8} - \frac{\lambda^2}{2} + 1 & \lambda & A\lambda^3(\rho - i\eta) \\ -\lambda\left(iA^2\eta\lambda^4 - A^2\lambda^4\left(\frac{1}{2} - \rho\right) + 1\right) & -\frac{1}{8}\left(4A^2 + 1\right)\lambda^4 - \frac{\lambda^2}{2} + 1 & A\lambda^2 \\ A\lambda^3\left(-i\eta\left(1 - \frac{\lambda^2}{2}\right) + \frac{\lambda^2\rho}{2} - \rho + 1\right) & -A\lambda^2\left(i\eta\lambda^2 - \lambda^2\left(\frac{1}{2} - \rho\right) + 1\right) & 1 - \frac{A^2\lambda^4}{2} \end{pmatrix}.$$

The values used for the CKM-parameters are $A = 0.79$, $\lambda = 0.2265$, $\rho = 0.144712$ and $\eta = 0.366399$[45].

Table 3.1: The observables with their experimental values used in the analysis. In case of a limit on a certain observable, e.g. $\mathcal{B}(\tau \to \mu\gamma)$, the 68% CL region is taken.

Observable	Experimental Value
R_D	0.34 ± 0.029 [10]
R_{D^*}	0.295 ± 0.013 [10]
Δa_μ	$(2.51 \pm 0.59) * 10^{-9}$ [6, 7]
ΔC_9	-0.675 ± 0.16 [16]
ΔC_{10}	0.244 ± 0.13 [16]
$R_D^{\mu/e}$	0.978 ± 0.035 [44]
$\delta(\mu \to e\nu\nu)$	$(6.5 \pm 1.5) * 10^{-4}$ [43]
$\mathcal{B}(\tau \to \mu\gamma)$	$< 2.66 * 10^{-8}$ [45]
g_τ/g_e	1.0058 ± 0.003 [10]
g_τ/g_μ	1.0022 ± 0.003 [10]
g_μ/g_e	1.0036 ± 0.0028 [10]
$C_{B_s}^1$	$< 1.02 * 10^{-5} \, \mathrm{TeV}^{-2}$ [46]
$\delta g_{\tau_L}^Z$	$(-0.11 \pm 0.61) * 10^{-3}$ [47]
$\delta g_{\tau_R}^Z$	$(0.66 \pm 0.65) * 10^{-3}$ [47]
$\delta g_{\mu_L}^Z$	$(0.3 \pm 1.1) * 10^{-3}$ [47]
$\delta g_{\mu_R}^Z$	$(0.2 \pm 1.3) * 10^{-3}$ [47]
R_K^ν	< 1.63 [48]
$\mathcal{B}\left(B_c^+ \to \tau^+\nu\right)$	< 0.1 [49]
$|\mathrm{Re}(C_D^1)|$	$< 1.81 * 10^{-7} \, \mathrm{TeV}^{-2}$ [46]
$|\mathrm{Im}(C_D^1)|$	$< 1.13 * 10^{-8} \, \mathrm{TeV}^{-2}$ [46]

$b \to cl\nu$ transitions

As covered in Section 1.3 the LFU ratios R_D and R_{D^*} both deviate from their SM prediction. The scalar leptoquark S_1 can contribute at tree level to the $b \to c\tau\nu$ transitions. The Feynman diagram of its contribution at leading order can be found in Fig. 3.1 The numerical expressions for R_D and R_{D^*}, with the S_1 contribution, are given by[42]:

$$
\begin{aligned}
\frac{R(D)}{R(D)_{SM}} &= 1 + 2\,\mathrm{Re}\left[C_{V_L}\right] - 0.79\frac{\lambda_{b\tau}^{1L}\lambda_{c\tau}^{1R}}{m_1^2}\left(1 + 0.05\log m_1^2\right) \\
&+ 0.36\frac{\left(\lambda_{b\tau}^{1L}\lambda_{c\tau}^{1R}\right)^2}{m_1^4}\left(1 + 0.08\log m_1^2\right),
\end{aligned}
\tag{3.5}
$$

$$
\begin{aligned}
\frac{R(D^*)}{R(D^*)_{SM}} &= 1 + 2\,\mathrm{Re}\left[C_{V_L}\right] - 0.34\frac{\lambda_{b\tau}^{1L}\lambda_{c\tau}^{1R}}{m_1^2}\left(1 + 0.02\log m_1^2\right) \\
&+ 0.1\frac{\left(\lambda_{b\tau}^{1L}\lambda_{c\tau}^{1R}\right)^2}{m_1^4}\left(1 + 0.01\log m_1^2\right).
\end{aligned}
\tag{3.6}
$$

In these expressions the renormalization group evolution (RGE) from UV matching scale to the electroweak scale is taken into account. The SM values of R_D and R_{D^*} are 0.299 and 0.258
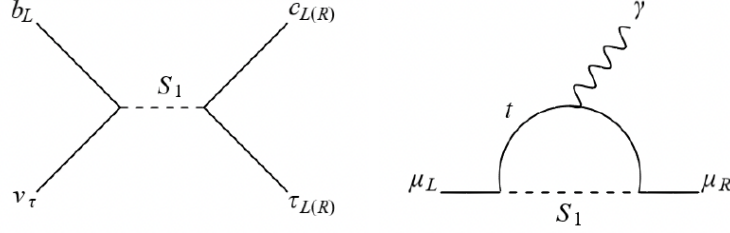
Figure 3.1: The leading order contributions of the scalar LQ S_1 to $R_{D^{(*)}}$ on the left and $(g-2)_\mu$ on the right. Figure adapted from [16].

respectively[10]. The observables R_D and R_{D^*} are correlated, which is taken into account when constructing our χ^2-function. The way to account for correlations has been discussed in section 3.1. The Pearson correlation coefficient between R_D and R_{D^*} is $\rho = -0.38$[10]. Another observable that is sensitive to $b \to c\tau\nu$ transitions is the branching ratio $\mathcal{B}\left(B_c^+ \to \tau^+\nu\right)$[42]:

$$
\begin{aligned}
\frac{\text{Br}\left(B_c^+ \to \tau^+\nu\right)}{\text{Br}\left(B_c^+ \to \tau^+\nu\right)_{\text{SM}}} &= 1 + 2\,\text{Re}\left[C_{V_L}\right] + 5.1\frac{\lambda_{b\tau}^{1L}\lambda_{c\tau}^{1R}}{m_1^2}\left(1 + 0.04\log m_1^2\right) \\
&+ 6.5\frac{\left(\lambda_{b\tau}^{1L}\lambda_{c\tau}^{1R}\right)^2}{m_1^4}\left(1 + 0.08\log m_1^2\right).
\end{aligned}
\tag{3.7}
$$

The term $2C_{V_L}$ in R_D, R_{D^*} and $\mathcal{B}\left(B_c^+ \to \tau^+\nu\right)$ is given by:

$$
2C_{V_L} = \frac{0.77}{V_{cs}m_1^2}\left(\lambda_{b\tau}^{1L}V_{cs}\lambda_{s\tau}^{1L*} + \lambda_{b\tau}^{1L}V_{cb}\lambda_{b\tau}^{1L*}\right).
\tag{3.8}
$$

The SM value for $\mathcal{B}\left(B_c^+ \to \tau^+\nu\right) \approx 2\%$[49].

There are constraints on LFU in $b \to cl\nu$ processes containing electrons and muons. One of these constraints is the ratio $R_D^{\mu/e} \equiv \mathcal{B}(B \to D\mu\nu)/\mathcal{B}(B \to De\nu)$. The NP contribution to this ratio is[42]:

$$
R_D^{\mu/e} \equiv \frac{\text{Br}\left(B \to D\mu\nu\right)}{\text{Br}\left(B \to De\nu\right)} = 1 + 2\,\text{Re}\left[C_{V_L}^\mu\right] - 0.047\frac{\lambda_{b\mu}^{1L}\lambda_{c\mu}^{1R}}{m_1^2} + 0.50\frac{\left|\lambda_{b\mu}^{1L}\lambda_{c\mu}^{1R}\right|^2}{m_1^4},
\tag{3.9}
$$

where $\text{Re}\left[C_{V_L}^\mu\right]$ is the same as $\text{Re}\left[C_{V_L}\right]$ in the expressions above.

Anomalous magnetic moment of the muon

One other current anomaly, outside the field of flavour physics, is the measurement of the magnetic moment of the muon. There have been great efforts to measure its value in experiment[6] and to determine its SM prediction[7]. The scalar leptoquark can contribute to this magnetic moment. The leading order contribution is shown in Fig. 3.1. This S_1 contribution to the $(g-2)_\mu$ deviation Δa_μ in terms of the model parameters is[51]:

$$
\Delta a_\mu = \frac{m_\mu m_t \lambda_{b\mu}^{1L}\lambda_{t\mu}^{1R}}{4\pi^2 M_1^2}\left(\log M_1^2/m_t^2 - \frac{7}{4}\right) - \frac{m_\mu^2\left(|\lambda_{b\mu}^{1L}|^2 + |\lambda_{t\mu}^{1R}|^2 + |\lambda_{c\mu}^{1R}|^2\right)}{32\pi^2 M_1^2}.
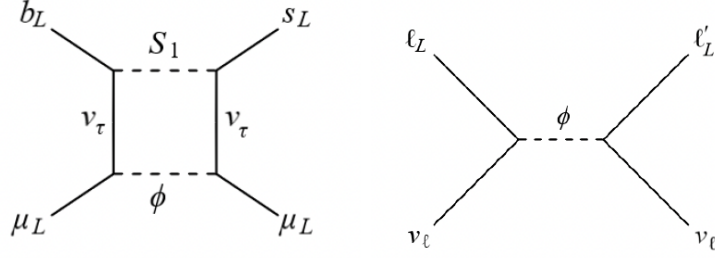\tag{3.10}
$$

Figure 3.2: The leading order contributions of the scalar LQ S_1 and the charged scalar ϕ to $b \to s\ell\ell$ transitions on the left and general charged lepton currents on the right. Figure adapted from [16].

$b \to sll$ transitions

As discussed in Section 1.3, the LFU ratio $R_{K^{(*)}}$ deviates from the expected SM value. These processes can be described using a combined top-down and bottom-up effective field theory approach. The EFT-operator $\mathcal{O}_{LL(LR)}^{bs\mu\mu} = (\bar{s}\gamma^\alpha P_L b)(\bar{\mu}\gamma_\alpha P_{L(R)}\mu)$ can contribute to the $b \to sll$ processes. Both S_1 and ϕ^+ give contributions to the Wilson coefficient of $\mathcal{O}_{LL(LR)}^{bs\mu\mu}$, as can be seen from the Feynman diagram in Fig. 3.2. These Wilson coefficients are given by [51]:

$$C_{LR} = \frac{|\lambda_{c\mu}^{1R}|^2 \, \lambda_{b\tau}^{1L} \, \lambda_{s\tau}^{1L*}}{64\pi^2 \, M_1^2}, \tag{3.11}$$

$$C_{LL} = -\lambda_{b\tau}^{1L}\lambda_{s\tau}^{1L*} \left(\frac{|\lambda_{b\mu}^{1L}|^2}{64\pi^2 \, M_1^2} + \frac{|\lambda_{\mu\tau}|^2 \, \log M_\phi^2/M_1^2}{64\pi^2(M_\phi^2 - M_1^2)} \right). \tag{3.12}$$

The values of these Wilson coefficients are found in global fits, the bottom-down part of this approach, which use the $R_{K^{(*)}}$ anomaly as input among other observables. They are determined in a linear combinations:

$$\Delta C_{9,10} = (C_{LR} \pm C_{LL})/2\mathcal{N}_{sb}. \tag{3.13}$$

The normalisation N_{sb} for C_9 and C_{10} is given by:

$$\mathcal{N}_{sb} = \frac{G_F \, \alpha \, V_{tb}V_{ts}^*}{\sqrt{2}\pi}. \tag{3.14}$$

Charged current lepton decays

The charged scalar ϕ^+ and the leptoquark S_1 can contribute to the charged current decay of leptons at tree level or one-loop level respectively. The leading contribution of ϕ^+ is shown in Fig. 3.2. The total contributions, tree level and one-loop, are given by[16]:

$$\delta(\mu \to e\nu\nu) = \frac{v^2 \left|\lambda_{e\mu}\right|^2}{4M_\phi^2} + \frac{3m_t^2 \left|\lambda_{b\mu}^{1L}\right|^2}{32\pi^2 M_1^2} \left(\frac{1}{2} - \log \frac{M_1^2}{m_t^2}\right),$$

$$\delta(\tau \to \mu\nu\nu) = \frac{v^2 \left|\lambda_{\mu\tau}\right|^2}{4M_\phi^2} + \frac{3v^2 \left|\lambda_{b\mu}^{1L}\right|^2 \left|\lambda_{b\tau}^{1L}\right|^2}{128\pi^2 M_1^2} +$$

$$+ \frac{3m_t^2 \left(\left|\lambda_{b\mu}^{1L}\right|^2 + \left|\lambda_{b\tau}^{1L}\right|^2\right)}{32\pi^2 M_1^2} \left(\frac{1}{2} - \log \frac{M_1^2}{m_t^2}\right),$$

$$\delta(\tau \to e\nu\nu) = \frac{3m_t^2 \left|\lambda_{b\tau}^{1L}\right|^2}{32\pi^2 M_1^2} \left(\frac{1}{2} - \log \frac{M_1^2}{m_t^2}\right).$$

(3.15)

The lepton flavour universality ratios, which have been measured, are defined as[42]:

$$\frac{g_\tau}{g_e} \equiv \frac{\Gamma(\tau \to \mu\nu\bar{\nu})}{\Gamma(\mu \to e\nu\bar{\nu})} \left(\frac{\Gamma_{\mathrm{SM}}(\tau \to \mu\nu\bar{\nu})}{\Gamma_{\mathrm{SM}}(\mu \to e\nu\bar{\nu})}\right)^{-1} = \left|\frac{1 + \delta(\tau \to \mu\nu\nu)}{1 + \delta(\mu \to e\nu\nu)}\right|,$$

$$\frac{g_\mu}{g_e} \equiv \frac{\Gamma(\tau \to \mu\nu\bar{\nu})}{\Gamma(\tau \to e\nu\bar{\nu})} \left(\frac{\Gamma_{\mathrm{SM}}(\tau \to \mu\nu\bar{\nu})}{\Gamma_{\mathrm{SM}}(\tau \to e\nu\bar{\nu})}\right)^{-1} = \left|\frac{1 + \delta(\tau \to \mu\nu\nu)}{1 + \delta(\tau \to e\nu\nu)}\right|,$$

$$\frac{g_\tau}{g_\mu} \equiv \frac{\Gamma(\tau \to e\nu\bar{\nu})}{\Gamma(\mu \to e\nu\bar{\nu})} \left(\frac{\Gamma_{\mathrm{SM}}(\tau \to e\nu\bar{\nu})}{\Gamma_{\mathrm{SM}}(\mu \to e\nu\bar{\nu})}\right)^{-1} = \left|\frac{1 + \delta(\tau \to e\nu\nu)}{1 + \delta(\mu \to e\nu\nu)}\right|.$$

(3.16)

$B \to K^{(*)}\bar{\nu}\nu$ decays

The branching ratio of $B \to K^{(*)}\bar{\nu}\nu$ is a clean observable in the SM. The ratio R_{K^ν}, which is a measure of the NP contribution to this decay, is defined as[42]:

$$R_K^\nu = \frac{\mathcal{B}(B \to K\nu\nu)}{\mathcal{B}(B \to K\nu\nu)_{\mathrm{SM}}},$$

$$= 1 + 1.34\frac{\lambda_{s\tau}^{1L}\lambda_{b\tau}^{1L}}{V_{ts}m_1^2} + 1.42\frac{(\lambda_{s\tau}^{1L})^2((\lambda_{b\mu}^{1L})^2 + (\lambda_{b\tau}^{1L})^2)}{V_{ts}^2 m_1^4}.$$

(3.17)

$\tau \to \mu\gamma$ decays

The branching ratio on the tau decaying to muon via a triangle diagram will give constraints on our S_1 couplings. This decay is forbidden in the SM and has not been observed experimentally. The numerical expression for this branching ratio is[42]:

$$\mathrm{Br}(\tau \to \mu\gamma) \approx \frac{4.9 \times 10^{-8}}{m_1^4}$$

$$\left(\left|1220 \left(V_{tb}^*\lambda_{b\tau}^{1L} + V_{ts}^*\lambda_{s\tau}^{1L}\right)\lambda_{t\mu}^{1R} + 58 \left(V_{cs}^*\lambda_{s\tau}^{1L} + V_{cb}^*\lambda_{b\tau}^{1L}\right)\lambda_{c\mu}^{1R} - 2.6 \left(\lambda_{c\mu}^{1R}\lambda_{c\tau}^{1R}\right)\right|^2\right.$$

$$\left. + \left|58 \left(V_{cb}\lambda_{b\mu}^{1L*}\right)\lambda_{c\tau}^{1R} + 0.88 \left(\lambda_{b\mu}^{1L}\lambda_{b\tau}^{1L}\right)\right|^2\right).$$

(3.18)

Z boson coupling

The S_1 leptoquark can contribute to the Z boson coupling on the one loop level, via a triangle diagram. These modifications are given by[16, 42]:

$$
\begin{aligned}
10^3 \delta g^Z_{e_{\alpha L}} &\approx 0.59 \frac{\left(\lambda^{1L}_{b\alpha}\right)^2}{m_1^2} \left(1 + 0.39 \log m_1^2\right), \\
10^3 \delta g^Z_{e_{\alpha R}} &\approx -0.67 \frac{\left(\lambda^{1R}_{t\alpha}\right)^2}{m_1^2} \left(1 + 0.37 \log m_1^2\right) + 0.059 \frac{\left(\lambda^{1R}_{c\alpha}\right)^2}{m_1^2}.
\end{aligned}
\tag{3.19}
$$

Meson mixing

The S_1 leptoquark gives contributions to B_S and D^0 meson mixing via the operators $\mathcal{O}^1_{B_s} = (\bar{s}\gamma_\mu P_L b)^2$ and $\mathcal{O}^1_D = (\bar{u}\gamma_\mu P_L c)^2$. The Wilson coefficients are[42]:

$$
C^1_{B_s} = \frac{\left(\lambda^{1L*}_{b\tau}\lambda^{1L}_{s\tau}\right)^2}{128\pi^2 M_1^2},
\tag{3.20}
$$

$$
C^1_D = \frac{\left(V_{cb}V^*_{ub}(\lambda^{1L*}_{b\tau}\lambda^{1L}_{b\tau} + \lambda^{1L*}_{b\mu}\lambda^{1L}_{b\mu}) + V_{cb}V^*_{us}\lambda^{1L*}_{b\tau}\lambda^{1L}_{s\tau} + V_{cs}V^*_{ub}\lambda^{1L*}_{s\tau}\lambda^{1L}_{b\tau} + V_{cs}V^*_{us}\lambda^{1L*}_{s\tau}\lambda^{1L}_{s\tau}\right)^2}{128\pi^2 M_1^2}.
\tag{3.21}
$$

3.3 Results

The model described in the previous section was built using Mathematica. First the χ^2-minimisation was performed to find the best-fit values for the coupling constants. Afterwards a numerical analysis of the parameter space was made using a Markov-Chain MC. Both analyses were performed as described in the beginning of this chapter. In this section the results of the analyses will be presented, starting with the χ^2-fit.

3.3.1 χ^2 fit

At first the χ^2-function was evaluated with all couplings set to 0, determining the goodness of fit for the SM. This sets the benchmark for the improvement of the fit when the NP is included. For the SM a value of $\chi^2_{SM} = 78.25$ is found. Minimising the χ^2-function yields $\chi^2_{min} = 9.37$. The values for the coupling constants in this minimum can be found in Table 3.3.1. Adding this NP model leads to an improvement of $\Delta\chi^2 = 68.88$ compared to the SM, which is a considerable improvement.

3.3.2 Scan of parameter space

A numerical scan of the parameter space was performed using Markov-Chain Monte Carlo following the steps set laid out in the beginning of this chapter. The starting point of the

Table 3.2: The values of the coupling constants yielding a minimum of the χ^2-fit

Coupling	Best fit
$\lambda_{b\tau}^{1L}$	-1.72
$\lambda_{s\tau}^{1L}$	0.38
$\lambda_{b\mu}^{1L}$	-1.96
$\lambda_{c\tau}^{1R}$	3.38
$\lambda_{t\mu}^{1R}$	-0.02
$\lambda_{c\mu}^{1R}$	-2.90
$\lambda_{e\mu}$	1.32
$\lambda_{\mu\tau}$	3.64

numerical scan was chosen to be the best fit value of the χ^2-fit. The scan is performed separately for both CL regions. The number of data points gathered is 69000(67000) for the 68%(95%) confidence level region. To visualise the allowed regions in parameter space, two-dimensional projections of the eight-dimensional parameter space were made. Examples of these projections are presented in Figure 3.3 and 3.4. The 68%(95%) confidence level region is shown in green(yellow) while the best fit value is presented as the black dot.

Each observable in the χ^2-fit has its own constraints on the allowed parameter space, some more constraining than others. The tightest individual constraints are shown in the 2D projections of Figure 3.3 and 3.4 as well. To plot these individual constraints the theoretical expression for a certain observable is set equal to its limit. For observables with a central value the 1σ limit for the observable is taken, however if there is only an upper
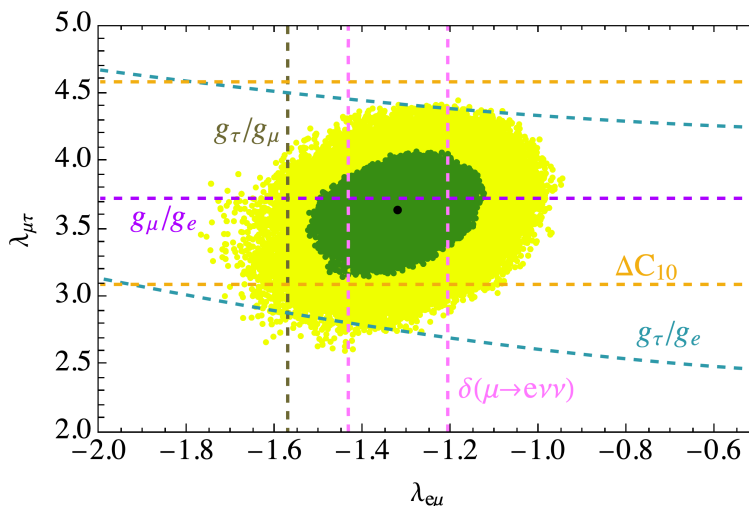

Figure 3.3: The 2D projection of the charged scalar couplings $\lambda_{e\mu}$ and $\lambda_{\mu\tau}$. The best fit value is represented by the black dot. The 68% and 95% CL regions are shown in green and yellow respectively. The most stringent individual constraints on these couplings are drawn in the figure as well.
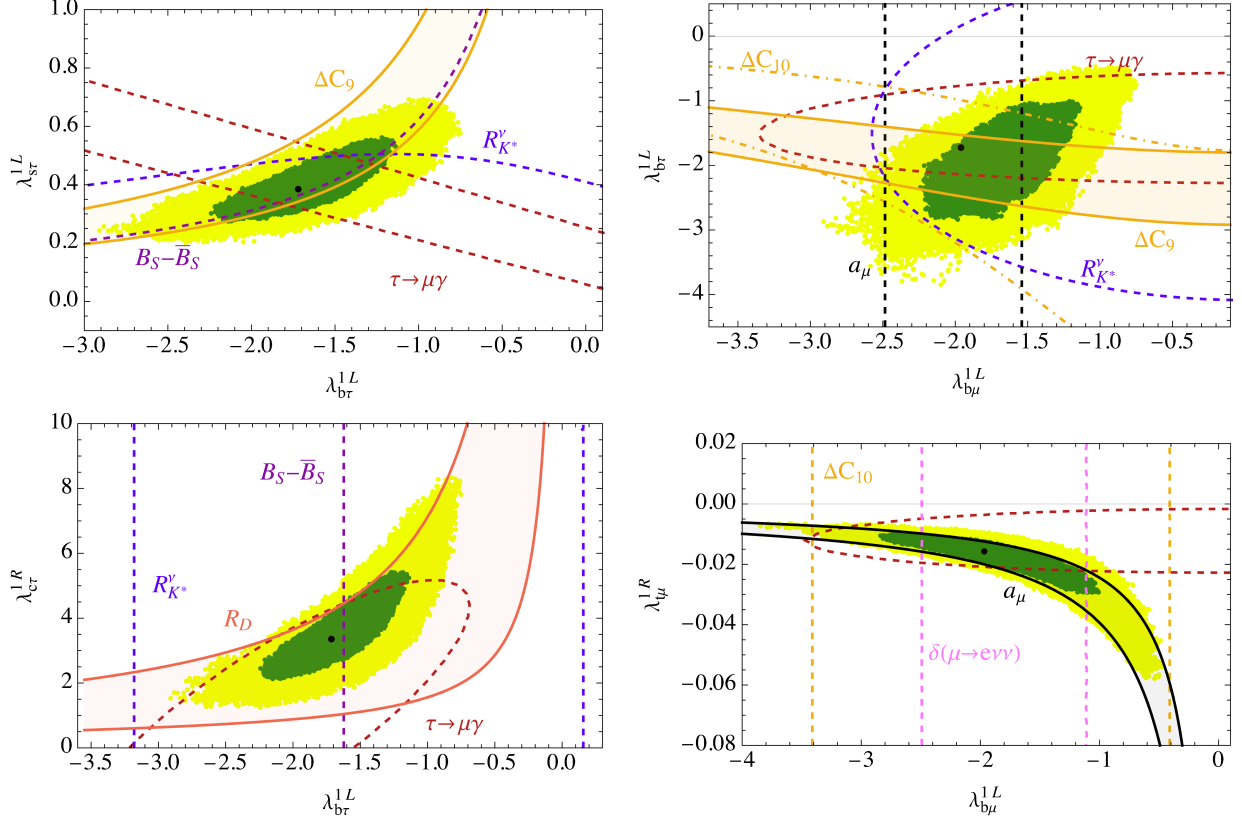
Figure 3.4: The 2D projection of different scalar leptoquark couplings. Like in Figure 3.3, the best fit value is represented by the black dot and the 68% and 95% CL regions are shown in green and yellow respectively. The tightest individual constraints on these couplings are drawn in the figure as well. The 2D projections presented are from left top to right bottom: $\lambda_{b\tau}^{1L}$ versus $\lambda_{s\tau}^{1L}$, $\lambda_{b\mu}^{1L}$ versus $\lambda_{b\tau}^{1L}$, $\lambda_{b\tau}^{1L}$ versus $\lambda_{c\tau}^{1R}$ and $\lambda_{b\mu}^{1L}$ versus $\lambda_{b\mu}^{1R}$.

or lower bound for a certain observable, e.g. $\mathcal{B}\left(B_c^+ \to \tau^+\nu\right)$, the 68% CL region is taken. The contour of this equality is then drawn in the 2D projection. If an observable depends on other couplings than the projected ones, the best fit value of these couplings are used as input.

From both the projection and the individual constraints in Figure 3.3 and the projections in Figure 3.4 it can be seen that the CL regions roughly follow the individual constraints. In some cases one of the individual constraints mainly dominates the shape of the allowed parameter space region. One example is the Δa_μ constraint in the $\lambda_{b\mu}^{1L}$-$\lambda_{t\mu}^{1R}$ projection, as can be seen in the bottom right projection in Figure 3.4. In other projections there is not one constraint dominating the shape, such as in the $\lambda_{e\mu}$-$\lambda_{\mu\tau}$ projection in Figure 3.3.

It is also possible to map the results of the parameter space scan back to the initial observables. This gives insight to whether the allowed parameter space region falls together with the experimental value. This has been done for R_D, R_{D^*}, ΔC_9 and ΔC_{10}, δa_μ and $B(\tau \to \mu\gamma)$ and for g_τ/g_e and $\delta(\mu \to e\nu\nu)$. These results are presented in Fig.3.5 with the experimental value of the observables depicted as the black cross-hair in addition to the best
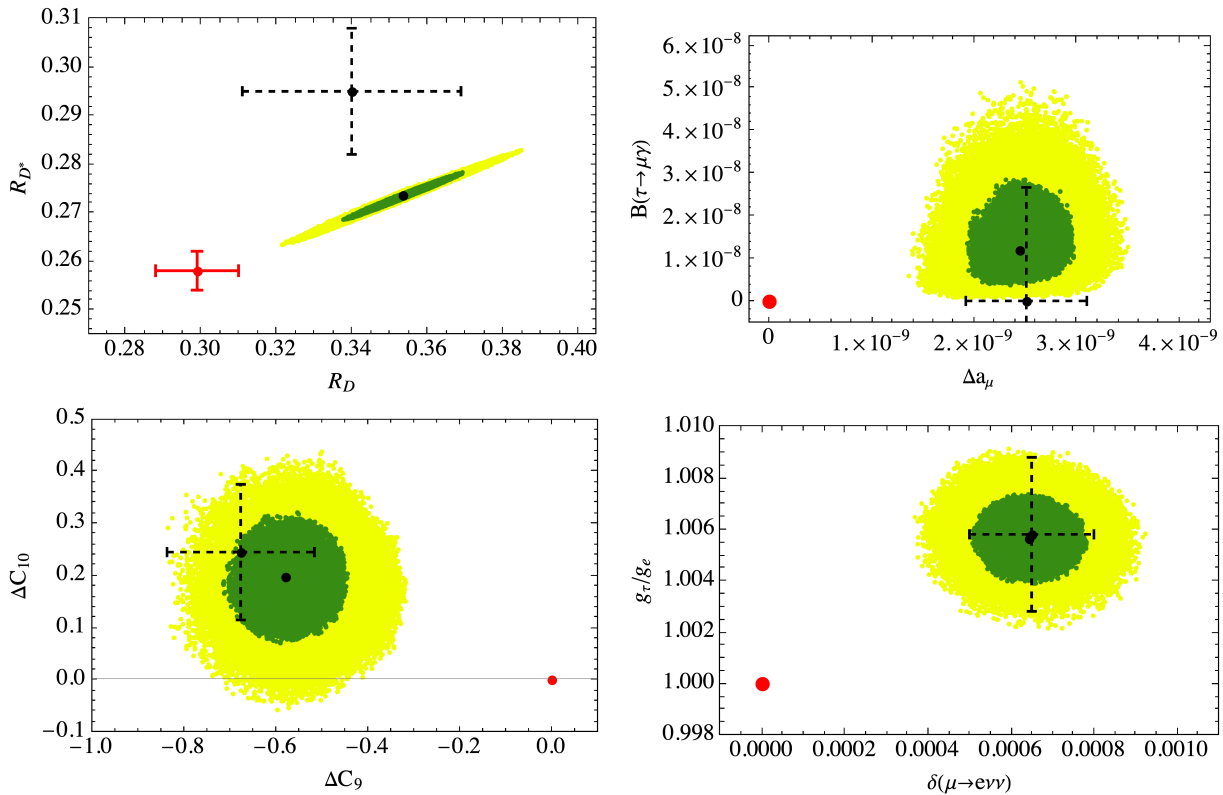
Figure 3.5: The results of the parameter space scan mapped back to the initial observables. Like before the best fit value is represented by the black dot and the 68% and 95% CL regions are shown in green and yellow respectively. In addition the experimental value is presented as the black cross-hair and the SM-value as a red cross-hair or dot. The allowed values for R_D and R_{D^*} (top left), ΔC_9 and ΔC_{10} (bottom left), δa_μ and $B(\tau \to \mu\gamma)$ (top right) and g_{tau}/g_e and $\delta(\mu \to e\nu\nu)$ (bottom right) in the two CL regions.

fit value and the two CL regions. One can see that for R_D and R_{D^*} the allowed CL regions do not overlap with the experimental values in this projection, while ΔC_9 and ΔC_{10} this is the case. In addition to the results of the fit the SM values are also included in the figures. This helps visualising that, although the experimental results cannot perfectly be accounted for in this model, there is an improvement compared to the SM values in many cases.

3.4 Discussion and outlook

The methods used in this chapter can be extended to perform a more elaborate fit. In addition the methods can also be applied to different, more complicated models, without an increase in complexity of the analysis. One obvious extension of the current model is to include the masses of the charged scalar and the scalar leptoquark as a free parameters. In addition more observables could be added to the fit to further constrain the parameters of this minimal model. Experimental results of direct LQ searches could also help, further constraining the parameter space.

Considering another model would, in light of the main topic of the experimental part of this thesis, also be interesting to consider. The minimal explanation considered in this chapter does not give any contributions to $B_{(s)} \to \tau\mu$ at tree level. Other models with for example a vector leptoquark, such as the 4321-model that was explored in the previous chapter, could give contributions at tree level to this process.

Another reason to study more extensive models is that, although there is an extensive improvement with respect to the Standard Model, not all anomalies can be explained within the set confidence levels. One example of this is the value of R_{D^*}, which in our fit results is too low for most values of R_D. However one should be careful, if enough new particles and parameters are added one can always explain everything. Besides this none of the observed anomalies has yet surpassed the necessary 5σ level, so there is always the possibility that they were due to a statistical fluctuation.

Part II

Experimental studies of LFV $B_{(s)} \to \tau\mu$ decays with LHCb

Chapter 4

The LHCb experiment

The LHCb experiment is one of the four major experiments at the Large Hadron Collider (LHC), together with ATLAS, CMS and ALICE. ATLAS and CMS are general-purpose detectors and the ALICE experiment focuses on heavy-ion physics.
In this chapter a brief overview of the LHC accelerator complex will be given, including its past and future operations. Then the LHCb detector will be covered in more detail, shedding some light on its different components as they were during Run 1 (2011-2012) and 2 (2015-2018). Finally an overview of the most important upgrades to the LHCb detector, implemented during the shutdown of 2019-2022, are presented. Another key aspect of the LHCb detector, or any other collider experiment, is the trigger system. The LHCb trigger system decides during data taking which events[1] will be saved. This trigger system and the upgrades to the trigger system will be covered in detail in the next chapter.
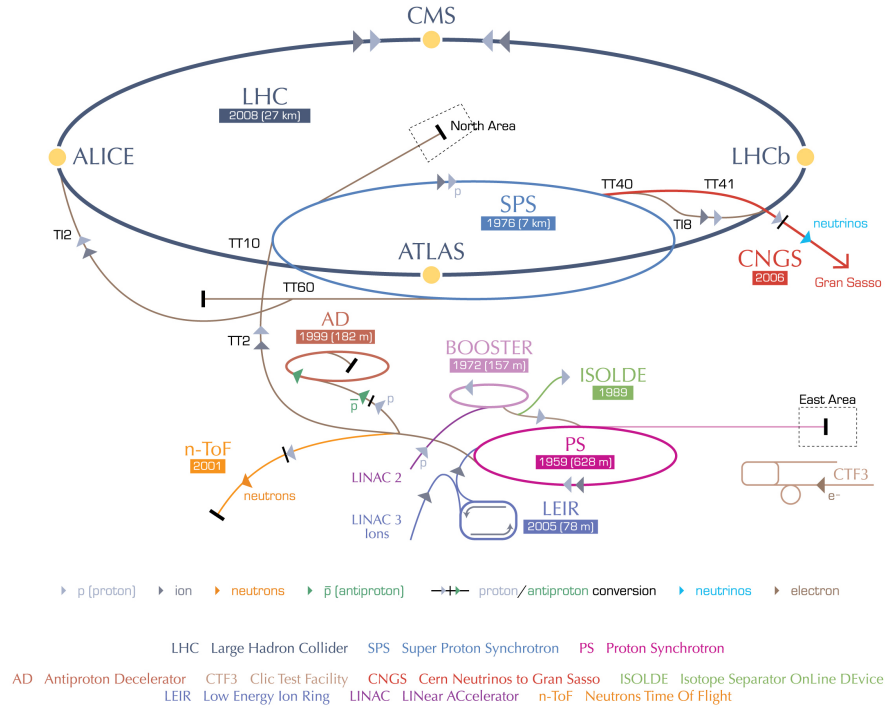
4.1 The LHC at CERN

The LHC[52] is a 27 kilometres long circular particle collider built at CERN, the European Organisation for Nuclear Research. It is designed to accelerate and collide protons, which is its main mode of operation, and heavy-ion nuclei (mainly lead-ions). There is an extensive system of smaller linear and circular accelerators, called the LHC accelerator complex, in which the protons are pre-accelerated before being injected into the LHC ring. In the LHC two beams of protons travel in opposite directions and are brought to collide at 4 different interaction points. These interaction points are where the four main experiments are located. The LHC has had two main periods of operation at increasingly higher energies. In Run 1 protons were collided with a centre of mass energy $\sqrt{s} = 7$ TeV in 2011 and $\sqrt{s} = 8$ TeV in 2012. After a shutdown of three years operations resumed in 2015 for Run 2, when protons were collided at an centre of mass energy of $\sqrt{s} = 13$ TeV up until 2018, reaching a peak luminosity of $\mathcal{L} = 10^{34}\,\mathrm{cm}^{-2}s^{-1}$. In 2022 the LHC is resuming operations, hoping to start the physics runs in 2023.

The four main experiments at the LHC are ATLAS[54], CMS[55], ALICE[56] and LHCb[18]. The ATLAS and CMS detectors are general-purpose detectors, originally designed for the

---

[1]An event is a collision that can be seen by the LHCb detector

Figure 4.1: A schematic view of the accelerator complex at CERN[53].

discovery of the Higgs particle. They are both barrel-shaped detectors built around the interaction point. Their current focus is, among many other topics, studying the properties of the Higgs boson and direct searches for BSM particles. The ALICE experiment focuses on the study of the quark gluon plasma (QGP) in heavy-ion collisions. Just like ATLAS and CMS, it is a barrel-shaped detector built around the interaction point.

The LHCb experiment was built to perform high precision measurements of the decays of b- and c-hadrons. It is specialised in the measurement of rare decays and CP-violation, the asymmetry between matter and anti-matter. In contrast to ATLAS, CMS and ALICE it is not a barrel-shaped detector built around the interaction point. It is a forward-facing detector built at one side of the interaction point.

4.2 LHCb

The LHCb experiment[18], built at point 8 of the LHC, is a forward-facing spectrometer covering a pseudorapidity range of $2 < \eta < 5$, where η is defined as:
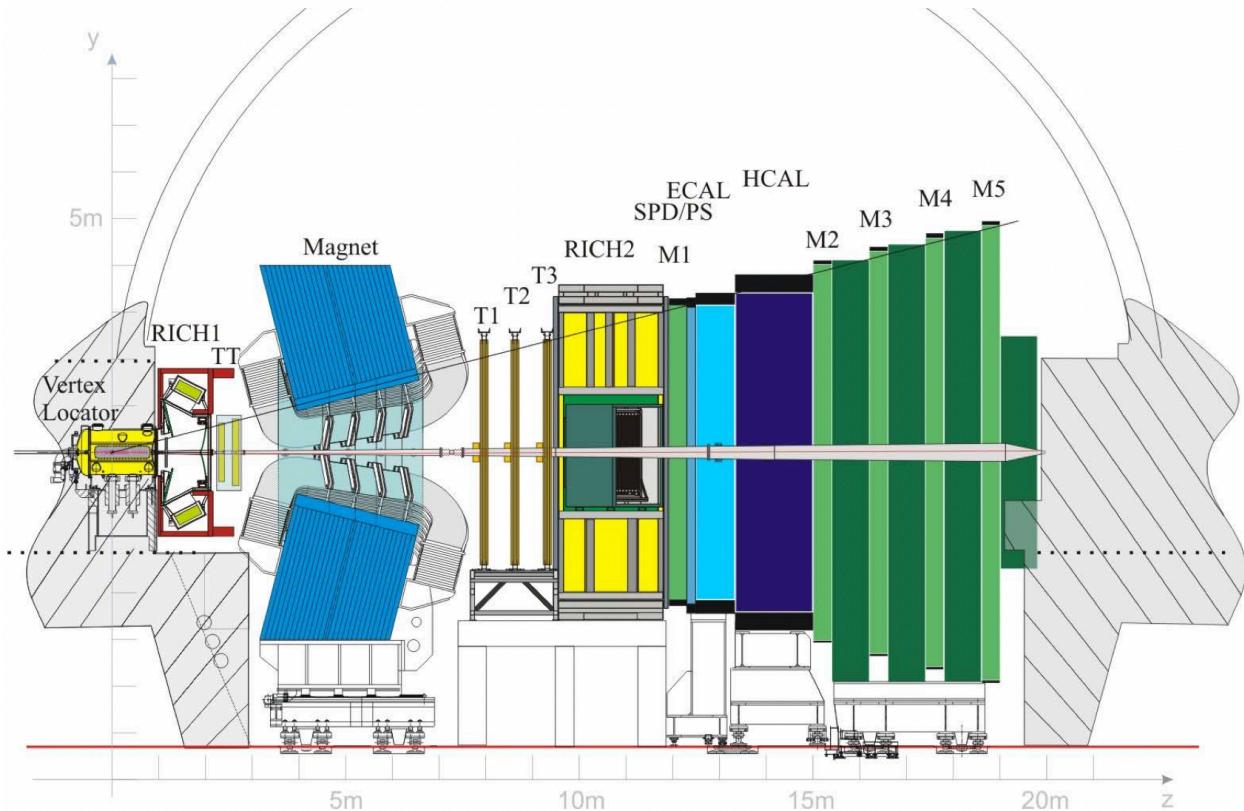
$$\eta = -\log\frac{\theta}{2}, \tag{4.1}$$

Figure 4.2: An overview of the LHCb detector with all its subdetectors in the y-z plane at x = 0. It also shows the scale of the detector. Figure taken from [18].

with θ being the polar angle. The reason for this forward-facing design is that beauty hadrons are predominantly formed in forward-backward region at the LHC[18]. Many of the subdetectors of the LHCb experiment are designed with the specific physics goals in mind. A key feature of b- and c-hadrons is a secondary decay vertex displaced from the primary pp collision vertex. Since b- and c-hadrons often decay via the weak interaction their lifetimes are relatively long. In order to find these secondary vertices and to track charged particles close to the interaction point the Vertex Locator (VELO) was designed. Further tracking of charged particles is done in the Tracker Turicensis (TT), Inner Tracker (IT) and Outer Tracker (OT). Besides tracking charged particles, particle identification (PID) is a crucial aspect of the LHCb detector.

In order to separate signal from background it is important to be able to distinguish between different particle types with high precision. In LHCb the PID is performed by two Ring Imaging Cherenkov (RICH1 and RICH2) detectors, the calorimeters and the muon stations. The energy deposited by the photons, electrons and hadrons is measured in the electronic and hadronic calorimeters. A schematic overview of the LHCb experiment with all its subdetectors can be found in Fig.4.2. Although the LHC can deliver higher luminosities, the LHCb experiment was designed to operate at a luminosity of $\mathcal{L} = 2 \cdot 10^{32}\,\mathrm{cm}^{-2}s^{-1}$. This corresponds to around one visible pp collision per two bunch-crossings.
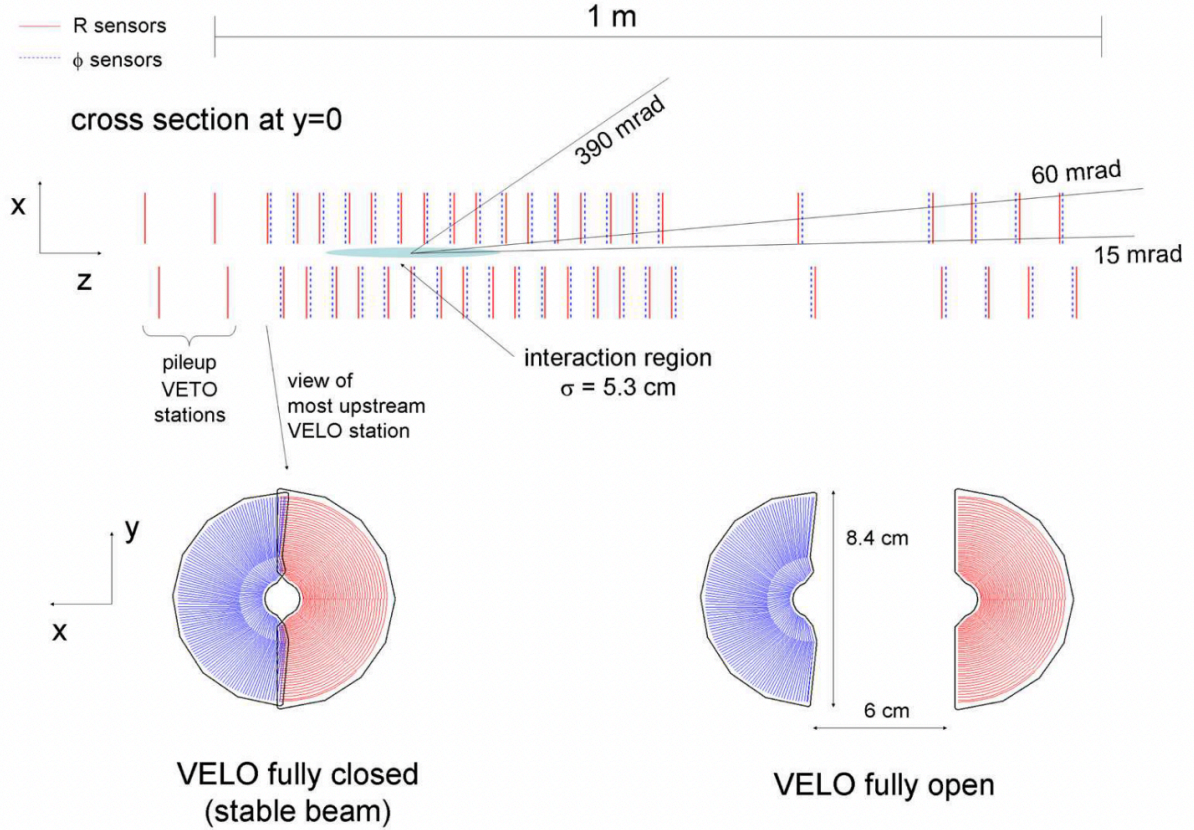
Figure 4.3: (top) A schematic of the VELO in the x-z plane at y = 0. It shows the opening angles at which a particle produced at the interaction point passes through at least three stations (390 mrad) and through the maximum number of stations (15 mrad). (bottom) A view of the VELO in fully closed and fully open position. Figure taken from [18].

4.2.1 VELO

The VELO[18, 57] is a silicon tracker surrounding the interaction point. It consists of two sets of half-circular silicon strip modules perpendicular to the beam-pipe (z-direction), 21 on each side. Each module is able to measure the distance to the beampipe (r) and the angle (ϕ). The VELO can be used the extract precise information on the position of the primary and secondary vertex which is crucial for background rejection. In Fig. 4.3 a schematic overview of the VELO is given.

4.2.2 Tracking detectors

Besides the VELO, LHCb has three additional tracking detectors, the TT, IT and OT. The TT[18, 58, 59] is a large area silicon detector consisting of four modules, located after RICH, before the dipole magnet. It improves the momentum resolution and it is important for the reconstruction of long-lived particles like the Λ-baryon and the K_s^0. Modules 2 and 3 are rotated with an angle of 5° and −5° respectively. This makes the detector sensitive to the

Figure 4.4: A schematic of the Tracking stations T1, T2 and T3. The rotated orientation of the second and third layer of each station can be seen. Figure adapted from [59].

y-coordinate as well.
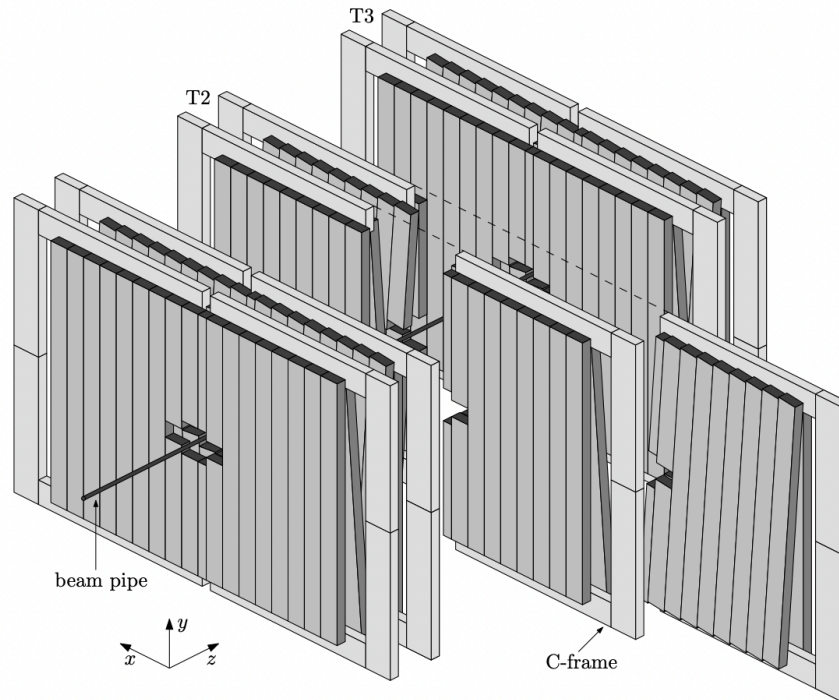
After the TT the particles pass through the LHCb magnet. The LHCb magnet[18] is a warm dipole magnet and it provides a magnetic field of 4 Tm. The polarity of the magnet is periodically reversed during data taking. The magnetic field curves particles of opposite charge in opposite directions. Asymmetries in detectors downstream of the magnet will lead to asymmetries in the detection of particles and anti-particles. Reversing the polarity of the magnet can resolve these effects if there is an equal amount of data of both polarities. The curvature of the charged particles is used to determine the momentum of the particles with great precision.

The IT[18, 58] and OT[18, 59] are combined in three tracking stations downstream of the magnet called T1, T2 and T3. The IT modules are, same as the TT modules, silicon microstrip detectors and are located closest to the beampipe. Around IT are the OT modules which cover the outer part of the T-station area. The OT is a gaseous straw-tube detector consisting of 5 mm wide tubes. Charged particles passing through one of these tubes ionise the gas inside the tube. The position where each charged particle passed through the detector can be determined using the drift time of the electrons through the tube. Each tracking station consists of 4 layers. A schematic of the three tracking stations is given in Fig. 4.4. Similar to the TT modules, in each station layers 2 and 3 are rotated at a an angle of 5º and −5º respectively to provide information on the y-coordinate.
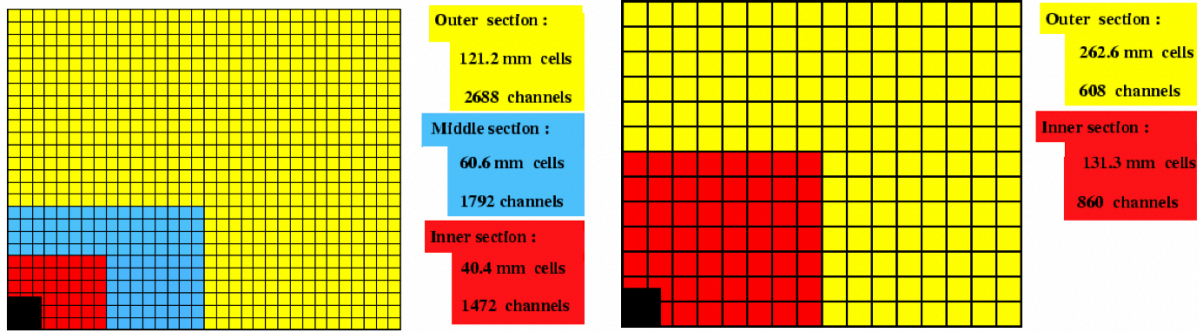
Figure 4.5: (left)The segmentation of the SPD, PS and ECAL. (right) The segmentation of the HCAL. Figure from [61].

4.2.3   RICH

Within LHCb, particle identification of charged particles is performed by the two RICH detectors, next to the calorimeters and the muon stations which will be discussed afterwards. The RICH detectors[18, 60] are Ring Imaging Cherenkov detectors and use, as the name implies, Cherenkov radiation to identify a charged particle. A charged particle travelling through a medium at a velocity higher than the speed of light in that medium emits radiation in the form of light. The angle with respect to the direction of motion at which the photons are emitted is determined by the velocity of the charged particle. This information can be combined with the momentum estimate from the tracking detectors to calculate the mass of said particle.

There are two RICH detectors in LHCb, RICH1 and RICH2, both covering a different momentum range. RICH1 is located in between the VELO and the TT covering a momentum range of 2 to 60 GeV/c. RICH2 is located downstream of the tracking stations before the calorimeters covering a momentum range of 15 to 100 GeV/c.

4.2.4   Calorimeters

The LHCb calorimeter systems[18, 61], positioned downstream from the RICH 2 detector, consist of four elements: a scintillating pad detector (SPD), the pre-shower detectors (PS), an electronic calorimeter (ECAL) and hadronic calorimeter (HCAL). The main goal of the calorimeter system is to measure the energy deposition of different particle types and identify them. The scintillating pad detector and the pre-shower both consist of scintillating pads and have a 15mm thick sheet of lead between them. They have been designed to improve the separation of photons, electrons and hadrons and are mainly used for the first level of the trigger system.

The ECAL has been designed to measure the energy of photons, electrons and π^0 hadrons. It consists of alternating slabs of lead and scintillating pads, containing 25 radiation lengths to capture the full shower of highly energetic photons. Since the particle density increases
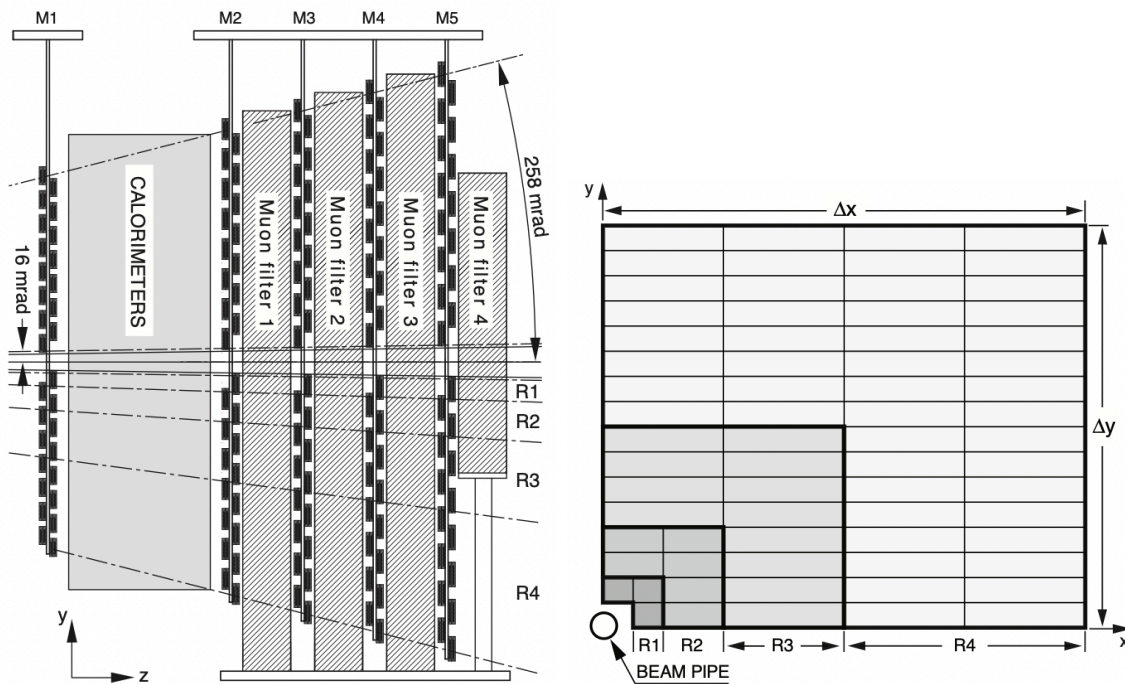
Figure 4.6: (left) A side view of the muon stations of the LHCb detector. (right) The four regions of the muon station in one quadrant. Figure adapted from [18].

close to the beampipe the ECAL is divided into three segments, with a higher density of readout cells closer to the beampipe. The SPD and PS have the same design.

The final part of the calorimeter system of LHCb is the HCAL. The HCAL has alternating layers of iron and scintillators containing 5.6 radiation lengths and it absorbs most of the hadronic showers, providing information on their energy. In contrast to the SPD, PS and ECAL the HCAL consists of only two segments. The layout of the different parts of the calorimeter system is illustrated in Fig. 4.5.

4.2.5 Muon Stations

The LHCb muon detector[18, 62] consists of 5 stations (M1-M5). Since muons hardly interact in the calorimeters 4 of the 5 muon stations (M2-M5) are located after the calorimeter system while M1 is located between RICH2 and the calorimeter system, as can be seen in Fig.4.6. Between the muon stations M2-M5 additional slabs of iron are placed to further reduce the hadronic background. Due to these additional iron slabs the minimum momentum of the muon to be detected must be 6 GeV/c. All the muon stations consist of multi-wire proportional chambers (MWPC), except for the part of M1 closest to the beampipe. This part consists of triple gas electron multiplier (GEM) detectors. The MWPC's and GEM detectors are based on the same physics principles as the OT, however their design is different. Each station consists of four regions, increasing in size further away from the beampipe to retain similar particle density. These regions are shown in Fig. 4.6.
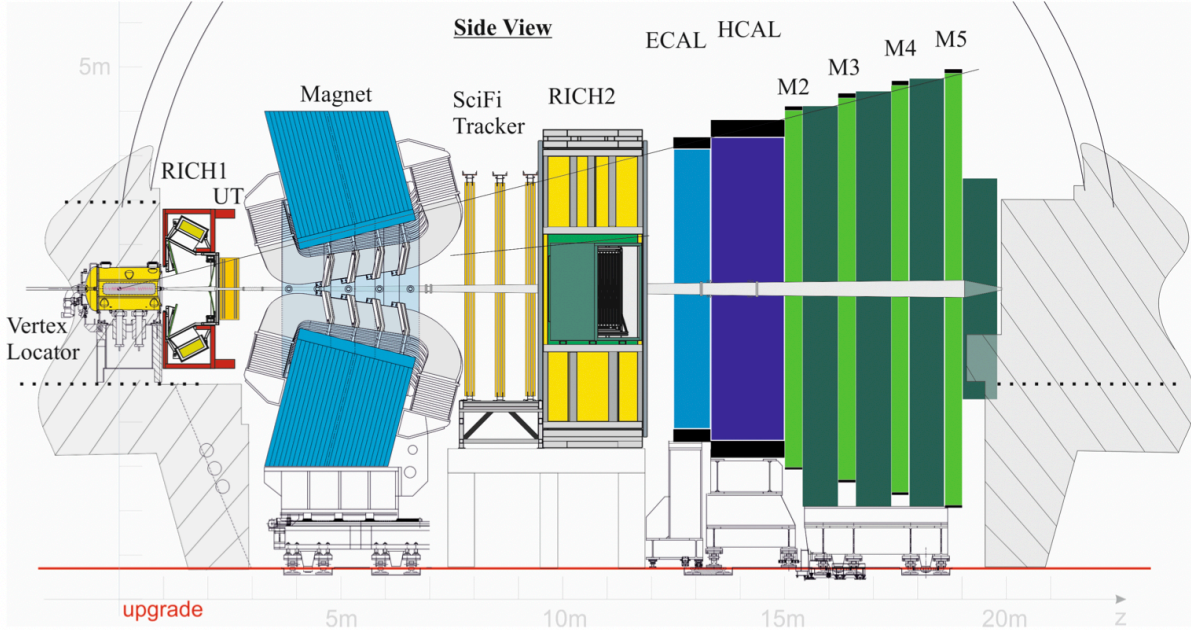
Figure 4.7: An overview of the upgraded LHCb detector in the y-z plane at x = 0. It also shows the scale of the detector. Figure taken from [63].

4.3 LHCb upgrade

During the long shutdown 2 (LS2) from 2019-2022 the LHCb experiment has received multiple upgrades to transform the experiment into a more general-purpose detector in the forward direction[64]. Besides this, the read-out frequency of the LHCb detector will be increased from 1 MHz to 40 MHz. To be able to deal with the increased luminosity substantial changes have been made to some subdetectors, while some detector only required minor upgrades. The VELO, TT, OT, UT, RICH, SPD and PS have all been upgraded or replaced. The magnet remained completely unchanged while the calorimeters and muon stations have received minor changes or upgrades. An overview of the upgraded LHCb detector can be found in Fig. 4.7. The trigger systems have received a drastic upgraded as well, but that will be discussed in the next chapter.

4.3.1 VELO upgrade

The silicon detectors inside the VELO have been completely redesigned and replaced. This upgrade is covered in detail in [65]. I will give the main points here. The new VELO consists of 26 stations, consisting of two L-shaped modules of hybrid pixel detectors. The new modules can be placed closer to the beampipe and the amount of material used is decreased drastically as well. The upgraded VELO can handle higher luminosities up to $\mathcal{L} = 2 \cdot 10^{33}\,\mathrm{cm}^{-2}s^{-1}$. The readout electronics have been upgraded as well to accommodate for the upgraded trigger system.

4.3.2 Tracking upgrade

The tracking systems have received major upgrades in LS2. These upgrades are described in detail in [66]. Below I will give a short summary of the main points.

Upstream tracker

In LS2 the TT and tracking stations (IT and OT) were replaced by two new tracking detectors. The tracking detector before the magnet, the TT in Run 1 and 2, is replaced by the new upstream tracker (UT). The UT detector is a new silicon micro-strip detector with increased granularity. Like the TT, it is composed of 4 planes with the two middle planes placed at a an angle of ±5°, however the acceptance is increased with respect to the TT.

Scintillating fibre tracker

The three T-stations are replaced by a new detector based on scintillating thin fibres, the SciFi detector. While the T-stations consisted of two separate detectors, the IT and OT, the new downstream tracking will be done by the SciFi only. The general design of the SciFi is very similar to the T-stations. It consists of 3 stations with 4 detection layers each. The middle two layers are again placed at an angle of ±5°. Each detection layer is divided vertically into 12 modules and each module consists of 6 layers of scintillating fibres close to the beampipe and 5 layers everywhere else.

4.3.3 Particle identification

In LS2 the particle identification systems of the LHCb detector have received multiple upgrades. These upgrades are described in detail in [67]. I will give a short summary of the upgrades below.

RICH upgrade

The RICH detectors have been upgraded as well, although the changes are smaller compared to the VELO and the tracking system. The layout of the two RICH detectors remains the same. RICH1 has received modifications to its optical system and a specific part used in Run 1 and 2 has been removed. Both RICH detectors have upgraded photon detectors and electronics to be able to operate at the increased luminosity.

Calorimeter

The calorimeter system has been simplified in the upgrade by removing the SPD and PS detectors. Their main purpose was in the first level of the trigger system, the hardware trigger L0, which has been removed in the upgrade. This will be covered in more detail in the next chapter. The electronics of the ECAL and HCAL have been redesigned and rebuilt completely.

Muon stations

Since the luminosity in future runs will be significantly higher, the particle density in the detectors will increase as well. As a result of this increase the M1 station of the muon system has been removed, since it cannot cope with the increased particle flux. Additional shielding is placed after the HCAL around the beampipe in front of M2 to reduce particle flux in that region, which is expected to be high. Similarly to the other subdetectors the readout electronics has been redesigned and replaced to accommodate for the higher luminosity.

Chapter 5

LHCb trigger system

During the data-taking the trigger system is responsible for filtering the amount of information saved by the LHCb experiment and making sure potential interesting events are selected. The LHCb trigger system uses information from all subdetectors to decide which events to save. The trigger system reduces the initial collision rate from the order of 10 MHz (30 MHz in Run 3) to a couple of KHz which can be saved to the disks. Just as the LHCb detector itself the trigger system has received a major upgrade during LS2. In this chapter the trigger system during Run 1 and 2 will be discussed, as well as the system during Run 3.

5.1   Run 1 and 2

In Run 1[68] and Run 2[69] the LHCb trigger system consisted of two separate layers, a hardware trigger (L0) and a software trigger (High Level Trigger). The L0 reduced the rate from the order of 10 MHz to 1 MHz using information from the calorimeters and the muon stations. The High Level Trigger (HLT) reduced the rate further to around 5 KHz in Run 1 and 12,5 KHz in Run 2.

5.1.1   Hardware trigger

The hardware trigger L0 consists of three separate triggers: the calorimeter trigger, the muon trigger and the pile-up trigger. The pile-up trigger is used to help determine the luminosity and not for selecting potential physics events, therefor this trigger will not be considered in this chapter. The calorimeter trigger makes use of information from the entire calorimeter system to select events with particles that have a high transverse energy. Based on the signal a particle leaves in each part of the calorimeter system the L0 trigger has the ability to distinguish between electrons, photons or hadrons. For each particle type there is a separate transverse energy threshold needed to activate the L0 trigger.
The muon trigger uses information from only the muon stations to trigger on events containing one or more muons. The muon trigger searches for straight lines in each quadrant of the
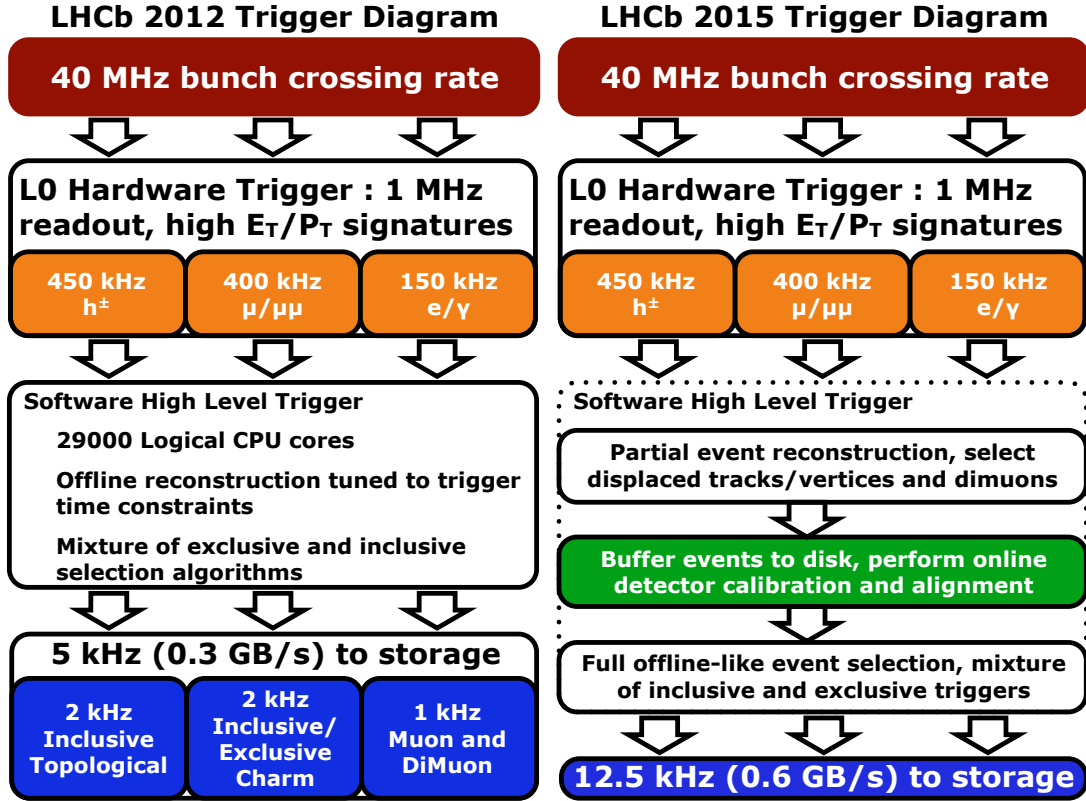
LHCb 2012 Trigger Diagram

40 MHz bunch crossing rate

L0 Hardware Trigger : 1 MHz readout, high E_T/P_T signatures

| 450 kHz h± | 400 kHz µ/µµ | 150 kHz e/γ |

Software High Level Trigger

29000 Logical CPU cores

Offline reconstruction tuned to trigger time constraints

Mixture of exclusive and inclusive selection algorithms

5 kHz (0.3 GB/s) to storage

| 2 kHz Inclusive Topological | 2 kHz Inclusive/ Exclusive Charm | 1 kHz Muon and DiMuon |

LHCb 2015 Trigger Diagram

40 MHz bunch crossing rate

L0 Hardware Trigger : 1 MHz readout, high E_T/P_T signatures

| 450 kHz h± | 400 kHz µ/µµ | 150 kHz e/γ |

Software High Level Trigger

Partial event reconstruction, select displaced tracks/vertices and dimuons

Buffer events to disk, perform online detector calibration and alignment

Full offline-like event selection, mixture of inclusive and exclusive triggers

12.5 kHz (0.6 GB/s) to storage

Figure 5.1: A schematic view of the LHCb trigger system during Run 1 (left) and Run 2 (right).[70]

muon detector pointing back to the collision vertex in the $y-z$ plane[1] and selects tracks with the highest and second highest p_T. Then a decision is made if one track meets the minimum p_T requirement or if the product of the two transverse momenta is large enough.

These four different triggers stages reduce the event rate to around 1 MHz. The events passing the hardware triggers are sent to the software trigger, HLT, which will further reduce the event rate. The L0 trigger remained the same in Run 1 and Run 2, except for the transverse energy thresholds in the calorimeter trigger.

5.1.2   Software trigger

HLT consists of two consecutive layers, HLT1 and HLT2, and it is run on a farm of multi-processors PCs called the Event Filter Farm (EFF). In HLT1 a partial event reconstruction is run to reduce the rate far enough so that a full event reconstruction can be run in HLT2. Both HLT1 and HLT2 work with a concept known as *trigger lines*. Trigger lines are a set of selection criteria based on information from the (partially) reconstructed event that an event must meet to pass the trigger. The combination of the L0 trigger with the HLT trigger lines

---

[1]The LHCb magnet does not bend particles in the $y-z$ plane since the strength of the magnet in the $y-z$ plane is negligible.

form a unique combination that has its own Trigger Configuration Key (TCK). The TCK is saved for each event that passes the trigger. The general structure of the HLT is the same in Run 1 and Run 2, up to some minor differences. At first HLT in Run 1 will be covered and afterwards the changes in Run 2 will be discussed.

Run 1

As mentioned before a partial event reconstruction was run in HLT1, making use of the information from the VELO, TT, tracking stations and muon stations. Information from the VELO was used to find the mean position of the interaction vertex in the $x - y$ plane, which was already done during the LHC fill. Vertices close to this mean position, i.e. within $300\mu m$, from which at least five tracks originate were considered as primary vertices. In HLT1 selections were made based on the impact parameter (IP)[2] and on the quality of the track. For muon candidates passing the L0 a search was performed to find VELO tracks that, combined with hits from the muon stations, form a muon candidate with a minimum track momentum of 6GeV/c. For candidate tracks, selected by either their IP or as a muon candidate, a search was performed for further hits in the T-stations, based on a minimum (transverse) momentum. Each candidate track was then fitted and the quality of the fit was determined. The quality of the HLT1 reconstruction was sufficient to place cuts on IP, momentum and mass of the charged particle that left the track. HLT1 reduced the rate from 1 MHz to 43 kHz.

In HLT2 a more complete event reconstruction was run using information from all subdetectors, however it was still simplified compared to the full offline reconstruction. A forward reconstruction algorithm was run starting from the VELO tracks. Due to the limited computing time per event the PID information from RICH could not be used. Muons and electrons could be identified using information from the muon stations and the ECAL respectively. The output of HLT2 can roughly be divided into three categories: inclusive topological trigger lines, exclusive trigger lines and muon trigger lines. Topological trigger lines are designed to trigger on partially reconstructed b-hadron decays, provided they have at least two charged particles in the final state. Exclusive trigger lines are designed to trigger on specific, fully reconstructed decays. Finally muon trigger lines are designed to trigger on events with muons. HLT2 reduced the event rate from 43 kHz to 5kHz which could be written away to the data storage. The full trigger scheme can be found in Figure 5.1.

Run 2

For Run 2 a number of changes were made both to HLT1 and HLT2[69]. The main change in HLT1 was that next to hits in VELO, T-stations and muons stations hits from the TT were used as well to perform track reconstruction. In contrast with Run 1, during Run 2 a full event reconstruction was run in HLT2. This is performed in three main steps: the track reconstruction of charged particles, the reconstruction of neutral particles and PID. In Run 2 again a mixture of inclusive and exclusive trigger lines were used, but due to improvements in the software a higher event rate could be written away to data storage.

---

[2]The impact parameter is distance of closest approach between a reconstructed track and the true origin of the particle.

LHCb Upgrade Trigger Diagram

**30 MHz inelastic event rate
(full rate event building)**

Software High Level Trigger

**Full event reconstruction, inclusive and
exclusive kinematic/geometric selections**

**Buffer events to disk, perform online
detector calibration and alignment**

**Add offline precision particle identification
and track quality information to selections**

**Output full event information for inclusive
triggers, trigger candidates and related
primary vertices for exclusive triggers**
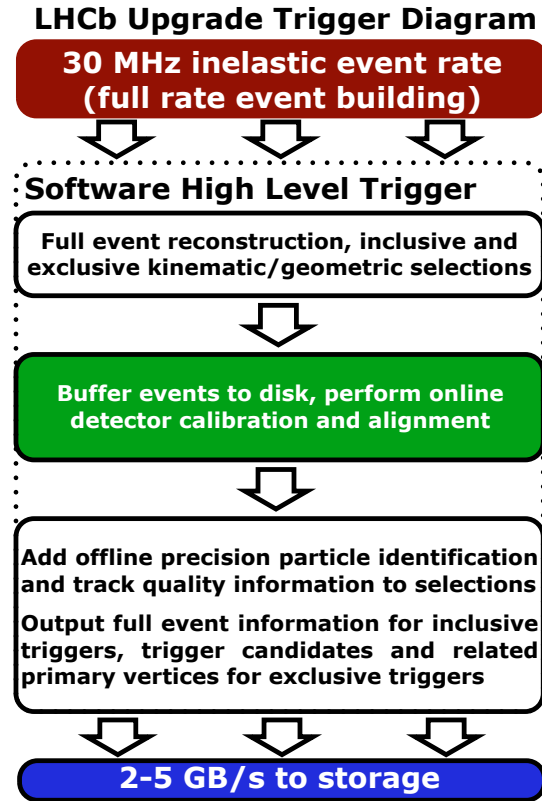
2-5 GB/s to storage

Figure 5.2: A schematic view of the LHCb trigger system during Run 3[70].

5.2   Run 3: Online software trigger

During LS2 the LHCb detector was upgraded to run at a higher luminosity and therefore to read out the detector at a higher event frequency. In order to achieve this the LHCb trigger system was upgraded as well[71]. The decision was made to remove the L0 hardware trigger and implement a full online software trigger, making it possible to read out the detector a 30 MHz event rate. The trigger system will only consist of HLT1 and HLT2. This means HLT1 has to be able to process at a 30 times higher event rate during Run 3 compared to Run 1 and Run 2.

To be able to run at this high event rate the high level trigger needed to be redesigned. Two options for the full software trigger were considered by the LHCb collaboration: A homogeneous system where both HLT1 and HLT2 are run on CPUs and a hybrid system where HLT1 will be run on GPUs and HLT2 will be run on CPUs[72]. The performance of both solutions were studied in detail including a cost-benefit assessment. It was decided to implement the hybrid HLT for Run 3 based on this study.
Running HLT1 on GPUs means that the entire software has to be redesigned. The new software for the HLT1 is encompassed in the Allen project [73]. Within the new HLT1 design trigger decisions will be made with information from the tracking detectors and the muon stations. In HLT2 a full online event reconstruction will be performed. The amount of data

that can be stored on disk will increase with one order of magnitude. Similarly as in Run 1 and Run 2 a collection of inclusive and exclusive trigger lines will be used. A schematic of the trigger scheme to be used in Run 3 can be found in Fig. 5.2.

Chapter 6

Analysis of $B_{(s)} \rightarrow \tau\mu$ in Run 2 and Run 3

The LHCb collaboration has performed a search for $B_{(s)} \rightarrow \tau\mu$ in the Run 1 data and the current limit is set on $\mathcal{B} < 4.2 \times 10^{-5}$ at the 95% confidence level[1][22]. As mentioned in the introduction certain NP models could shift the branching fraction of this decay from 10^{-54} in the SM up to even 10^{-5}, which would be in the range of the LHCb detector. Setting a stricter limit on this decay would impact the allowed parameter space of these NP models and finding this decay would be a direct proof of new physics beyond the Standard Model.

In this thesis preparations will be made for this search in Run 2 and Run 3. Similarly to the previous analysis the focus will be on decays where the τ decays hadronically via $\tau \rightarrow \pi^+\pi^-\pi^+\nu_\tau$. This decay mode has a smaller branching fraction than its decay to a μ and ν_μ, $17.39 \pm 0.04\%$ versus $9.02 \pm 0.05\%$[74], but the two neutrinos in this decay mode make it very complicated to reconstruct the τ[2]. The missing momentum from the tau-neutrino in the hadronic decay can be reconstructed analytically, as will be discussed in this chapter. For this reason only this decay channel is considered.

In order to gather more data containing potential $B_{(s)} \rightarrow \tau\mu$ events an exclusive HLT2 trigger line will be written for Run 3. This trigger line will enable the collaboration to gather more data containing potential interesting events, in addition to the additional data due to the increased luminosity.

A start will be made on the analysis of the Run 2 data, searching for this decay in the data gathered from 2015 to 2018. At first an overview of the main steps of the analysis will be given. Due to time constraints the analysis could not be performed in its entirety. The parts of the analysis that have been executed will be covered in more detail in this chapter as well. These parts are the study of potential Λ_b backgrounds with RapidSim, the analytic reconstruction of the $B_{(s)}$-mass due to the missing neutrino and the invariant mass fit on the normalisation channel MC simulation samples[3].

---

[1]This is under the assumption there is no contribution from B^0 decays.

[2]Neutrinos cannot be detected in the LHCb detector.

[3]Throughout the rest of the thesis Monte Carlo simulation samples will simply be referred to as MC samples.
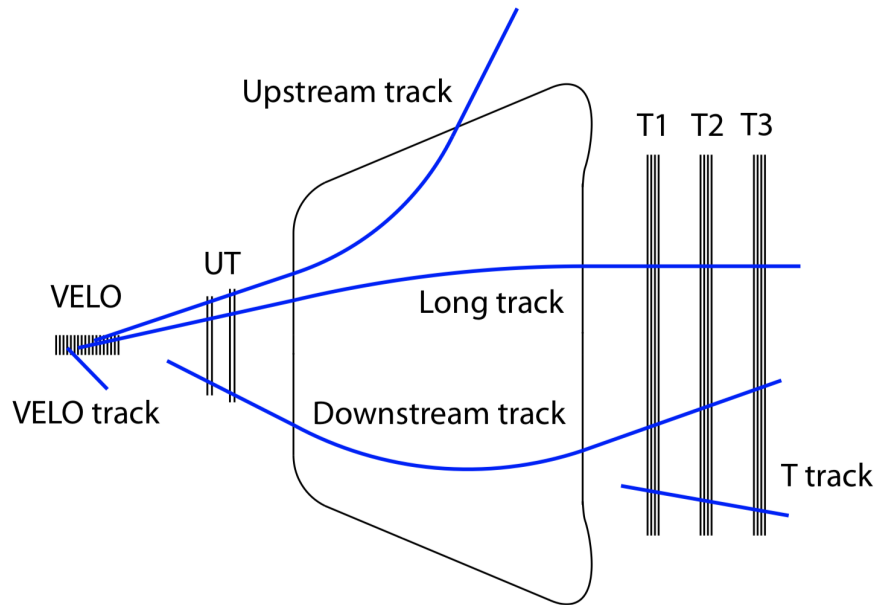
Figure 6.1: Different track types for charged particles, as defined in LHCb. Figure taken from [75].

6.1 Writing an HLT2 trigger lines for $B_{(s)} \to \tau\mu$

A major part of this thesis was the design of an exclusive HLT2 trigger line for $B_{(s)} \to \tau\mu$ events, where the τ decays hadronically to three pions and a τ-neutrino. As explained in the previous chapter the LHCb trigger systems works with the concept of trigger lines. A trigger line is a combination of selection criteria that an event must pass in order for the event to be either passed on to the next trigger level or for the event to be saved. In HLT2 a full event reconstruction is run. This means one can make a selection on all information from the detector. In this section, after covering the basic structure of the code, an overview will be given on the selection criteria that are used an what they are based on, namely the efficiency and rate of the trigger line.

6.1.1 Structure of the code

All trigger lines of the LHCb collaboration live in a software project called Moore[76]. The trigger line for $B_{(s)} \to \tau\mu$ is only one of the hundreds of lines. For a large collaboration it is important that the software is well-organised and that there is as little redundancy in the code as possible. To ensure the same structure an similar selection criteria are used within similar analyses the different physics working groups[4] within LHCb share much of the code. The code for a trigger line essentially consists of two separate type of files: *builders* and *lines*.

---

[4]Within LHCb working groups are divided according to the topic of the physics analyses. As an example, there is a rare decay and a charm working group focusing on analyses of rare decays and charmed decays respectively.

There are several layers of builder files. In the first basic builder files the information from the full event reconstruction is retrieved, in which the particles have already been identified, to create general particle objects without any selection criteria. There is distinction however in types of track (upstream, downstream or long, see Fig. 6.1), RICH signal for hadrons and bremsstrahlung-reconstruction for electrons. These builder files are used by all working groups. The next layer of builders is working group specific. For our trigger line the builders from the rare decays (rd) working group will be used. In the next builder file the rd-specific particle objects are created by passing these particles through a filter that places loose cuts on properties such as momentum, PID and impact parameter. The final layer of builder files are again a set of filters posing more strict, often event-specific cuts on the particle objects. In addition to stricter selection criteria this layer of builder files is also the place where unstable particles in the decay are created. This is done by combining the particle objects and placing requirements on the combination of the decay products such as the distance of closest approach (DOCA) of the tracks. As an example: in the builder file for our specific decay the $B_{(s)}$-meson is built by combining a muon and a tau.

The second type of files are the files containing the trigger lines. In these files a trigger line is built for each specific decay. The particle objects are built using the functions from the builder files and passed to the HLT2-line builder function, which is universal for all HLT2-trigger lines. Once the code for the different lines is built they have to be tested and optimised on their rate and efficiency.

6.1.2 Efficiencies and rates

In a perfect world the trigger line would fire on all the $B_{(s)} \to \tau\mu$ events in the detector and not fire on any other event. Sadly we do not live in a perfect world so the cuts in the trigger line have to be implemented in such a way that it triggers on as many signal events as possible, without triggering on other events. This last part is crucial since there is a limited amount of bandwidth for each trigger line due to the overall limitation on the amount of data that can be stored to disk.

The efficiency of our trigger line has to be optimised to fire on as much signal as possible. This is done by using a dedicated MC sample and checking how many events pass the requirements. Additional tests are performed to check if there is no clear bias within the trigger selection requirements.

To study the efficiency dedicated MC samples are produced with upgrade conditions for both magnet polarities. For each polarity the trigger line is run over 20000 events to study a potential bias in magnet polarity. Afterwards the ratio of the events that could have been reconstructed and the events on which the trigger line fired are studied to see how the reconstruction efficiency behaves as a function of pseudorapidity and transverse momentum. To test the rate the trigger line is run over a minimum bias sample, which is a sample containing a random mix of processes as one would have in real unfiltered data. The rate over this minimum bias sample is indicative for the rate of the line when used during data taking. As mentioned before the rate cannot be too large. In the optimisation of the selection criteria the rate over the minimum bias sample is leading.

6.2 An overview of the $B_s \to \tau\mu$ analysis workflow

The search for $B_s \to \tau(\to \pi^+\pi^-\pi^+\nu_\tau)\mu$ consists of multiple steps. In this section the workflow of this analysis will be discussed, which will be largely the same as the previous analysis[22]. The goal of this analysis is to search for the decay $B_s \to \tau\mu$ and either set a limit on its branching ratio if no events are found or to determine the branching ratio if some events are found. The branching ratio is determined using a normalisation channel. The normalisation channel for $B_s \to \tau\mu$ will be $B^0 \to D^-(\to K^+\pi^-\pi^-)\pi^+$. The reason for this normalisation channel is two-fold: it is a decay with a relatively high branching ratio and its decay topology is very similar to the $B_s \to \tau\mu$ decay. The branching ratio is given by

$$\mathcal{B}(B_s \to \tau\mu) = \alpha^{\mathrm{norm}} \cdot N^{\mathrm{sig}}, \tag{6.1}$$

where the normalisation factor α^{norm} is given by

$$\alpha^{\mathrm{norm}} = \frac{f_{B^0}}{f_{B_s}} \frac{\mathcal{B}(B^0 \to D^-(\to K^+\pi^-\pi^-)\pi^+)}{\mathcal{B}(\tau \to \pi^+\pi^-\pi^+\nu_\tau)} \frac{\epsilon_{B\to D\pi}}{\epsilon_{B\to\tau\mu}} \frac{1}{N^{\mathrm{norm}}}. \tag{6.2}$$

In the normalisation factor the hadronisation fraction of the b-quark into either a B^0 or a B_s meson, the efficiencies of selections and reconstruction of both decays, the branching fraction the normalisation channel and the fact that only one decay channel of the τ-lepton is considered are all taken into account. Now the reason for using a normalisation channel becomes apparent as well. Since the final branching fraction is calculated using a ratio with the normalisation channel (almost) all systematic uncertainties due to the detector cancel out.

The first step of the analysis, after choosing the event samples including trigger and stripping requirements, is to perform the event reconstruction. The neutrino from the hadronic τ decay is not observed by the LHCb detector. However, since information on the position of the τ-decay vertex is available one can analytically reconstruct the missing information, up to a two-fold ambiguity. This will be shown explicitly later on in this chapter. Once the $B_{(s)}$-mass is reconstructed a signal region is defined using the Monte-Carlo data. This signal region will be blinded, or covered up, throughout the analysis until the analysis strategy is final, unblinding only for the final measurement. This is done to prevent human biases.
The next step in the analysis will be the entanglement of signal and background events. As in many analyses one wants to remove as much background as possible while retaining as many signal events as possible. Background will be removed offline in a couple of steps. First a pre-selection will be made via a set of cuts using parameters that are effective in vetoing potential dangerous backgrounds and via a Boosted Decision Tree (BDT)[77] based on isolation variables. After the pre-selection the data will be filtered further in two more steps. First another BDT will be trained to remove combinatorial background contributions and finally a cut will be placed on the τ decay time to remove some specific partially reconstructed backgrounds. In the previous analysis BDTs were used, however many more Machine Learning algorithms could be used to achieve the same goal. For the normalisation channel the offline selection procedure will be a bit more straightforward. A selection of cuts will be applied offline after which the invariant mass distribution will be fitted. The efficiencies of both the signal and normalisation channel will be determined using a combination of Monte Carlo and

data-driven methods.

After all the selection processes a final BDT will be built to divide the final sample into bins with different signal-to-background ratios. A simultaneous fit of the invariant mass distribution[5] will performed in all BDT bins. If, in accordance with the SM, no signal events are found a new limit will be set on the branching ratio of the $B_{(s)} \to \tau\mu$ decay using the CLs method[78].

6.3   Studying Λ_b backgrounds with RapidSim

In this analysis it is crucial to control all potential background sources, since it is a search for a very rare decay. Many of the potential backgrounds will have a higher branching ratio and could easily overshadow a potential signal. Studying backgrounds using full detector simulations can be quite time consuming and some potential background channels might have a negligible impact. Therefore potential background sources are often first studied using a program that can produce events with similar kinematic properties and mass resolutions as in a full detector simulation. Based on this pre-study a decision can be made on whether to study this potential background source in more detail or not.

In this analysis a brief study of a new potential background source for the $B_{(s)} \to \tau\mu$ decay was performed using RapidSim: decays of the Λ_b^0-baryon. This analysis is a new addition to the Run 1 strategy.

6.3.1   RapidSim

RapidSim[79] is a fast Monte Carlo generator for the phase space decay of beauty and charm quark hadrons. It is able to produce millions of events in a few seconds, with similar momentum spectra, efficiency shapes and mass resolutions as obtained from a full detector simulation. RapidSim is based on the ROOT software package[80] and it utilises the TGen-PhaseSpace class to perform the fast simulations. The kinematic properties of the events are calculated using FONLL (fixed order next-to-leading log)[81] calculations. Events are generated with the kinematic properties as if they were produced in pp collisions at the LHC and are within the geometric acceptance of the LHCb-detector.

Next to studying the invariant mass shape and kinematic properties of heavy-quark hadron decays it is also possible to study the invariant mass shape of partially reconstructed decays.

6.3.2   Potential background channels

To form a potential background source the decay products of the Λ_b^0-baryon should contain the same final state particles as in the $B_{(s)} \to (\tau \to 3\pi\nu_\tau)\mu$ decay. A list of the considered decay channels can be found in Table 6.1. All the decays will be partially reconstructed decays, not reconstructing the decay products of the Λ^0 decaying into $p\pi^-$ or $n\pi^0$. Events of

---

[5]An invariant mass distribution shows the number of candidates with a certain invariant mass. If some particle decay is successfully extracted from the data, there will be a peak in the invariant mass distribution at the combined mass of the decay products.

Table 6.1: The different decay channels considered in the RapidSim simulations. In all cases the decays were partially reconstructed, not reconstructing the Λ^0 decay products.

Channel	Decay	Branching Ratio
1	$\overline{\Lambda}_b^0 \to (\Lambda_c^- \to \overline{\Lambda}^0 \mu^- \overline{\nu}_\mu)\pi^+\pi^-\pi^+$	$2.70 * 10^{-4}$
2	$\Lambda_b^0 \to (\Lambda_c^+ \to \Lambda\pi^+\pi^-\pi^+)\mu^-\overline{\nu}_\mu$	$7.52 * 10^{-4}$
3	$\overline{\Lambda}_b^0 \to (\Lambda_c^- \to \overline{\Lambda}^0 \mu^- \overline{\nu}_\mu)(\tau^+ \to \pi^+\pi^-\pi^+\overline{\nu}_\tau)\nu_\tau$	$6.77 * 10^{-5}$
4	$\Lambda_b^0 \to (\Lambda_c^+ \to \Lambda^0\pi^+\pi^-\pi^+)(\tau^- \to \mu^-\overline{\nu}_\mu\nu_\tau)\overline{\nu}_\tau$	$1.31 * 10^{-4}$
5	$\Lambda_b^0 \to (\Lambda_c^+ \to \Lambda^0\pi^+)\pi^-\pi^+\mu^-\overline{\nu}_\mu$	$2.43 * 10^{-4}$
6	$\Lambda_b^0 \to (\Lambda_c^+ \to \Lambda^0\pi^+)\pi^-\pi^+(\tau^- \to \mu^-\overline{\nu}_\mu\nu_\tau)\overline{\nu}_\tau$	$4.23 * 10^{-5}$
7	$\Lambda_b^0 \to (\Lambda_c^+ \to \Lambda^0\pi^+\pi^-\pi^+)(D_s^- \to \mu^-\overline{\nu}_\mu)$	$2.20 * 10^{-6}$
8	$\Lambda_b^0 \to (\Lambda_c^+ \to \Lambda^0\pi^+\pi^-\pi^+)(D_s^- \to (\tau^- \to \mu^-\overline{\nu}_\mu\nu_\tau)\overline{\nu}_\tau)$	$3.93 * 10^{-6}$
9	$\overline{\Lambda}_b^0 \to (\Lambda_c^- \to \overline{\Lambda}^0 \mu^- \overline{\nu}_\mu)(D_s^+ \to \pi^+\pi^-\pi^+)$	$4.16 * 10^{-6}$
10	$\overline{\Lambda}_b^0 \to (\Lambda_c^- \to \overline{\Lambda}^0 \mu^- \overline{\nu}_\mu)(D_s^+ \to (\tau^+ \to \pi^+\pi^-\pi^+\overline{\nu}_\tau)\nu_\tau)$	$2.02 * 10^{-6}$

the different channels were produced according to their branching ratio and their cumulative invariant mass shape will be studied. Misidentified Λ_b^0-decays are not taken into account since their branching ratio would be heavily suppressed, considering the PID efficiency of the LHCb detector.

6.3.3 Selection criteria

To see if the partially reconstructed Λ_b^0-baryon decays can be a significant source of background the invariant mass shape of the events is studied. Several kinematic cuts are applied to the momenta, mass and (misidentified) tau vertex. These cuts are the same as in the previous $B_{(s)} \to \tau\mu$ analysis[22]. In Table 6.2 an overview of all the applied cuts can be found. It is important to note that in some decay channels the τ decays leptonically and not hadronically. In these cases, e.g. decay 4, the cuts on the tau are applied to the Λ_c^+ and not on the leptonically decaying tau. The reason for this is that in this case the Λ_c^+-decay produces the τ-like signal and the τ produces the μ-signal. For all decay channels it is checked that the cuts are applied to the correct particles.

6.4 Analytic $B_{(s)}$-mass reconstruction

One of the difficulties of studying the $B_{(s)} \to \tau\mu$ decay resides in the reconstruction of the τ, which always contains at least one neutrino[6]. Since neutrinos cannot be detected by the LHCb detector there will be some missing energy due to the missing neutrinos when reconstructing the τ-lepton, and therefor in the reconstruction of the $B_{(s)}$-meson. As a result the visible invariant mass of the $B_{(s)}$-meson will not peak at the true $B_{(s)}$-meson mass. It is determined using only the information of the three π's from the hadronic τ decay and the

---

[6]This is the case at least within the Standard Model. There are BSM theories for LFV τ-decays but these will not be considered here.

Table 6.2: The applied kinematic cuts to the partially reconstructed Λ_b decays

Particle type	Cut
Λ_b	$p_T > 6000$ MeV/c
	$M \in [2000, 7000]$ MeV/c^2
	$M_{\mathrm{corr}} < 10000$
	$p_T(\mu + 3\pi) > 2500$ MeV/c
τ	$p_T > 1000$ MeV/c
	1 daughter with $p_T > 800$ MeV/c
	$M \in [400, 2100]$ MeV/c^2
	Vertex distance $\rho \in [0.1, 7]$ mm
	Vertex distance $z < 5$ mm
π	$p > 2000$ MeV/c
	$p_T > 250$ MeV/c
μ	$p > 6000$ MeV/c
	$p_T > 1000$ MeV/c

muon. However, due to the three π's the τ decay vertex can be reconstructed. This piece of information together with the position of the primary vertex provides enough information to perform an analytic reconstruction of the missing neutrino momentum and therefor the true $B_{(s)}$-meson mass, up to a two-fold ambiguity. In this section this analytic reconstruction will be performed.

6.4.1 Constraints and assumptions

The missing neutrino momentum and the $B_{(s)}$ decay vertex (V_B), both unknown a priori, will be expressed in terms of the primary vertex (PV), τ-vertex (V_τ), the $3 - \pi$ 4-momentum ($P_{3\pi}$) and the muon 4-momentum (P_μ), which all are measured experimentally. Based on the decay topology a closed set of equations can be constructed and solved for the neutrino momentum (P_ν). To make life a bit easier a convenient frame of reference is chosen, based on the decay plane. The decay plane is defined by the flight direction of the $B_{(s)}$-meson ($\hat{n}_B$), given by the PV and the V_B, and the μ-momentum. The frame of reference, denoted by $\hat{i}\hat{j}\hat{k}$, is defined such that $\hat{i}$ is in the μ-direction, $\hat{j}$ lies in the decay plane and $\hat{k}$ is orthogonal to the decay plane. This decay plane and corresponding frame of reference is depicted in Fig. 6.2. The set of equations based on the constraints of the decay topology are the following:

- The components of the 3π-momentum and ν_τ-momentum outside the decay plane are equal and opposite:

$$p_{3\pi}^k = -p_\nu^k. \tag{6.3}$$

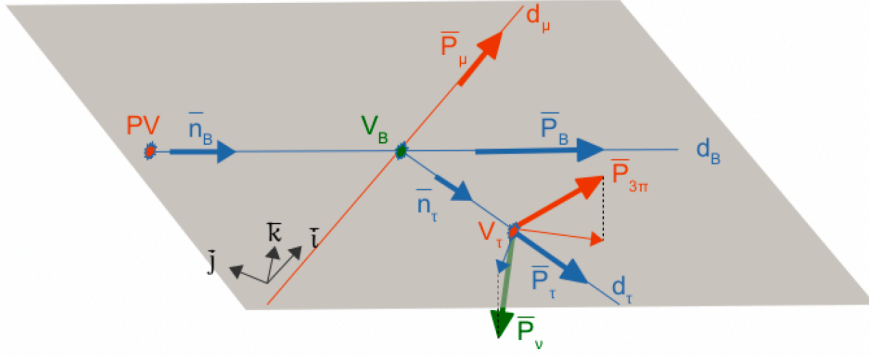- The B decay vertex V_B is along the μ flight direction. Let U_μ be a position on the muon trajectory:

Figure 6.2: The decay plane of $B_{(s)} \to \tau\mu$ given by the $B_{(s)}$-meson flight direction and the μ momentum.

$$\vec{P}_\mu \wedge (U_\mu - V_B) = 0,$$
$$p_\mu^i \left(-U_\mu^j + V_B^j\right) = 0. \tag{6.4}$$

- The $B_{(s)}$-meson momentum will be in the direction defined by the PV and V_B once the neutrino momentum is taken into account:

$$\vec{P}_B \wedge (V_B - PV) = 0,$$
$$\left(p_{3\pi}^j + p_\nu^j\right)\left(V_B^i - PV^i\right) - \left(p_{3\pi}^i + p_\nu^i + p_\mu^i\right)\left(V_B^j - PV^j\right) = 0. \tag{6.5}$$

- The τ momentum will be in the direction defined by V_B and V_τ once the neutrino momentum is taken into account:

$$\vec{P}_\tau \wedge (V_\tau - V_B) = 0,$$
$$\left(p_{3\pi}^i + p_\nu^i\right)\left(V_\tau^j - V_B^j\right) - \left(p_{3\pi}^j + p_\nu^j\right)\left(V_\tau^i - V_B^i\right) = 0. \tag{6.6}$$

- There is 4-momentum conservation at the τ decay vertex V_τ:

$$P_\tau - P_{3\pi} - P_\nu = 0, \tag{6.7}$$

which can be rewritten using $P_\mu P^\mu = M^2$, $E^2 = \vec{p}^2 + M^2$ and $M_\nu = 0$. This gives the last equation of our system of equations:

$$\frac{1}{2}\left(M_\tau^2 - M_{3\pi}^2\right) - p_{3\pi}^i p_\nu^i - p_{3\pi}^j p_\nu^j - p_{3\pi}^k p_\nu^k$$
$$- \sqrt{M_{3\pi}^2 + p_{3\pi}^{i2} + p_{3\pi}^{j2} + p_{3\pi}^{k2}}\sqrt{p_\nu^{i2} + p_\nu^{j2} + p_\nu^{k2}} = 0 \tag{6.8}$$

These equations form a closed system of equations that can be solved for the neutrino momentum. From Equation 6.3 one can find the k-component of the $\vec{p}_\nu$ and from Equation 6.4 one finds V_B^j. Both Equation 6.5 and Equation 6.6 can be written as $V_B^i = ...$ which allows us to eliminate V_B^i as unknown as well. This leads to the following expression:

$$V_\tau^i + \frac{\left(p_{3\pi}^i + p_\nu^i\right)\left(V_B^j - V_\tau^j\right)}{\left(p_{3\pi}^j + p_\nu^j\right)} = PV^i + \frac{\left(p_{3\pi}^i + p_\nu^i + p_\mu^i\right)\left(V_B^j - PV^j\right)}{\left(p_{3\pi}^j + p_\nu^j\right)}. \tag{6.9}$$

From this equation one can find the jth component of the neutrino momentum in terms of p_ν^i and known quantities:

$$p_\nu^j = \frac{1}{\left(V_\tau^i - PV^i\right)}\left[p_\nu^i\left(V_\tau^j - PV^j\right) - p_{3\pi}^i\left(V_\tau^j - PV^j\right) + p_\mu^i\left(V_B^j - PV^j\right)\right] - p_{3\pi}^j. \tag{6.10}$$

We are left with one last unknown, p_ν^i, and one last equation, Equation 6.8. If the expressions for p_ν^k and p_ν^j are plugged into Equation 6.8 one can find a solution for p_ν^i. In this last step the two-fold ambiguity comes around the corner, since one ends up with a quadratic equation of the form $Ap_\nu^{i2} + Bp_\nu^i + C = 0$ which will have two solutions. Using these solutions an expression for p_ν^j can be found as a function of known observables. At this point the neutrino momentum has been reconstructed. The final step of the reconstruction is determining the $B_{(s)}$-meson mass, which is found from conservation of 4-momentum at the $B_{(s)}$-vertex:

$$P_B = P_\mu + P_{3\pi} + P_\nu,$$
$$M_B^2 = \left(\sqrt{M_{3\pi}^2 + p_{3\pi}^{i2} + p_{3\pi}^{j2} + p_{3\pi}^{k2}} + \sqrt{M_\nu^2 + p_\nu^{i2} + p_\nu^{j2} + p_{3\pi}^{k2}} + \sqrt{M_\mu^2 + p_\mu^{i2}}\right)^2 \tag{6.11}$$
$$- \left(p_{3\pi}^i + p_\nu^i + p_\mu^i\right)^2 - \left(p_{3\pi}^j + p_\nu^j\right)^2.$$

One of the requirements of this reconstruction is that the discriminant of the quadratic solution is positive. If the discriminant is positive two masses can be studied, M_B^+ and M_B^-, corresponding to the two neutrino momentum solutions.

6.5   Normalisation channel mass fit

One of the steps that will be performed in preparation of the analysis is the invariant mass fit on the Monte Carlo data of the normalisation channel, $B^0 \to D^-(\to K^+\pi^-\pi^-)\pi^+$. Before performing the mass fit selection criteria were applied on the MC data. These selection criteria correspond to the stripping[7] requirements and offline selections used in the previous analysis. The applied selection criteria can be found in Table 6.3 for the stripping requirements and in Table 6.4 for the offline selection requirements. The selection criteria are based on the decay kinematics, such as the DIRA[8] and quality of the reconstructed tracks, such as impact parameter χ^2.

---

[7]Stripping is the pre-selection that is applied to reconstructed data, before the data is used in an analysis.
[8]The DIRA is defined as the cosine of the angle between the momentum and flight direction of the particle.

Table 6.3: The stripping requirements for the normalisation channel $B^0 \to D^-(\to K^+\pi^-\pi^-)\pi^+$ as implemented in the stripping lines StrippingB2XTau v21 and v21r1.

Particle type	Cut
B^0	$p_T > 5000$ MeV$/c$
	$M \in [2000, 7000]$ MeV$/c^2$
	Flight Distance $\chi^2 < 4000$
	Impact parameter $\chi^2 < 200$
	Flight Distance < 35mm
D	$p_T > 1000$ MeV$/c$
	1 daughter with $p_T > 800$ MeV$/c$
	$M \in [1750, 2080]$ MeV$/c^2$
	DIRA > 0.99
	ORIVX $\chi^2 < 16$
π and K	$p > 2000$ MeV$/c$
	$p_T > 250$ MeV$/c$
	IP $\chi^2 > 16$
	Track χ^2 per DOF < 3
	Track Ghost Prob < 0.3
π	ProbNNpi > 0.55
K	PIDK > -5

Table 6.4: The offline selection requirement applied to the normalisation channel $B^0 \to D^-(\to K^+\pi^-\pi^-)\pi^+$.

Particle type	Cut
B^0	$p_T > 5050$ MeV$/c$
	Endvertex $\chi^2 < 5$
	Flight distance from $PV > 2$
	Lifetime $\chi^2 < 10$
D	$M \in [1850, 1900]$ MeV$/c^2$
	Endvertex $\chi^2 < 6$
	Flight distance χ^2 from OWN$PV > 200$
	Original vertex $\chi^2 < 5$
K from D	PIDK> 15
	$p_T > 750$ MeV$/c$
π from D	Min IP> 0.2

Once the selection criteria are applied to the MC data the invariant mass distribution will be fitted. Our aim is to perform all fits in python using the zfit model fitting library, which is based on TensforFlow[82]. It is a python oriented alternative for the ROOT based RooFit library[83]. The signal will be modelled using a double sided crystal ball (DSCB) PDF. A DSCB is a Gaussian PDF in the centre with, potentially different, exponential tails on both

sides. The DSCB PDF is given by:

$$
f_{\text{CB}}(x, \alpha_L, n_L, \mu, \sigma, \alpha_R, n_R, N) = N \cdot
\begin{cases}
A_L \cdot (B_L - \frac{x-\mu}{\sigma})^{-n_L}, & \text{for } \frac{x-\mu}{\sigma} < -\alpha_L \\
e^{-\frac{(x-\mu)^2}{2\sigma^2}}, & \text{for } \alpha_L \leq \frac{x-\mu}{\sigma} \leq \alpha_R \\
A_R \cdot (B_R - \frac{x-\mu}{\sigma})^{-n_R}, & \text{for } \frac{x-\mu}{\sigma} > \alpha_R,
\end{cases}
\tag{6.12}
$$

where $A_{L,R} = (\frac{n_{L,R}}{|\alpha_{L,R}|})^{n_{L,R}} \cdot e^{-\frac{|\alpha_{L,R}|^2}{2}}$ and $B_{L,R} = \frac{n_{L,R}}{\alpha_{L,R}} - |\alpha_{L,R}|$. The yield is given by the normalisation of the PDF, N. The point where the DSCB goes from the exponential tail to the Gaussian is given by α_L and the point where it goes back into the exponential tail is given by α_R. The Gaussian width and mean are given by σ and μ respectively, while the invariant mass is given by x.

Chapter 7

Results

In the previous chapter the experimental methods of the analyses performed in this thesis were discussed. In this chapter the results of those analyses will be presented. The same order will be followed as before. At first the results for the HLT2 trigger line will be presented, followed by the study of the potential Λ_b backgrounds with RapidSim. Next the results of the analytic reconstruction of the B-meson mass will be presented. Finally the results of the invariant mass fit on the normalisation channel Monte Carlo will be covered. The chapter will end with a section discussing the results.

7.1 HLT2 trigger Line

The results for the HLT2 trigger line consists of two main components as mentioned before: the efficiency and the rate. At first the set of selection criteria used for our trigger line will be discussed. Then the efficiency and rate results will be presented. In addition to the $B_{(s)} \to \tau\mu$ trigger line, a trigger line for the $B_{(s)} \to \tau e$ decay was written as well on request from the collaboration. Since no dedicated MC samples existed for this decay only the rate of this line was considered.

7.1.1 Selection criteria

The trigger line consists of several steps each with its own selection criteria. These selection criteria are the results of a process of optimising the efficiency while keeping the rate of the lines in control. First of all a search is performed on a τ decaying hadronically. Cuts are placed on the π transverse momenta, PID, τ mass, position of the τ-vertex and the χ^2 of the impact parameter reconstruction. For the μ the selection is based on the (transverse) momentum, PID and again on the χ^2 of the impact parameter reconstruction. Finally cuts are placed on the $\tau - \mu$ vertex distance, impact parameter, the DIRA and the B_s mass. In Table 7.1 an overview of all selection criteria is given.

For the $B_{(s)} \to \tau e$ trigger line the same selection criteria were used as in the $B_{(s)} \to \tau\mu$ line, except for the PID requirements. The PID requirement for the electron is tighter in order to control the rate of the trigger line.

Table 7.1: The selection criteria for in the HLT2 trigger line designed to select $B_{(s)} \to \tau\mu$ and $B_{(s)} \to \tau e$ events.

Particle type	Cut
B_s	$M \in [2500, 6000]$ MeV/c^2
	IP χ^2 w.r.t. PV $\in [3, 35]$
	DIRA > 0.99
	FD $\chi^2 > 80$
τ	$p_T > 1000$ MeV/c
	1 daughter with $p_T > 800$ MeV/c
	$M \in [600, 2100]$ MeV/c^2
	IP χ^2 w.r.t. PV $> 12.$
	Vertex distance $\rho \in [0.05, 8]$ mm
	Vertex distance $z > 2$ mm
π	one π with $p_T > 750$ MeV/c
	$p_T > 250$ MeV/c
	$\text{PID}_K < 0.$
μ	$p > 2000$ MeV/c
	$p_T > 500$ MeV/c
	$\text{PID}_\mu > 2.$
	IP χ^2 w.r.t. PV $> 5.$
e	$p > 2000$ MeV/c
	$p_T > 500$ MeV/c
	$\text{PID}_e > 3.$
	IP-χ^2 w.r.t. PV $> 5.$

7.1.2 Efficiencies

The efficiency of the $B_{(s)} \to \tau\mu$ line was tested on dedicated Monte Carlo samples, one for each magnet polarity. For each polarity a sample of 20000 events was used. The efficiency for a positive magnet polarity (mag up) is $3.4 \pm 0.2\%$. For a negative magnet polarity (mag down) the efficiency is $3.9 \pm 0.1\%$. This efficiency is calculated with respect to all events in the MC sample, some of which fall outside the detector geometry. Based on this analysis there is a small polarity bias, in favour of a negative magnet polarity.

In addition to studying the overall efficiency of the trigger line the efficiency of the trigger line as a function of transverse momentum and pseudorapidity is studied as well. The efficiency distributions are studied separately for the τ, μ and B-meson. The efficiency is calculated with respect to reconstructible signal events, i.e. the signal events inside the detector geometry. The distributions are normalised to the yields in order to more clearly visualise the differences in shape between the triggered and reconstructible events. For this reason the efficiency ratios are normalised to 1. These distributions and their ratios are presented in Figure 7.1.

It can be seen that the efficiencies for all three particle types are not flat as a function of the transverse momentum and pseudorapidity. When considering the trigger efficiency as a
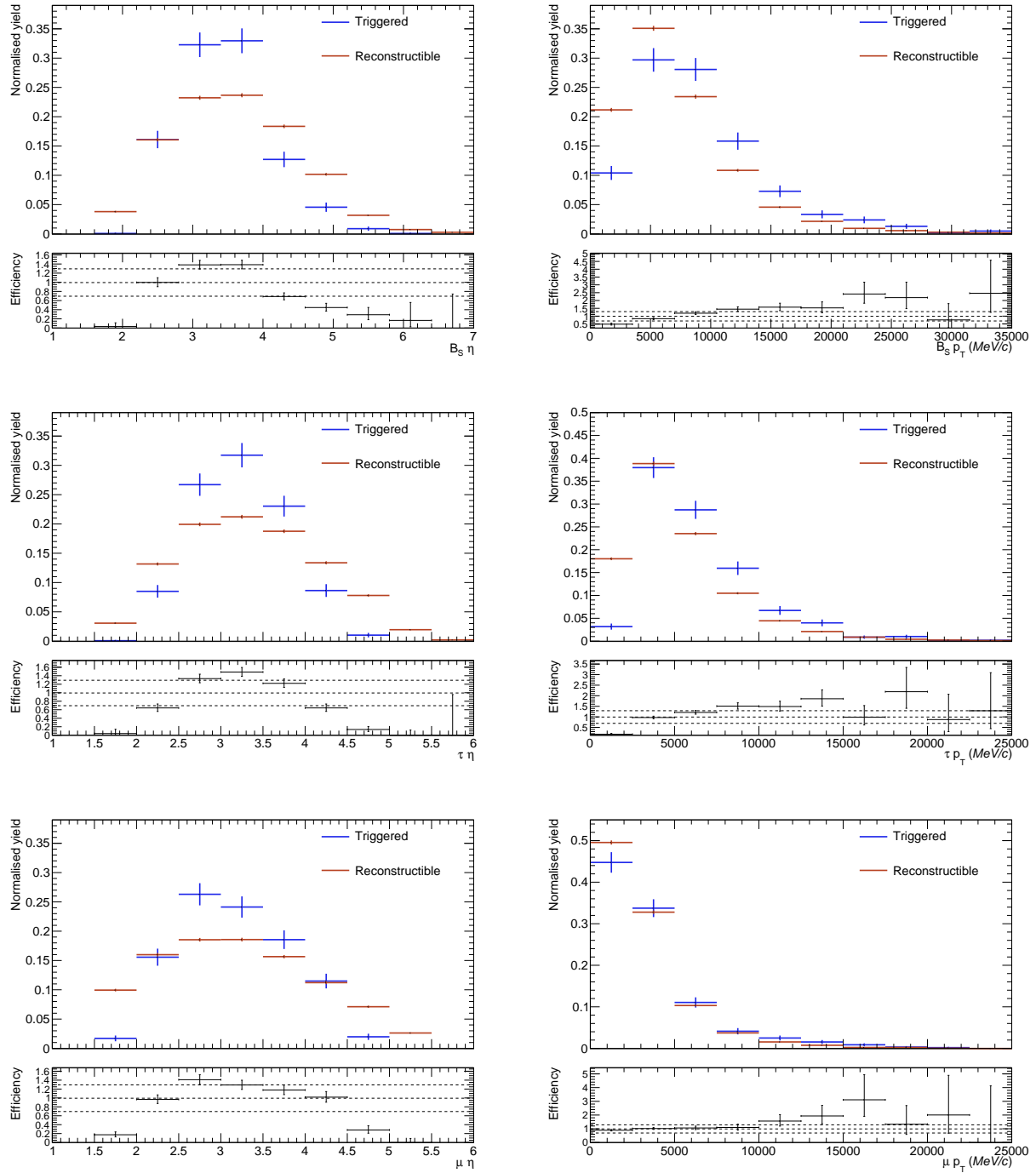
Figure 7.1: The normalised yields of the triggered events over the reconstructible events and their ratio as a function of pseudorapidity (left) and transverse momentum (right) for the B_s-meson (top), τ (middle) and μ (bottom). The distributions have been normalised to their respective yields to compare the shapes of the distributions between the reconstructible events and triggered events.

function of the pseudorapidity one can see that the efficiency is largest in the centre of the detector. The efficiency shape as a function of pseudorapidity is similar for all three particle types. The efficiency distribution as a function of the transverse momentum also no difference can be observed between the three particle types. The distribution of the transverse momentum itself however is different for the μ's on one hand and the τ's and B_s-mesons on the other hand at low transverse momentum. This is to be expected due to the mass differences. The B_s-meson and the τ are much heavier than the muons, leading to a different p_T spectrum.

7.1.3 Rates

Although the efficiency of the trigger line is more interesting from a physics perspective, the trigger rates of the two HLT2 lines were leading in designing the lines. The trigger rates of both the $B_{(s)} \to \tau\mu$ and the $B_{(s)} \to \tau e$ trigger lines were tested using an HLT1 filtered minimum bias sample. The output rates of both trigger lines is 0.0769 ± 0.07kHz.

This trigger rate is acceptable for a very rare decay trigger line. Both trigger lines were checked by experts of the LHCb collaboration and are now incorporated into the LHCb trigger software. They will be used in the data-taking in Run 3 to collect data that can be used in future searches for these decays.

7.2 Λ_b background

The next step in the analysis is a study of potential Λ_b decays entering as a background component in the analysis. A total of 300000 Λ_b events were generated using RapidSim divided over the 10 decay channels, reported in Table 6.1, taking their relative branching fractions into account. As discussed in the previous chapter the events are generated assuming a partially reconstructed decay where the Λ-baryon is not reconstructed.

In the top of Figure 7.2 the cumulative mass distribution can be found. It can already be seen that a large part of the mass distribution falls outside of the B and B_s search window and no clear mass peak can be seen. Once the kinematic cuts from Table 6.2 are applied the number of events reduces drastically from around 300000 events to a bit over 6000 events, which is a reduction of a factor 50. This reduction in events is only due to the kinematic selection criteria. In a full detector simulation one can apply more sophisticated cuts on track properties and fit quality, utilising parameters such as the impact parameter and DIRA. The expectation is that these cuts will fully remove the contribution of partially reconstructed Λ_b decays. Therefore it is unnecessary to perform a full detector simulation for these decays.

7.3 Analytic B-mass reconstruction

The analytic reconstruction of the missing neutrino momentum and the B-meson mass is performed as discussed in the previous chapter. The reconstruction was performed on the 2017 and 2018 $B_{(s)} \to \tau\mu$ Monte-Carlo data, both separated by magnet polarity. Each of the four samples contains around 200000 events. At first the visible B-mass can be seen in Figure 8.1 for both magnet polarities in the 2018 MC data. It is clear that the visible mass does not
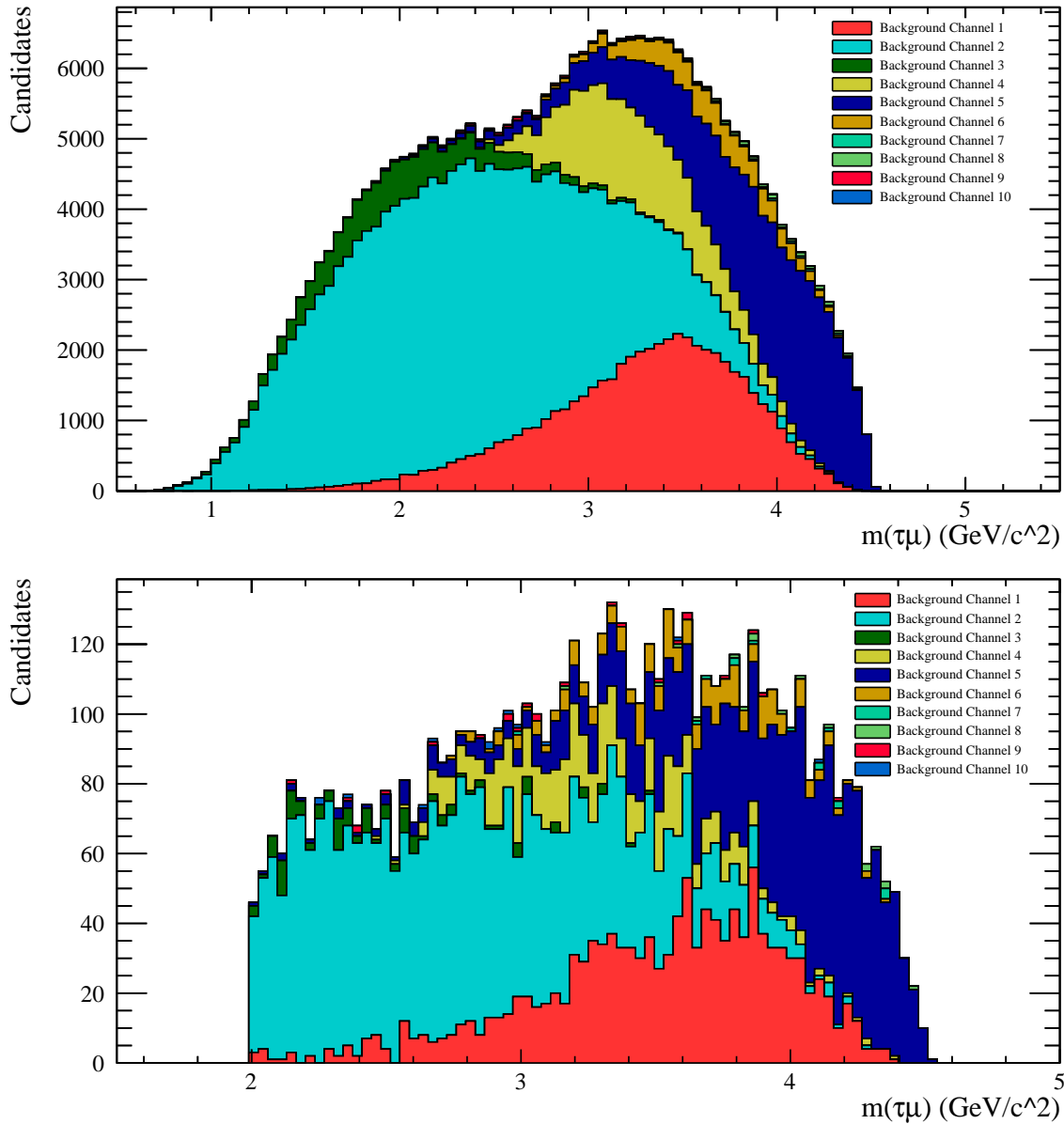
Figure 7.2: (Top) The invariant mass spectrum of the reconstructed $\tau - \mu$ signal, generated with RapidSim before (top) and after (bottom) applying the kinematic cuts. The decay channels corresponding to the numbers in the legend can be found in Table 6.1.

peak at the B-meson mass, which is due to the missing neutrino. This missing energy shifts the visible mass towards lower masses. In Figure 8.2 the results for the reconstructed mass are shown for both the plus and the minus solution and for both magnet polarities, again for the 2018 MC data. The mass peak is clearly shifted towards the B-meson mass. The results of the reconstruction for the 2017 Monte Carlo data can be found in Appendix B.

During the reconstruction of the neutrino momentum, the quadratic formula is applied to find the plus and minus solution for the momentum. However, one requirement when using this formula is that the discriminant is positive. For a fraction of the events the discriminant
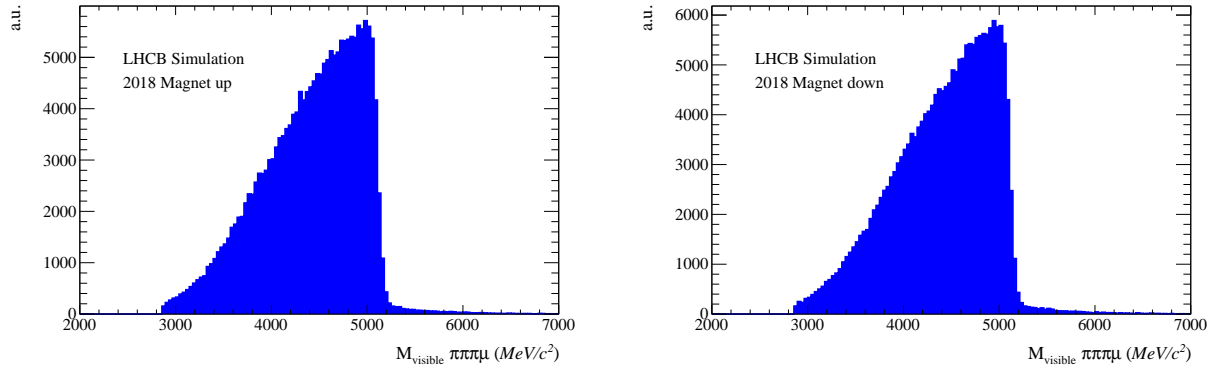
Figure 7.3: The visible B-meson mass of the 2018 $B_{(s)} \to \tau\mu$ Monte Carlo sample for positive magnet polarity (left) and negative magnet polarity (right). The visible mass distribution does not peak at the B-meson mass, as is expected due to the missing neutrino.
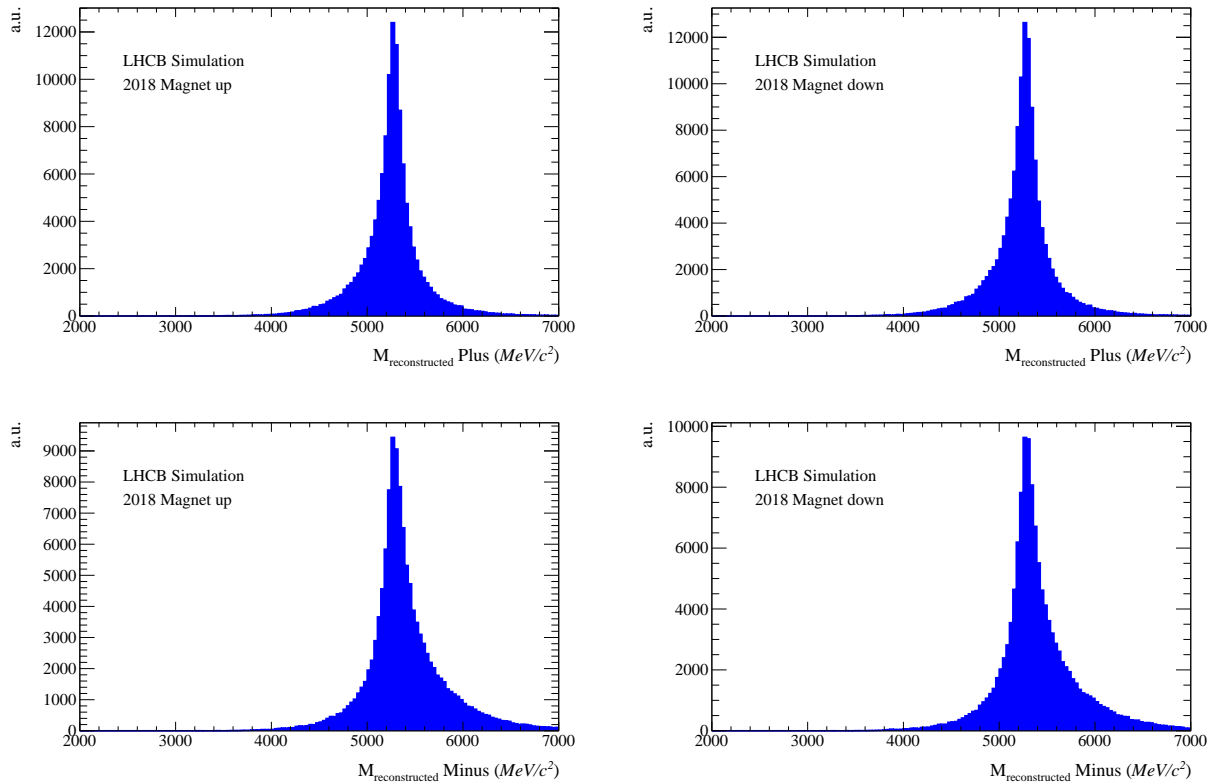

Figure 7.4: The reconstructed B-meson mass of the 2018 $B_{(s)} \to \tau\mu$ Monte Carlo sample for positive magnet polarity (left) and negative magnet polarity (right). The figures on the top show the plus solution for the neutrino momentum reconstruction and the figures on the bottom show the minus solution.
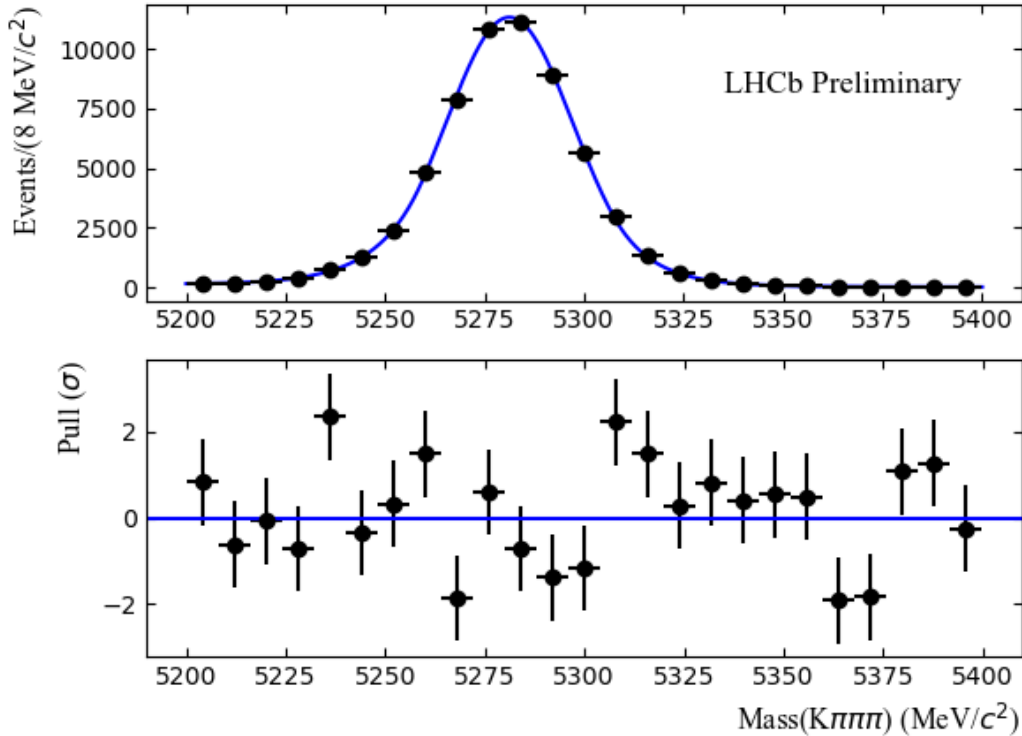
Figure 7.5: $B^0 \to D^-(\to K^+\pi^-\pi^-)\pi^+$ 2018 Monte Carlo invariant mass fit using a DSCB PDF.

is calculated to be negative, preventing the reconstruction of the neutrino momentum. The reconstruction efficiencies, i.e. the percentage of events with a positive discriminant, are calculated to be $(65.9 \pm 0.4)\%$ for the 2018 magnet up sample and $(65.8 \pm 0.4)\%$ for the 2018 magnet down sample. For the 2017 Monte Carlo sample the reconstruction efficiencies are $(66.1 \pm 0.3)\%$ for the magnet up sample and $(65.9 \pm 0.3)\%$ for the magnet down sample.

7.4 Invariant mass fit of normalisation channel MC

An invariant mass fit was performed on the 2018 Monte-Carlo signal sample of the normalisation channel $B^0 \to D^-(\to K^+\pi^-\pi^-)\pi^+$ using zfit. At first the selection criteria from Table 6.3 and Table 6.4 are applied to the full sample. Then the signal is fitted to a double sided crystal ball PDF. The equation for the DSCB can be found in Eq. 6.12. The results of this fit are presented in Fig. 7.5 and the fitted values of the DSCB parameters can be found in Table 7.2. As can be seen from Fig. 7.5 the invariant mass distribution is well described by the DSCB in blue. The largest pull from the fit is around 2σ and it fluctuates around 0, indicating that the DSCB PDF describes the invariant mass shape well.

Table 7.2: The results for the DSCB parameters from the invariant mass fit of the normalisation channel 2018 MC sample.

Parameter	Value
N	60100 ± 245
μ	5281.00 ± 0.08
σ	15.95 ± 0.10
α_L	1.382 ± 0.040
n_L	143.2 ± 453.8
α_R	1.626 ± 0.042
n_R	153.5 ± 217.5

7.5   Discussion

The trigger lines for both $B_{(s)} \to \tau\mu$ and $B_{(s)} \to \tau e$ have been incorporated in the LHCb software and will gather data for future searches in Run 3. Although it would have been possible to further fine tune the selection criteria used in the trigger lines, time was a limiting factor since the trigger lines had to be ready in time to be used in Run 3. In addition, the selection criteria of the lines were chosen to be similar to the criteria used in other rare decay trigger lines, so deviating too much from these criteria would not have been possible.
At the moment of writing this thesis the analysis of the search for $B_{(s)} \to \tau\mu$ in Run 2 is still ongoing. Parts of the analysis have been prepared and performed, as presented in the sections above. However, some of these steps can still be improved upon. The offline selection criteria applied to the normalisation channel were not determined ourselves, but taken from the previous analysis. Improvements could be made by studying and optimising these selection criteria, since the optimal cuts might differ between Run 1 and Run 2 data.

The main limitation for us in this analysis was time. The entire analysis had to be built up from scratch and all dedicated MC samples for both signal and background had to be requested from the collaboration. The only MC sample readily available was the normalisation channel MC. Nevertheless a good start was made and many of the main components, such as the invariant mass fit and B-mass reconstruction, have been written and are ready to be used in the analysis.

Chapter 8

Conclusion and outlook

In this chapter the main results of the research conducted in this thesis will be summarised, followed by some comments on potential future research that can be done based on this work. In both sections first the theoretical topics are covered, before discussing the experimental studies.

8.1   Conclusion

The 4321-model containing a vector leptoquark was explored, presenting the calculations of the massive gauge boson spectrum and the interaction Lagrangian in detail. This was followed by an overview of the flavour structure of the model. Finally the contributions of the 4321-model to the LFV $B_{(s)} \to \tau\mu$ decay are discussed. It was shown that the contribution of the vector leptoquark to the branching fraction of this decay is approximately $\mathcal{B} \approx (1.1 \pm 0.09) \times 10^{-6}$.

After these calculation a minimal solution to the flavour anomalies, consisting of the addition of a scalar leptoquark and a charged scalar to the SM, was considered. A χ^2-fit was performed on the couplings of these new scalar particles to the SM particles. It was found that if these particles are added to the SM the experimental data is described better than with solely the SM, with a difference of $\Delta\chi^2 = 68.88$. In addition the allowed parameter space of the model was studied within a certain fit quality. These results were also mapped back to the observables and compared to the SM and experimental values.

In preparation of future experimental searches for the $B_{(s)} \to (\tau \to \pi\pi\pi\nu_\tau)\mu$ decay with LHCb an HLT2 trigger line was written for Run 3. The efficiency of this trigger line is $3.4 \pm 0.2\%$ for a positive magnet polarity and $3.9 \pm 0.1\%$ for a negative magnet polarity. In addition an HLT2 trigger line for $B_{(s)} \to \tau e$ decays was written. Both lines have been incorporated into the LHCb software and will be used during Run 3 data taking.

A start was made with the search of $B_{(s)} \to \tau\mu$ in the Run 2 data. It is shown using RapidSim that partially reconstructed Λ_b decays pose no threat as potential background sources. In addition the analytic reconstruction of the neutrino momentum is performed an applied to the 2017 and 2018 $B_{(s)} \to \tau\mu$ Monte Carlo sample. This reconstruction can performed with an efficiency of $(65.9 \pm 0.4)\%$ for the 2018 magnet up sample and $(65.8 \pm 0.4)\%$ for the 2018

magnet down sample. For the 2017 Monte Carlo sample the reconstruction efficiencies are $(66.1\pm0.3)\%$ for the magnet up sample and $(65.9\pm0.3)\%$ for the magnet down sample. Finally the invariant mass distribution of the normalisation channel $B^0 \to D^-(\to K^+\pi^-\pi^-)\pi^+$ 2018 Monte Carlo is fitted using zfit.

8.2 Outlook

One of the next steps on the theory side, if one were to continue the work done in this thesis, would be to further deepen our understanding of the 4321-model. Understanding the flavour structure of the model and its implications on the $B_{(s)} \to \tau\mu$ decay will prove insightful. If the model is better understood one could also see if there are adaptions one could make to the model in order to find contributions to more of the flavour anomalies. Another interesting analysis would be to perform a similar study as presented in Chapter 3, but using the 4321-model instead of this minimal model. This would require to calculate the contributions of the 4321-model components to desired observables in terms of the model parameters. Once this is done the framework of the analysis presented in this thesis can be used to perform the analysis.

On the experimental side it is more clear what the next step would be: continue the analysis. There is still a lot of work that needs to be done before the analysis of Run 2 data is complete, like the background rejection with BDTs or a similar ML technique and the final fit of the invariant mass distribution. With the Run 2 analysis the limit on the branching fraction of $B_{(s)} \to \tau\mu$ can be tightened further, which in turn helps constrain potential BSM theories. In addition there is also a future for this analysis, and potentially the search for $B_{(s)} \to \tau e$, in Run 3 thanks to the HLT2 trigger lines that have been written. These trigger lines will increase the number of event candidates that the LHCb experiment will gather, allowing us to keep on tightening the limit on the branching fraction or even allowing us to observe one of the decays.

The field of flavour physics in general is an exciting field to be working in currently. The hints of new physics seen in the flavour anomalies will, hopefully, transform into clear signs of NP with the new data runs of the LHC experiments and also Belle II. The possibility still exists that the flavour anomalies are due to statistical fluctuations and the new signs of physics will disappear. Nevertheless, whatever future results will be, studies of BSM models and searches for LFV decays like $B_{(s)} \to \tau\mu$ will aid in the understanding of the world of physics and that in itself makes it important to continue research in these fields.

Bibliography

[1] **ATLAS** collaboration, G. Aad et Al.. "Observation of a new particle in the search for the Standard Model Higgs boson with the ATLAS detector at the LHC". In: *Phys. Lett. B* **716** (2012). DOI: https://doi.org/10.1016/j.physletb.2012.08.020.

[2] **CMS** collaboration, S. Chatrchyan et Al.. "Observation of a new boson at a mass of 125 GeV with the CMS experiment at the LHC". In: *Phys. Lett. B* **716** (2012). DOI: https://doi.org/10.1016/j.physletb.2012.08.021. URL: https://www.sciencedirect.com/science/article/pii/S0370269312008581.

[3] P.W. Higgs. "Broken Symmetries, Massless Particles and Gauge Fields". In: *Phys. Rev. Lett.* **16** (1964).

[4] F. Englert and R. Brout. "Broken Symmetry and the Mass of Gauge Vector Mesons". In: *Phys. Rev. Lett.* **17** (1964).

[5] The Super-Kamiokande collaboration, Y. Fukuda et Al.. "Measurement of the Flux and Zenith-Angle Distribution of Upward Throughgoing Muons by Super-Kamiokande". In: *Phys. Rev. Lett.* **82** (1999). DOI: 10.1103/PhysRevLett.82.2644.

[6] B. Abi et Al. "Measurement of the Positive Muon Anomalous Magnetic Moment to 0.46 ppm". In: *Phys. Rev. Lett.* **126** (14 Apr. 2021), p. 141801. DOI: 10.1103/PhysRevLett.126.141801. URL: https://link.aps.org/doi/10.1103/PhysRevLett.126.141801.

[7] T. Aoyama et Al. "The anomalous magnetic moment of the muon in the Standard Model". In: *Physics Reports* **887** (2020). The anomalous magnetic moment of the muon in the Standard Model, pp. 1–166. ISSN: 0370-1573. DOI: https://doi.org/10.1016/j.physrep.2020.07.006. URL: https://www.sciencedirect.com/science/article/pii/S0370157320302556.

[8] **LHCb** collaboration, R. Aaij et Al.. "Test of lepton universality in $B^0 \to K^{*0}\ell^+\ell^-$ decays". In: *JHEP* **55** (2017). DOI: 10.1007/JHEP08(2017)055.

[9] **LHCb** collaboration, R. Aaij et Al.. "Test of lepton universality in beauty-quark decays". In: *Nat. Phys* **18** (2022). DOI: 10.1038/s41567-021-01478-8.

[10] **HFLAV**, Y. S. Amhis et Al.. "Averages of b-hadron, c-hadron, and τ-lepton properties as of 2018". In: *Eur. Phys. J C* **81**.3 (Mar. 2021). DOI: 10.1140/epjc/s10052-020-8156-7. URL: https://doi.org/10.1140/epjc/s10052-020-8156-7.

[11] **LHCb** collaboration, R. Aaij et Al.. "Angular analysis of the $B^0 \to K^{*0}\mu^+\mu^-$ using 3 fb1 of integrated luminosity". In: *JHEP* **104** (2016). DOI: 10.1007/JHEP02(2016)104.

BIBLIOGRAPHY

[12] N. B. Beaudry et Al.. "The $B \to K\pi$ puzzle revisited". In: *JHEP* **74** (2018). DOI: 10.1007/JHEP01(2018)074.

[13] M. Mühlleitner, M.O.P. Sampaio, R. Santos and J. Wittbrodt. "Phenomenological comparison of models with extended Higgs sectors". In: *JHEP* **132** (2017). DOI: 10.1007/JHEP08(2017)132.

[14] I. Dorsner et Al.. "Physics of leptoquarks in precision experiments and at particle colliders". In: *Physics Reports* **641** (2016). DOI: 10.1016/j.physrep.2016.06.001.

[15] L. Di Luzio, A. Greljo and M. Nardecchia. "Gauge leptoquark as the origin of B-physics anomalies". In: *Phys. Rev. D* **96** (11 Dec. 2017). DOI: https://doi.org/10.1103/PhysRevD.96.115011.

[16] D. Marzocca and S. Trifinopoulos. "A Minimal Explanation of Flavour Anomalies: B-Meson Decays Muon Magnetic Moment and the Cabibbo Angle". In: (Apr. 2021). DOI: 10.1103/PhysRevLett.127.061803. URL: http://arxiv.org/abs/2104.05730.

[17] S. Chib and E. Greenberg. "Understanding the Metropolis-Hastings Algorithm". In: *The American Statistician* **49**.4 (1995), pp. 327–335. ISSN: 00031305. DOI: 10.2307/2684568. URL: http://www.jstor.org/stable/2684568.

[18] **LHCb** collaboration, A Augusto Alves Jr et Al.. "The LHCb detector at the LHC". In: *JINST* **3** (2008). DOI: 10.1088/1748-0221/3/08/s08005. URL: https://doi.org/10.1088/1748-0221/3/08/s08005.

[19] L. Calibbi and G. Signorelli. "Charged lepton flavour violation: An experimental and theoretical introduction". In: *Riv. Nuovo Cimento* **71** (2018). DOI: 10.1393/ncr/i2018-10144-0.

[20] C. Cornella, J. Fuentes-Martín and G. Isidori. "Revisiting the vector leptoquark explanation of the B-physics anomalies". In: *JHEP* **168** (2019). DOI: 10.1007/JHEP07(2019)168.

[21] A.D. Smirnov. "Vector leptoquark mass limits and branching ratios of $K_L^0, B^0, B_s \to \ell_i^+ \ell_j^-$ decays with account of fermion mixing in leptoquark currents". In: *Mod. Phys. Lett. A* **33** (2018). DOI: 10.1142/S0217732318500190.

[22] **LHCb** collaboration, R. Aaij et Al.. "Search for the Lepton-Flavor-Violating Decays $B_S^0 \to \tau^\pm \mu^\mp$ and $B^0 \to \tau^\pm \mu^\mp$". In: *Phys. Rev. Lett.* **123** (2019). DOI: 10.1103/PhysRevLett.123.211801. URL: https://doi.org/10.1103/PhysRevLett.123.211801.

[23] D. Griffiths. *Introduction to Elementary Particles*. Second, Revised Edition. Wiley-VCH, 2008.

[24] Wikipedia. URL: https://en.wikipedia.org/wiki/Quark#/media/File:Standard_Model_of_Elementary_Particles.svg.

[25] M. D. Schwartz. *Quantum Field Theory and the Standard Model*. First Edition. Cambridge University Press, 2014.

[26] M. Thomson. *Modern Particle Physics*. First Edition. Cambridge University Press, 2013.

[27] S. Weinberg. "Baryon and Lepton Nonconserving Processes". In: *Phys. Rev. Lett.* 43 (1979). DOI: 10.1103/PhysRevLett.43.1566.

[28] R. Alonse, E.E. Jenskins, A.V. Manohar and M. Trott . "Renormalization Group Evolution of the Standard Model Dimension Six Operators III: Gauge Coupling Dependence and Phenomenology". In: *JHEP* **159** (2014). DOI: 10.1007/JHEP04(2014)159.

[29] S. Descotes-Genon, T. Hurth, J. Matias and J. Virto. "Optimising the basis of $B^0 \to K^{*0}\ell^+\ell^-$ observables in the full kinematic range". In: *JHEP* **137** (2013). DOI: 10.1007/JHEP05(2013)137.

[30] **BABAR** collaboration, J.P. Lees et Al.. "Evidence for an Excess of $\bar{B} \to D^{(*)}\tau^-\bar{\nu}_\tau$ decays". In: *Phys. Rev. Lett.* **109** (2012). DOI: 10.1103/PhysRevLett.109.101802.

[31] **Belle** collaboration, G. Caria et Al.. "Measurement of $\mathcal{R}(D)$ and $\mathcal{R}(D^*)$ with a Semileptonic Tagging Method". In: *Phys. Rev. Lett.* **124** (2020). DOI: 10.1103/PhysRevLett.124.161803.

[32] **LHCb** collaboration, R. Aaij et Al.. "Test of lepton flavor universality by the measurement of the $B^0 \to D^{*-}\tau^+\nu_\tau$ using branching fraction using three-prong τ decays". In: *Phys. Rev. D* **197** (2018). DOI: 10.1103/PhysRevD.97.072013.

[33] Muon g-2 collaboration, G.W. Bennet et Al.. "Final report of the E821 muon anomalous magnetic moment measurement at BNL". In: *Phys. Rev. D* **73** (2006). DOI: 10.1103/PhysRevD.73.072003.

[34] C. Csaki. "The minimal supersymmetric standard model". In: *Modern Physics Letters A* **11**.08 (Mar. 1996). DOI: 10.1142/s021773239600062x.

[35] I. P. Ivanov. "Building and testing models with extended Higgs sectors". In: *Prog. Part. Nucl. Phys.* **95** (2017). DOI: 10.1016/j.ppnp.2017.03.001.

[36] A. Crivellin et Al.. "Lepton flavour violating B decays in Z' models." In: *Phys. Rev. D* **92** (2015). DOI: 10.1103/PhysRevD.92.054013.

[37] E.H. Simmons et Al.. "Coloron Models and LHC Phenomenology." In: *SCGT12* (2014). DOI: 10.1142/9789814566254_0014.

[38] J.C. Pati and A. Salam. "Lepton number as the fourth color." In: *Phys. Rev. D* **10** (1974). DOI: 10.1103/PhysRevD.11.703.2.

[39] B. Gripaios, M Nardecchia and S.A. Renner. "Composite leptoquarks and anomalies in B-meson decays". In: *JHEP* **6** (2015). DOI: 10.1007/JHEP05(2015)006.

[40] L. Di Luzio et Al.. "Maximal flavour violation: a Cabibbo mechanism for leptoquarks". In: *JHEP* **2018** (2018). DOI: https://doi-org.proxy.library.uu.nl/10.1007/JHEP11(2018)081.

[41] Wolfram Research Inc. *Mathematica, Version 12.3.1.0*. Champaign, IL, 2021. URL: https://www.wolfram.com/mathematica.

[42] V. Gherardi, D. Müller and E. Venturini. "Low-energy phenomenology of scalar leptoquarks at one-loop accuracy". In: *JHEP* **138** (2021). DOI: https://doi.org/10.1007/JHEP01(2021)138.

[43] A. Crivellin et Al. "Searching for lepton flavor universality violation and collider signals from a singly charged scalar singlet". In: *Phys. Rev. D* **103** (7 Apr. 2021), p. 073002. DOI: 10.1103/PhysRevD.103.073002. URL: https://link.aps.org/doi/10.1103/PhysRevD.103.073002.

[44] **Belle** collaboration, R. Glattauer et Al.. "Measurement of the decay $B \to Dl\nu$ in fully reconstructed events and determination of the Cabibbo-Kobayashi-Maskawa matrix element $|V_{cb}|$". In: **93**.3 (Feb. 2016). DOI: 10.1103/physrevd.93.032006. URL: https://doi.org/10.11032Fphysrevd.93.032006.

[45] Particle Data Group, P.A. Zyla et Al.. "Review of Particle Physics". In: *PTEP* 2020.8 (2020). and 2021 update. DOI: 10.1093/ptep/ptaa104.

[46] **UTfit** collaboration, M. Bona et Al.. "Model-independent constraints on $\Delta F = 2$ operators and the scale of new physics". In: *Journal of High Energy Physics* 03 (Mar. 2008). DOI: 10.1088/1126-6708/2008/03/049. URL: https://doi.org/10.1088/1126-6708/2008/03/049.

[47] **ALEPH & DELPHI & L3 & OPAL & SLD** Collaborations, the LEP Electroweak Working Gr "Precision electroweak measurements on the Z resonance". In: *Physics Reports* **427**.5 (2006), pp. 257–454. ISSN: 0370-1573. DOI: https://doi.org/10.1016/j.physrep.2005.12.006. URL: https://www.sciencedirect.com/science/article/pii/S0370157305005119.

[48] **Belle** collaboration, J. Grygier et Al.. "Search for $B \to h\nu\overline{\nu}$ decays with semileptonic tagging at Belle". In: *Phys. Rev. D* **96** (9 Nov. 2017). DOI: 10.1103/PhysRevD.96.091101. URL: https://link.aps.org/doi/10.1103/PhysRevD.96.091101.

[49] A. G. Akeroyd and Chuan-Hung Chen. "Constraint on the branching ratio of $B_c^- \to \tau\overline{\nu}$ from LEP1 data and consequences for $R(D^{(*)})$ anomaly". In: *Phys. Rev. D* **96** (7 Oct. 2017). DOI: 10.1103/PhysRevD.96.075011. URL: https://link.aps.org/doi/10.1103/PhysRevD.96.075011.

[50] Y. H. Ahn, Hai-Yang Cheng, and Sechul Oh. "Wolfenstein Parametrization at Higher Order: Seeming Discrepancies and Their Resolution". In: *Physics Letters B* **703**.5 (June 2011), pp. 571–575. DOI: 10.1016/j.physletb.2011.08.047. URL: http://arxiv.org/abs/1106.0935.

[51] M. Bauer and Ma. Neubert. "Minimal Leptoquark Explanation for the $R_{D^{(*)}}$ R_K and $(g-2)_\mu$ Anomalies". In: *Physical Review Letters* **116** (14 Apr. 2016). DOI: 10.1103/PhysRevLett.116.141802.

[52] Lyndon Evans and Philip Bryant. "LHC Machine". In: *JINST* **3** (2008). DOI: 10.1088/1748-0221/3/08/s08001. URL: https://doi.org/10.1088/1748-0221/3/08/s08001.

[53] C. Lefèvre. *CERN accelerator complex.* 2008. URL: https://cds.cern.ch/record/1260465.

[54] **ATLAS** collaboration, G. Aad et Al.. "The ATLAS Experiment at the CERN Large Hadron Collider". In: *JINST* **3**.08 (Aug. 2008). DOI: 10.1088/1748-0221/3/08/s08003.

[55] **CMS** collaboration, S. Chatrchyan et Al.. "The CMS Experiment at the CERN LHC". In: *JINST* **3**.08 (Aug. 2008). DOI: 10.1088/1748-0221/3/08/S08004.

[56] **ALICE** collaboration, K. Aamodt et Al.. "The ALICE Experiment at the CERN LHC". In: *JINST* **3**.08 (Aug. 2008). DOI: 10.1088/1748-0221/3/08/S08002.

[57] **LHCb** collaboration, R. Aaij et Al.. "Performance of the LHCb Vertex Locator". In: *JINST* **9** (2014). DOI: 10.1088/1748-0221/9/09/P09007. URL: https://doi.org/10.1088/1748-0221/9/09/P09007.

[58] G.A. Cowen. "Performance of the LHCb Silicon Tracker". In: *Nuclear Instruments and Methods in Physics Research Section A* **699** (2013), pp. 156–159. DOI: https://doi.org/10.1016/j.nima.2012.05.074. URL: https://www.sciencedirect.com/science/article/pii/S0168900212005876.

[59] **LHCb** collaboration, A Augusto Alves Jr et Al.. "Performance of the LHCb Outer Tracker". In: *JINST* **9** (2014). DOI: 10.1088/1748-0221/9/01/P01002. URL: https://doi.org/10.1088/1748-0221/9/01/P01002.

[60] **LHCb** RICH collaboration, M. Adinolfi et Al.. "Performance of the LHCb RICH detector at the LHC". In: *Eur. Phys. J. C* **73** (2013). DOI: 10.1140/epjc/s10052-013-2431-9. URL: https://doi.org/10.1140/epjc/s10052-013-2431-9.

[61] **LHCb** calorimeter group, C. A. Beteta et Al.. "Calibration and Performance of the LHCb calorimeters in Run 1 and 2 at the LHC". In: (Aug. 2020). arXiv: 2008.11556 [physics.ins-det].

[62] **LHCb** collaboration, A Augusto Alves Jr et Al.. "Performance of the LHCb muon system". In: *JINST* **8** (2013). DOI: 10.1088/1748-0221/8/02/P02022. URL: https://doi.org/10.1088/1748-0221/8/02/P02022.

[63] A. Piucci. "The LHCb Upgrade". In: *Journal of Physics: Conference Series* **878** (2017), p. 012012. DOI: 10.1088/1742-6596/878/1/012012. URL: https://doi.org/10.1088/1742-6596/878/1/012012.

[64] **LHCb** collaboration, Bediaga, I. et Al.. "Framework TDR for the LHCb Upgrade: Technical Design Report". In: (Apr. 2012).

[65] LHCb Collaboration. *LHCb VELO Upgrade Technical Design Report*. Tech. rep. Nov. 2013. URL: https://cds.cern.ch/record/1624070.

[66] LHCb Collaboration. *LHCb Tracker Upgrade Technical Design Report*. Tech. rep. Feb. 2014. URL: https://cds.cern.ch/record/1647400.

[67] LHCb Collaboration. *LHCb PID Upgrade Technical Design Report*. Tech. rep. Nov. 2013. URL: https://cds.cern.ch/record/1624074.

[68] R Aaij et Al. "The LHCb trigger and its performance in 2011". In: *Journal of Instrumentation* **8**.04 (Apr. 2013). DOI: 10.1088/1748-0221/8/04/p04022. URL: https://doi.org/10.1088/1748-0221/8/04/p04022.

[69] R. Aaij et Al. "Design and performance of the LHCb trigger and full real-time reconstruction in Run 2 of the LHC". In: *Journal of Instrumentation* 14.04 (Apr. 2019). DOI: 10.1088/1748-0221/14/04/p04013. URL: https://doi.org/10.1088/1748-0221/14/04/p04013.

[70]   *Trigger Schemes.* URL: http://lhcb.web.cern.ch/lhcb/speakersbureau/html/TriggerScheme.html.

[71]   LHCb Collaboration. *LHCb Trigger and Online Upgrade Technical Design Report.* Tech. rep. May 2014. URL: https://cds.cern.ch/record/1701361.

[72]   R. Aaij et Al. "A Comparison of CPU and GPU Implementations for the LHCb Experiment Run 3 Trigger." In: *Comput Softw Big Sci* **6**.1 (2021). DOI: 10.1007/s41781-021-00070-2. URL: https://doi.org/10.1007/s41781-021-00070-2.

[73]   R. Aaij et Al. "Allen: A High-Level Trigger on GPUs for LHCb." In: *Comput Softw Big Sci* **4**.7 (2020). DOI: 10.1007/s41781-020-00039-7. URL: https://doi.org/10.1007/s41781-020-00039-7.

[74]   Particle Data Group, R.L. Workman et Al.. "Review of Particle Physics". In: *PTEP* 2022 (2022), p. 083C01. DOI: 10.1093/ptep/ptac097.

[75]   S. Aiola et Al. "Hybrid seeding: A standalone track reconstruction algorithm for scintillating fibre tracker at LHCb." In: *Comput. Phys. Commun.* **260** (2021). DOI: 10.1016/j.cpc.2020.107713.

[76]   **LHCb** collaboration. URL: https://lhcbdoc.web.cern.ch/lhcbdoc/moore/.

[77]   L. Breiman. *Classification And Regression Trees.* First Edition. Wadsworth international group, 1984.

[78]   A.L. Read. "Presentation of search results: the CL_s technique." In: *J. Phys. G: Nucl. Part. Phys.* **28** (2002). DOI: 10.1088/0954-3899/28/10/313.

[79]   D.C. Craik G.A. Cowan and M.D. Needham. "RapidSim: An application for the fast simulation of heavy-quark hadron decays". In: *Computer Physics Communications* 214 (2017). DOI: https://doi.org/10.1016/j.cpc.2017.01.029. URL: https://www.sciencedirect.com/science/article/pii/S0010465517300413.

[80]   Rene Brun and Fons Rademakers. "ROOT — An object oriented data analysis framework". In: *Nucl. Inst. Meth.* A389.1 (1997). DOI: https://doi.org/10.1016/S0168-9002(97)00048-X. URL: https://www.sciencedirect.com/science/article/pii/S016890029700048X.

[81]   Matteo Cacciari, Mario Greco, and Paolo Nason. "The p_T spectrum in heavy-flavour hadroproduction". In: *Journal of High Energy Physics* 1998.05 (May 1998). DOI: 10.1088/1126-6708/1998/05/007. URL: https://doi.org/10.1088/1126-6708/1998/05/007.

[82]   J. Eschle Read. "zfit: Scalable pythonic fitting". In: *SoftwareX* 11 (2020). DOI: https://doi.org/10.1016/j.softx.2020.100508.

[83]   CERN. URL: https://root.cern/topical/#roofit.

Appendix A: $SU(4)$ generators

The generators of the $SU(4)$ group in the fundamental representation:

$$T^1 = \frac{1}{2}\begin{pmatrix} 0 & 1 & 0 & 0 \\ 1 & 0 & 0 & 0 \\ 0 & 0 & 0 & 0 \\ 0 & 0 & 0 & 0 \end{pmatrix} \quad T^2 = \frac{1}{2}\begin{pmatrix} 0 & -i & 0 & 0 \\ i & 0 & 0 & 0 \\ 0 & 0 & 0 & 0 \\ 0 & 0 & 0 & 0 \end{pmatrix} \quad T^3 = \frac{1}{2}\begin{pmatrix} 1 & 0 & 0 & 0 \\ 0 & -1 & 0 & 0 \\ 0 & 0 & 0 & 0 \\ 0 & 0 & 0 & 0 \end{pmatrix}$$

$$T^4 = \frac{1}{2}\begin{pmatrix} 0 & 0 & 1 & 0 \\ 0 & 0 & 0 & 0 \\ 1 & 0 & 0 & 0 \\ 0 & 0 & 0 & 0 \end{pmatrix} \quad T^5 = \frac{1}{2}\begin{pmatrix} 0 & 0 & -i & 0 \\ 0 & 0 & 0 & 0 \\ i & 0 & 0 & 0 \\ 0 & 0 & 0 & 0 \end{pmatrix} \quad T^6 = \frac{1}{2}\begin{pmatrix} 0 & 0 & 0 & 0 \\ 0 & 0 & 1 & 0 \\ 0 & 1 & 0 & 0 \\ 0 & 0 & 0 & 0 \end{pmatrix}$$

$$T^7 = \frac{1}{2}\begin{pmatrix} 0 & 0 & 0 & 0 \\ 0 & 0 & -i & 0 \\ 0 & i & 0 & 0 \\ 0 & 0 & 0 & 0 \end{pmatrix} \quad T^8 = \frac{1}{2\sqrt{3}}\begin{pmatrix} 1 & 0 & 0 & 0 \\ 0 & 1 & 0 & 0 \\ 0 & 0 & -2 & 0 \\ 0 & 0 & 0 & 0 \end{pmatrix} \quad T^9 = \frac{1}{2}\begin{pmatrix} 0 & 0 & 0 & 1 \\ 0 & 0 & 0 & 0 \\ 0 & 0 & 0 & 0 \\ 1 & 0 & 0 & 0 \end{pmatrix}$$

$$T^{10} = \frac{1}{2}\begin{pmatrix} 0 & 0 & 0 & -i \\ 0 & 0 & 0 & 0 \\ 0 & 0 & 0 & 0 \\ i & 0 & 0 & 0 \end{pmatrix} \quad T^{11} = \frac{1}{2}\begin{pmatrix} 0 & 0 & 0 & 0 \\ 0 & 0 & 0 & 1 \\ 0 & 0 & 0 & 0 \\ 0 & 1 & 0 & 0 \end{pmatrix} \quad T^{12} = \frac{1}{2}\begin{pmatrix} 0 & 0 & 0 & 0 \\ 0 & 0 & 0 & -i \\ 0 & 0 & 0 & 0 \\ 0 & i & 0 & 0 \end{pmatrix}$$

$$T^{13} = \frac{1}{2}\begin{pmatrix} 0 & 0 & 0 & 0 \\ 0 & 0 & 0 & 0 \\ 0 & 0 & 0 & 1 \\ 0 & 0 & 1 & 0 \end{pmatrix} \quad T^{14} = \frac{1}{2}\begin{pmatrix} 0 & 0 & 0 & 0 \\ 0 & 0 & 0 & 0 \\ 0 & 0 & 0 & -i \\ 0 & 0 & i & 0 \end{pmatrix} \quad T^{15} = \frac{1}{2\sqrt{6}}\begin{pmatrix} 1 & 0 & 0 & 0 \\ 0 & 1 & 0 & 0 \\ 0 & 0 & 1 & 0 \\ 0 & 0 & 0 & -3 \end{pmatrix}$$

Appendix B: Analytic B-mass reconstruction

In this appendix the results of the analytic B-mass reconstruction for the 2017 $B_{(s)} \to \tau\mu$ Monte Carlo sample are presented. The reconstruction efficiency is $(66.1 \pm 0.3)\%$ for the magnet up sample and $(65.9 \pm 0.3)\%$ for the magnet down sample.
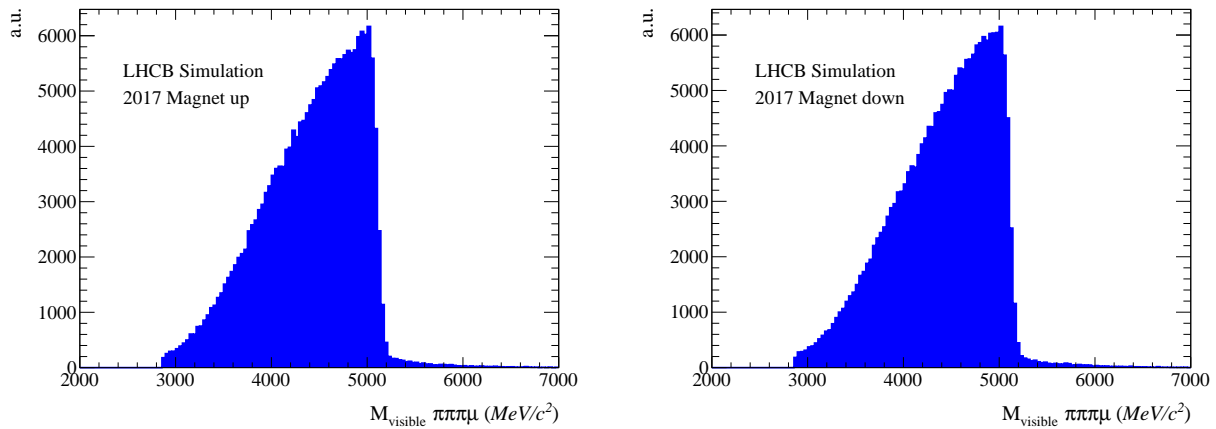

Figure 8.1: The visible B-meson mass of the 2017 $B_{(s)} \to \tau\mu$ Monte Carlo sample for positive magnet polarity (left) and negative magnet polarity (right). The visible mass distribution does not peak at the B-meson mass, as is expected due to the missing neutrino.
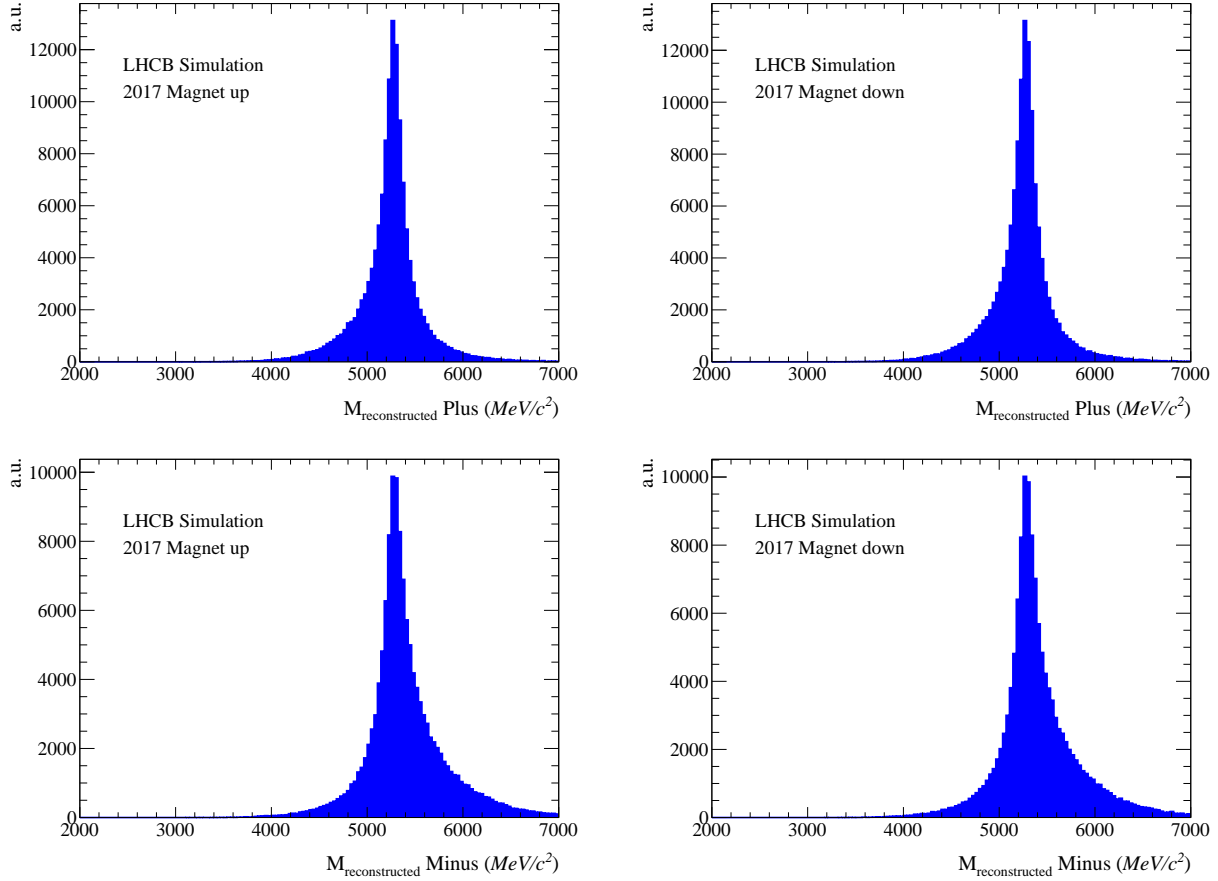
Figure 8.2: The reconstructed B-meson mass of the 2017 $B_{(s)} \to \tau\mu$ Monte Carlo sample for positive magnet polarity (left) and negative magnet polarity (right). The figures on the top show the plus solution for the neutrino momentum reconstruction and the figures on the bottom show the minus solution.

Acknowledgements

Samenvatting voor niet natuurkundigen

Alles om ons heen bestaat uit hele kleine deeltjes genaamd atomen. Van de tafel waar je aan zit tot de lucht om je heen. Deze atomen kunnen aan elkaar gekoppeld worden tot moleculen, die samen grote en complexe structuren kunnen vormen: vloeistoffen, kristallen, eiwitten, cellen, bomen, dieren en ga zo maar door. Uiteindelijk is alles om ons heen te herleiden tot deze atomen. Lange tijd werd gedacht dat deze atomen de aller kleinste deeltjes in de natuur waren, zogenaamde fundamentele deeltjes, die niet verder op te splitsen zijn. Aan het einde van de negentiende eeuw werd duidelijk dat dit niet het geval was met de ontdekking van het elektron: het eerste echte fundamentele deeltje. Een atoom bleek te bestaan uit een positief geladen atoomkern met negatief geladen elektronen daaromheen. Na deze ontdekking werd het langzaamaan, in de eerste helft van de twintigste eeuw, duidelijk hoe deze atomen in elkaar zaten. De positief geladen atoomkern bleek te bestaan uit positief geladen deeltjes, genaamd protonen, en elektrisch neutrale deeltjes, genaamd neutronen. Deze protonen en neutronen bleken op hun beurt uit nog kleinere deeltjes te bestaan, genaamd quarks. Deze quarks zijn, net als elektronen, fundamentele deeltjes.

Natuurkunde is de wetenschap die probeert de regels te ontdekken waar de niet-levende natuur zich aan houdt. Dit maakt natuurkunde een hele brede wetenschap die op te delen is in veel verschillende categoriën. Voorbeelden hiervan zijn onderzoek naar hoe zwaartekracht werkt of hoe een magneet werkt? Onderzoek naar het weer, waarom is de lucht blauw en radioactiviteit vallen onder de natuurkunde. De tak van natuurkunde waar deze scriptie binnen valt is de deeltjesfysica. In de deeltjesfysica proberen we het gedrag van fundamentele deeltjes, zoals quarks en elektronen, te beschrijven. Het blijkt dat we vrij goed in staat zijn dit gedrag te beschrijven. In de twintigste eeuw is hier veel onderzoek naar gedaan, met als resultaat het Standaard Model voor de deeltjesfysica (SM). Het Standaard Model is een van de meest succesvolle theoriën in de natuurkunde.

Het Standaard Model van de deeltjesfysica

Het Standaard Model beschrijft alle fundamentele deeltjes en hoe zij met elkaar praten, ookwel hun interacties genoemd. De deeltjes in het SM kunnen grofweg in tweeën worden opgedeeld: materie deeltjes en interactie deeltjes. Als twee deeltjes een interactie met elkaar aangaan gebeurt dit altijd via een ander fundamenteel deeltje. Er zijn drie soort interacties, of krachten, in het SM met ieder hun eigen krachtdragende deeltjes. De meest bekende is de elektro-magnetische kracht. Het krachtdragende deeltje voor de elektro-magnetische kracht

Standard Model of Elementary Particles

three generations of matter (fermions)			interactions / force carriers (bosons)	
I	II	III		
mass ≈2.2 MeV/c² charge ⅔ spin ½ **u** **up**	≈1.28 GeV/c² ⅔ ½ **c** **charm**	≈173.1 GeV/c² ⅔ ½ **t** **top**	0 0 1 **g** **gluon**	≈124.97 GeV/c² 0 0 **H** **higgs**
≈4.7 MeV/c² −⅓ ½ **d** **down**	≈96 MeV/c² −⅓ ½ **s** **strange**	≈4.18 GeV/c² −⅓ ½ **b** **bottom**	0 0 1 **γ** **photon**	
≈0.511 MeV/c² −1 ½ **e** **electron**	≈105.66 MeV/c² −1 ½ **μ** **muon**	≈1.7768 GeV/c² −1 ½ **τ** **tau**	≈91.19 GeV/c² 0 1 **Z** **Z boson**	
<1.0 eV/c² 0 ½ **νe** **electron neutrino**	<0.17 MeV/c² 0 ½ **νμ** **muon neutrino**	<18.2 MeV/c² 0 ½ **ντ** **tau neutrino**	≈80.39 GeV/c² ±1 1 **W** **W boson**	

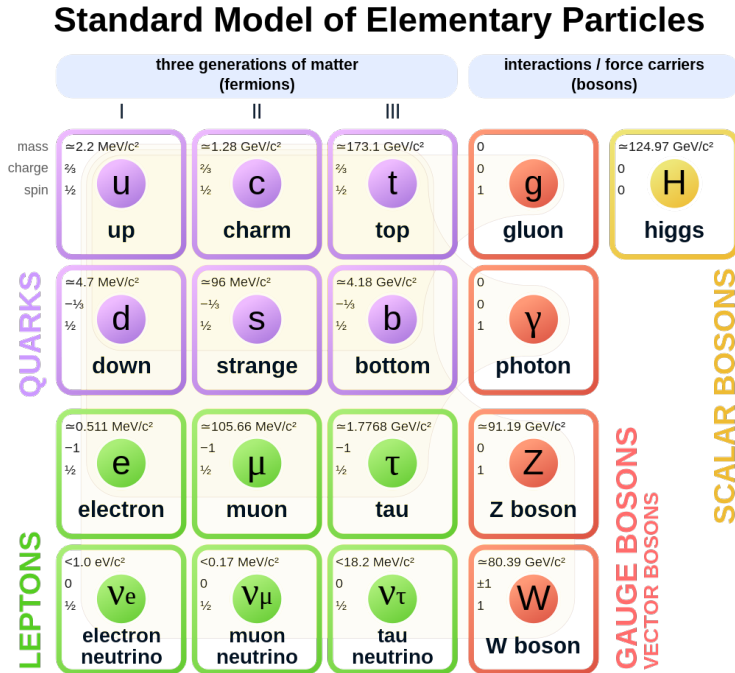QUARKS · LEPTONS · GAUGE BOSONS VECTOR BOSONS · SCALAR BOSONS

Figure 8.3: Alle fundamentele deeltjes in het Standaard Model van de deeltjesfysica.

is het foton, ook wel bekend als het licht-deeltje. Licht bestaat namelijk uit fotonen. De twee andere krachten in het SM zijn de zwakke wisselwerking en sterke wisselwerking. De zwakke wisselwerking wordt gedragen door twee W-bosonen, een is positief geladen en een is negatief geladen, en een Z-boson.[1] De sterke wisselwerking wordt gedragen door deeltjes die gluonen heten. Er is nog een vijfde krachtdragend deeltje in het SM, namelijk het Higgs deeltje. Dit is het deeltje wat massa geeft aan de materie deeltjes via het Higgs mechanisme.

Naast de krachtdragende deeltjes zijn er ook 12 soorten materie deeltjes. Deze 12 kunnen opgedeeld worden in 6 quarks en 6 leptonen. Elektronen vallen onder deze laatste categorie. Het elektron heeft ook nog twee zwaardere broertjes: het muon (μ) deeltje en het tau (τ) deeltje. Deze gedragen zich in het SM exact hetzelfde als het elektron, buiten dat ze zwaarder zijn. Naast het elektron, muon en tau zijn er ook nog drie neutrinos (ν). Dit zijn massaloze deeltjes die heel weinig interacties aangaan met de andere materie deeltjes, wat ze erg lastig te meten maakt. De andere 6 materie deeltjes zijn quarks. Er zijn drie quarks met een elektrische lading van $\frac{2}{3}$: de up-quark (u), charm-quark (c) en top-quark (t). De andere drie quarks, met een elektrische lading van $\frac{-1}{3}$, zijn de down-quark (d), strange-quark (s) en beauty-quark (b). Deze quarks kunnen gecombineerd worden om zogenaamde sub-atomaire deeltjes te vormen. Er bestaan twee type sub-atomaire deeltjes: baryonen en mesonen.

---

[1]Fundamentele deeltjes hebben een aantal eigenschappen waardoor we ze kunnen onderscheiden. Sommige van deze eigenschappen spreken redelijk voor zich, zoals massa en elektrische lading. Een wat minder duidelijke, maar daarom niet minder belangrijke, eigenschap is de spin van een deeltje. De spin van een deeltje kan gezien worden als een extra soort lading die een fundamenteel deeltje kan hebben. Heeft een deeltje een gehele spin, 0, 1, 2, etc, dan is het een boson, Heet het deeltje een halve spin, $\frac{1}{2}$, $\frac{3}{2}$, $\frac{5}{2}$, etc, dan is het een fermion.

Baryonen bestaan uit drie quarks en deze zijn we al eerder tegen gekomen. Zowel het proton als het neutron is namelijk een baryon. Mesonen zijn sub-atomaire deeltjes die uit twee quarks bestaan. In deze scriptie ligt de focus op B-mesonen. Dit zijn mesonen waar een van de twee quarks een beauty-quark is. Veel van deze baryonen en alle mesonen zijn instabiele deeltjes: na een bepaalde, hele korte tijd vervallen ze in andere subatomaire deeltjes. De enige stabiele deeltjes fundamentele deeltjes zijn elektronen en fotonen. Het enige stabiele sub-atomaire deeltje is het proton. Om de eigenschappen van deze deeltjes, en daarmee het SM, te kunnen testen, moeten ze eerst ergens geproduceerd worden en vervolgens ook nog gedetecteerd worden.Er zijn door de jaren heen veel experimentele opstellingen gebouwd om het SM te testen. De meest bekende van deze experimenten, die vandaag de dag nog in gebruik is, is de Large Hadron Collider bij CERN in Geneve.

De Large Hadron Collider en het LHCb experiment

De Large Hadron Collider (LHC) is een grote deeltjesversneller gebouwd onder de grond bij CERN in Geneve. De LHC bestaat uit een ring met een lengte van 27 kilometer waar in twee richtingen protonen versneld kunnen worden tot bijna de snelheid van het licht (300.000 kilometer per seconde). Op verschillende punten in deze ring kunnen deze protonen tot botsing gebracht worden. Bij deze botsingen ontstaat een grote hoeveelheid aan fundamentele en
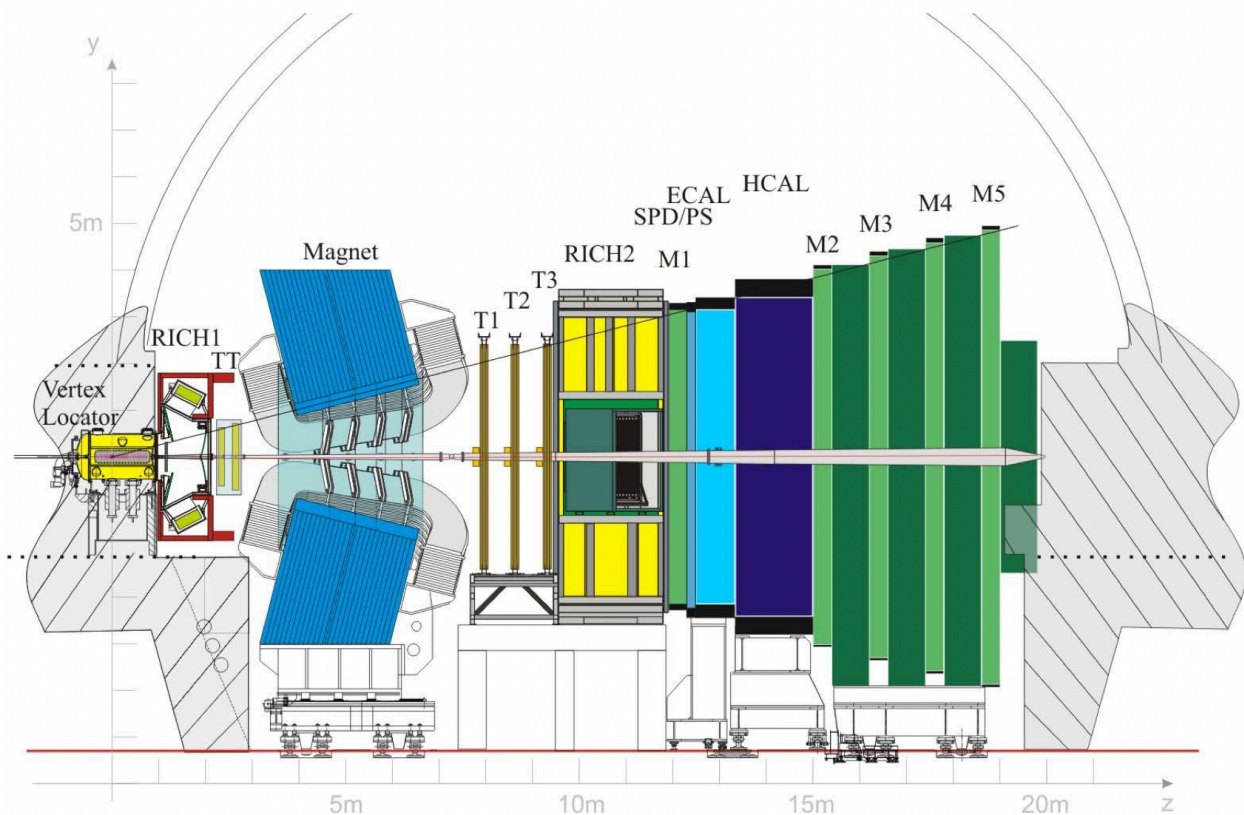

Figure 8.4: Een schematische weergave van de LHCb experiment, een van de vier grote experimenten bij de LHC.

sub-atomaire deeltjes, die op hun beurt weer vervallen naar uiteindelijk stabiele deeltjes. Op de plekken in de ring waar de protonen tot botsing gebracht worden zijn grote detectoren gebouwd die in staat zijn deze deeltjes te meten en daarmee de eigenschappen van het SM kunnen toetsen. Deze vier grote detectoren zijn ATLAS, CMS, ALICE en de LHCb detector. De LHCb detector, waarmee gewerkt is in deze scriptie, is speciaal ontworpen om de eigenschappen van sub-atomaire deeltjes te onderzoeken die een b-quark bevatten. Waar ATLAS, CMS en ALICE gebouwd zijn in de vorm van een vat rondom het botsingspunt is de LHCb detector aan een kant van het botsingspunt gebouwd. De reden hiervoor is dat de meeste B-mesonen en -baryonen deze richting op vliegen wanneer ze geproduceerd worden bij een proton-proton botsing.

Door de jaren heen, de LHC begon met proton-proton botsingen in 2010, zijn er verschillende periodes zonder botsingen geweest om verbeteringen aan te brengen aan zowel de LHC als de experimenten. Er zijn tot nu toe 2 lange periodes geweest wanneer er data verzameld werd door de experimenten, Run 1 van 2010-2013 en Run 2 van 2015-2018. In 2022 is de LHC weer begonnen met het opstarten van de proton-proton botsingen voor de volgende periode van data verzamelen, Run 3. Tussen Run 2 en Run 3 zijn er wederom grote verbeteringen gedaan aan de LHC en de experimenten.

Is er nog meer dan Standaard Model?

Ondanks dat het Standaard Model een erg succesvolle theorie is, veel processen in de deeltjesfysica kunnen er nauwkeurig mee beschreven worden, is er altijd de vraag: is er nog meer natuurkunde voorbij het SM? Er zijn namelijk een aantal vragen waarop het SM geen antwoord heeft. Waarom zijn er precies 6 soorten quarks en 6 soorten leptonen? Uit experimenten is gebleken dat op zijn minst twee van de drie type neutrino's een massa hebben, terwijl ze in het SM massaloos zijn. Naast deze bestaande vragen zijn er de laatste jaren een aantal metingen gedaan waarbij de uitkomst anders is dan de waarde die verwacht werd op basis van het Standaard Model. Het komt wel vaker voor dat een meting niet voldoet aan de verwachtingen uit het SM. Er worden zoveel metingen uitgevoerd dat je puur op basis van statistiek kan verwachten dat er soms een meting afwijkt. Wat deze specifieke afwijkingen interessant maakt is dat ze allemaal in dezelfde hoek van de deeltjesfysica zitten, namelijk in het gedrag van muonen en het verval van B-mesonen. Deze set van afwijkingen wordt binnen de deeltjesfysica de *Flavour anomalies* genoemd. Ondanks dat er geen meting bij zit die zo veel afwijkt van het SM dat het binnen de deeltjesfysica een ontdekking genoemd wordt[2], hebben deze afwijkingen er wel voor gezorgd dat er meer onderzoek gedaan wordt naar theoriën voorbij het SM die deze afwijkingen zouden kunnen verklaren.

Een van de manieren om het SM uit te breiden is door een nieuw krachtdragend deeltje toe te voegen die op zijn beurt nieuwe interacties zou toelaten. In deze scriptie is er onderzoek gedaan naar zo'n nieuw krachtdragend deeltje: de leptoquark. Zoals de naam al een beetje weggeeft koppelt de leptoquark een lepton direct aan een quark. Dit is een soort interactie die niet toegestaan is in het SM. Wanneer een leptoquark wordt toegevoegd aan het SM

---

[2]Binnen de deeltjesfysica is er de eis dat, om iets een ontdekking te kunnen noemen, er een afwijking moet zijn van vijf standaarddeviaties. Wat dit inhoudt is dat de kans dat het afwijkende resultaat komt door een statistische fluctuatie in de data kleiner moet zijn dan 1 op 3.5 miljoen.

zorgt dit voor een groot aantal nieuwe processen die ineens wel mogelijk zijn. Verder draagt de leptoquark ook bij aan processen die wel al mogelijk zijn in het SM, maar die met een leptoquark ineens vaker zouden kunnen gebeuren. Het is belangrijk om te controleren dat, wanneer we een leptoquark toevoegen, deze niet de voorspellingen die wel overeenkomen met gemeten waardes verandert. In deze scriptie worden leptoquarks bestudeerd vanuit twee kanten: theoretische deeltjesfysica en experimentele deeltjesfysica, waarbij een deel van de focus zal liggen op een process wat alleen kan plaats vinden wanneer er leptoquarks zijn. Dit proces is het verval van een B-meson naar een tau en een muon: $B_{(s)} \rightarrow \tau\mu$.

Het onderzoek in deze scriptie

Vanuit een theoretisch oogpunt hebben we gekeken naar hoe we een theorie kunnen opbouwen waarin een leptoquark toegevoegd is aan het standaardmodel. Hier is ook gekeken naar de voorspellingen van zo'n model voor het $B_{(s)} \rightarrow \tau\mu$ verval. Verder hebben we gekeken hoe een ander model met een leptoquark, er zijn veel verschillende soorten leptoquark die zich allemaal net anders gedragen, de flavour anomalies kan verklaren en tegelijk consistent kan zijn met metingen die wel kloppen met het SM. Hierbij hebben we gekeken naar hoe sterk de koppeling van de leptoquark aan de SM deeltjes moet zijn. Ook hebben we bestudeerd of het nieuwe model de data beter beschrijft dan het SM.

Aan de experimentele kant hebben we gewerkt aan de meting van het $B_{(s)} \rightarrow \tau\mu$ verval met het LHCb experiment. Eerst hebben we ervoor gezorgd dat gedurende de volgende data-verzamelings periode, Run 3, er meer potentieel interessante data opgeslagen wordt voor dit proces. Dit hebben we gedaan door mee te schrijven aan de software die bepaalt welke data wel en niet opgeslagen wordt. Hierna hebben we een begin gemaakt aan de zoektocht naar het $B_{(s)} \rightarrow \tau\mu$ verval in de data verzameld gedurende Run 2.

Leptoquarks in de theoretische deeltjesfysica

De natuur gedraagt zich anders bij hoge energiën dan bij lage energiën. Bij een lage temperatuur (dus weinig energie) verandert water van een vloeistof naar een vaste stof, namelijk ijs. Bij een hoge temperatuur (dus veel energie) verandert water juist in een gas. Het SM uit zich ook op andere manieren wanneer we het bestuderen bij hogere energiën. Het werd pas duidelijk bij experimenten waar atomen bij een hoge energie bestudeerd werden dat ze uit protonen en neutronen bestonden. Toen ze bij nog hogere energiën onderzocht werden bleek dat de protonen en neutronen zelf uit quarks bestonden. Het gedrag van quarks, en alle andere deeltjes uit het SM verandert wanneer we de energie maar ver genoeg ophogen. Ook de wiskundige beschrijving van het gedrag verandert mee. Hoe we een theorie of model op de allerhoogste energiën kunnen beschrijven wordt vaak de UV-beschrijving of UV-theorie genoemd. In deze scriptie hebben we gekeken naar de UV-theorie die leidt tot een specifiek type leptoquark in het SM. Het model in kwestie is het zogenaamde 4321-model[15].

We zijn gestart vanaf een gezamenlijke beschrijving van het SM en de leptoquark op de hoogste energie. Het doel was om een dusdanige model te bouwen dat, wanneer we de energie verlagen, we eindigen met het SM zoals we dat kennen met de toevoeging van een leptoquark.
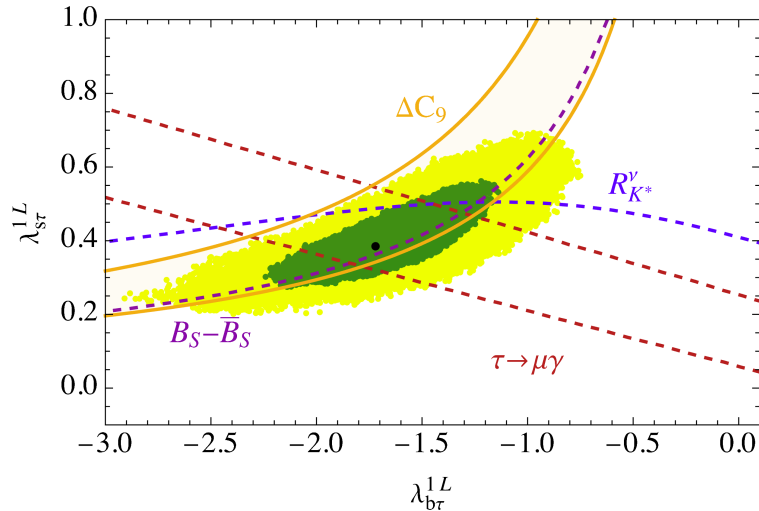
Figure 8.5: De toegestane waardes voor de koppeling van de leptoquark aan een b-quark en τ-lepton op de horizontale as en de koppeling van de leptoquark aan een s-quark en τ-lepton op de verticale. De beste waarde voor de koppelingen is de zwarte punt. De groene punten en gele punten zijn de toegestane afwijkingen binnen een bepaalde foutmarge (1 of 2 standaard deviaties). Met de gekleurde lijnen zijn verschillende limieten op deze koppelingen op basis van specifieke processen weergegeven.

We beschrijven deze transitie van hoge naar lage energie en we onderzoeken hoe deze plaats moet vinden om het gewenste effect te hebben. We hebben gevonden dat, om het juiste type leptoquark te krijgen in het SM, er ook andere nieuwe deeltjes aan het SM toegevoegd moeten worden. Vervolgens is er gekeken naar de manier waarop de leptoquark en de andere nieuwe deeltjes interacties aan gaan met de SM-deeltjes. De precieze interactie-structuur van de leptoquark die nodig is om een oplossing voor de "flavour anomalies" te zijn is ook bestudeert. Op het einde is er ook berekend in welke mate deze leptoquark bijdraagt aan het $B_{(s)} \to \tau\mu$ proces.

In de tweede helft van het theoretische onderzoek naar leptoquarks hebben we onderzoek gedaan naar een andere uitbreiding van het SM. We hebben gekeken naar wat we aan nieuwe type deeltjes zouden moeten toevoegen aan het SM om de flavour anomalies te kunnen verklaren. We hebben hier gekeken naar een minimale oplossing: wat is het minimale aan nieuwe deeltjes wat we moeten toevoegen om de flavour anomalies te kunnen verklaren? We hebben een bepaald type leptoquark toegevoegd samen met een geladen higgs-achtig deeltje. Vervolgens hebben we de bijdrages van deze nieuwe deeltjes aan verscheidene processen berekend. Onder deze processen vallen de flavour anomalies, maar ook processen waarvan de SM voorspelling overeenkomt met de gemeten waardes. A priori is het niet bekend hoe sterk te koppeling van de nieuwe deeltjes aan de SM deeltjes is. Er is gekeken naar hoe sterk, of zwak, deze koppelingen zouden moeten zijn om de data zo goed mogelijk te beschrijven. Uit deze analyse hebben is een set met beste waardes voor deze koppelingen gekomen. Het ene proces zet strengere limieten voor bepaalde koppelingen dan andere processen. Er is daarom ook gekeken naar hoe de individuele processen de waardes voor de koppelingen beperken.

Tegelijkertijd is er gekeken naar hoeveel er afgeweken kan worden van de beste waarde zonder dat de kwaliteit van de beschrijving te veel afneemt. Een voorbeeld hiervan is te zien in Figuur 8.5. In dit figuur kan je duidelijk zien dat de toegestane waardes van de koppelingen binnen de foutmarges een combinatie is van de individuele limieten gesteld door de processen. We hebben ook aangetoond dat dit model de data beter beschrijft dan alleen het SM. Een van de "nadelen" van dit model is dat het geen meetbare bijdrage levert aan het $B_{(s)} \rightarrow \tau\mu$ proces, waar het model wat we hiervoor bestudeerd hebben dit wel deed.

Experimentele zoektocht naar $B_{(s)} \rightarrow \tau\mu$

Wanneer de LHC protonen laat botsen, gebeurt dit niet met 1 of 2 botsingen per seconde, maar met miljoenen botsingen per seconde. In heel weinig van deze botsingen vinden de processen plaats waar we in geïntereseerd zijn. In een ideale wereld zouden we alle informatie van alle botsingen opslaan en dan later eruit halen wat interessant is. Dit gaat helaas niet. De hoeveelheid data zou zo groot zijn dat het niet door kabels weg te schrijven is naar harde schijven. Er moet vlak na een botsing al bepaald worden of deze misschien een interessant proces bevat en of hij dus wel of niet opgeslagen moet worden. Om deze keuzes te kunnen maken is er software geschreven die vlak na een botsing kan bepalen of de data wel of niet interessant is. In deze scriptie is er een stuk software (dit noemen we *code*) geschreven wat controleert of er in een botsing een mogelijk $B_{(s)} \rightarrow \tau\mu$ signaal zit. Dit wordt gedaan op basis van code, die controleert of er een τ en een muon geproduceerd en waargenomen zijn in de botsing en of deze ongeveer van dezelfde plek komen. De muonen kunnen direct waargenomen worden door het LHCb experiment. De tau deeltjes leven niet lang genoeg om ze direct waar te nemen. Ze vervallen naar drie π-mesonen en een neutrino: $\tau \rightarrow \pi\pi\pi\nu_\tau$. Als dit signaal aanwezig is in de detector wordt de data opgeslagen. Naast de software voor dit proces is er ook software geschreven voor honderden andere processen. Voor al deze processen kan tegelijkertijd gecontroleerd worden of de data opgeslagen moet worden. Onze software zal gebruikt worden bij het verzamelen van data in Run 3.

Er is ook een begin gemaakt met de zoektocht naar het $B_{(s)} \rightarrow \tau\mu$ verval in de data van Run 2, waarbij we ook specifiek kijken naar processen waar de tau vervalt als $\tau \rightarrow \pi\pi\pi\nu_\tau$. Omdat dit proces in het SM niet voorkomt en zelfs met de toevoeging van een leptoquark nog heel zeldzaam is, is het belangrijk dat we heel goed begrijpen welke processen er mogelijk als achtergrond aanwezig zijn. Ookwel, van welke processen denken we dat het een $B_{(s)} \rightarrow \tau\mu$ is, maar is het eigenlijk iets anders. Een van de mogelijke achtergrond processen die we onderzocht hebben is het verval van Λ_b baryonen. Om dit te onderzoeken hebben we deze vervallen gesimuleerd met een programma genaamd RapidSim. Vervolgens hebben we gedaan alsof deze data $B_{(s)} \rightarrow \tau\mu$ data is en op basis daarvan eisen gesteld waaraan het proces moet voldoen. Nadat we deze eisen gesteld hadden bleef er nauwelijks nog data over, waarop we konden concluderen dat deze Λ_b baryonen geen potentieel achtergrondsignaal is.
Wat het meten van dit proces extra moeilijk maakt is het feit dat we een τ-lepton in het verval hebben. De reden dat dit ingewikkeld is, is dat de τ niet lang leeft en altijd een neutrino als vervalproduct heeft en dat we neutrino's niet kunnen meten in onze detector. Hierdoor mist er altijd een klein stukje informatie. Gelukkig kunnen we de drie π-mesonen

wel meten in de detector en daarmee het punt waar in de detector de τ vervalt vinden. Verder weten we ook waar in de detector de botsing heeft plaatsgenomen. Doordat we deze twee stukjes informatie tot onze beschikking hebben kan de missende informatie van de neutrino gereconstrueerd worden. Doordat in eerste instantie de informatie, en dus de energie, van het neutrino mist is ook de massa van het B-meson wat gemeten is lager dan dat het daadwerkelijk is. Door het gereconstrueerde neutrino energie te gebruiken kan de werkelijke B-massa bepaald worden. Dit is getest op gesimuleerde $B_{(s)} \to \tau\mu$ data en er is aangetoond dat de methode die we gebruiken effectief is.